Transmission-Type Impedance Probes for Use in Complex Plasmas

by

Brandon Doyle

A dissertation submitted to the Graduate Faculty of
Auburn University
in partial fulfillment of the
requirements for the Degree of
Doctor of Philosophy

Auburn, Alabama
December 9, 2023

Keywords: Plasma, Diagnostics, Complex Plasma

Approved by

Uwe Konopka, Professor (Department of Physics, Auburn University)
Edward Thomas Jr., Dean of the College of Sciences and Mathematics
and Professor of Physics, (Auburn University)
Guillaume Marc Laurent, Professor (Department of Physics, Auburn University)
David Maurer, Professor (Department of Physics, Auburn University)
Chad Rose, Assistant Professor (Department of Mechanical Engineering, Auburn University)

Abstract

Impedance probes measure electron density (n_e) and electron temperature (T_e) by interpreting frequency-dependent transmission or reflection spectra (S_{21} or S_{11}) of radiofrequency (RF) signals of low power (10^{-5} W). This diagnostic method is promising for use in complex plasmas because it is less disruptive to plasma and dust than Langmuir probes, and it is easier and cheaper to implement than many common spectroscopic measurements, such as laser-induced fluorescence (LIF). Transmission-type impedance probes offer some further advantages over reflection-type probes because they can resolve plasma conditions near the probe vs farther away in the chamber, and because they also may be used as a DC double Langmuir probe. One potential application is to measure the charge of a dust cloud by performing RF and DC measurements to measure n_e and n_i, and then to determine the charge on the dust via the quasineutrality condition, $n_i - n_e - z_d n_d \approx 0$.

This work explores the topic of transmission-type impedance probes in three ways. Firstly, a theoretical model is developed to understand transmission-type impedance probe spectra. Secondly, experiments are performed in which transmission spectra are recorded using these probes in RF glow discharge plasmas. And lastly, a computer model is developed to simulate the probe-plasma system, treating the continuous plasma medium as a series of discrete circuit elements and using SPICE algorithms to simulate the transmission of RF signals through the plasma. This computer model is then used to determine n_e and T_e from experimental transmission spectra. We end by discussing ways of implementing this diagnostic technique in dusty plasma experiments, both for ground-based experiments and for microgravity experiments.

Dedication

To Sir Ghillean Prance, whom I have never met, but who once inspired a young boy on the Amazon River to become a scientist.

And to my dad, whom I love, and who once inspired a young boy on the San Marcos River to become a scientist.

And to my girls, whom I love more than I know how to say, and who do not have to like rivers ***or*** *science.*

Acknowledgments

A dissertation is never a solitary endeavor, and mine is no exception – the people who helped me through this process are myriad. I want to say a heartfelt thanks to my advisor, Uwe Konopka, and to the other members of my committee, whose guidance helped me steer this ship of a dissertation, and whose patience helped me right it whenever I capsized.

Thanks to the other members of my group. Thanks to the professors and to the research faculty and staff. Thanks to the other graduate students, those who came before me and those who come after. And thanks even to those grad students who came after me and left before me. Among the (former) students before me, thanks in particular to Ami DuBois for her patient mentoring.

And finally, I must thank my "other committee." Out of all the people whose support I so heavily relied upon, thanks most of all to my wife, Sarah, without whom I would never have survived graduate school. Thanks also to my dear friend, Ellie Williamson, without whom I would never have *left* graduate school. And of course, thanks to my parents and my brother, who cheered me on every step of the way.

Table of Contents

Abstract ii

Dedication iii

Acknowledgments iv

1 Dusty Plasmas 1

1.1 General Plasma Concepts 2

1.1.1 What is a Plasma? 3

1.1.2 Low Temperature Plasmas 3

1.1.3 Quasineutrality 5

1.1.4 The Plasma Frequency 5

1.1.5 The Debye Length 8

1.1.6 Sheathes 9

1.2 Dusty Plasmas 11

1.2.1 Forces on Dust Particles 12

1.2.2 Dust Charge 13

1.2.3 Dust Crystals 16

1.2.4 Microgravity 17

1.3 LTP Diagnostic Methods 17

1.3.1 Langmuir Probes 17

1.4 Impedance Probes 18

1.4.1 Early Work . . . 19
1.4.2 Models . . . 20
1.4.3 Probe Design . . . 20

2 Theory . . . 24
2.1 Impedance Probes . . . 24
2.2 Circuit Model . . . 25
2.3 Fluid Model for Bulk Plasma . . . 27
2.3.1 Plane Wave Solutions . . . 28
2.3.2 Ohm's Law . . . 29
2.3.3 Circuit Model Elements from Fluid Model . . . 32

3 Experiment . . . 34
3.1 Plasma Devices . . . 34
3.1.1 DODECA . . . 34
3.1.2 RaFyL . . . 35
3.2 Impedance Probe . . . 36
3.3 Experimental Setup . . . 36
3.4 Results and First Analysis . . . 38
3.4.1 Qualitative Fitting . . . 40
3.4.2 Fit Uncertainties . . . 41

4 Circuit Simulations . . . 48
4.1 The Simulation Object . . . 49
4.1.1 Calculating Sheath Thickness . . . 50
4.1.2 Calculating Capacitances . . . 53

4.1.3 Calculating Bulk Plasma Values . . . 56
4.1.4 Basic Circuit Simulation Results . . . 56
4.1.5 Qualitative Comparison to Experiment . . . 57
4.2 High Frequency Limit . . . 59
4.2.1 Reproducing the Mismatch in a Simplified Circuit . . . 60
4.2.2 Fixing the High Frequency Limit . . . 62
4.3 Density Near and Far . . . 65
4.4 Fitting Data With vna.py . . . 68

5 Conclusion and Outlook . . . 73
5.1 Comparison of Analyses . . . 73
5.2 Future Experimental Work . . . 75
5.2.1 RaFyL Development . . . 75
5.2.2 Future Experiments . . . 77
5.2.3 COMPACT . . . 79
5.3 Future Modeling Work . . . 81
5.3.1 vna.py Improvements . . . 81
5.3.2 Plasma Model Improvements . . . 81

References . . . 83

Appendices . . . 90

A Sheath Width Calculation . . . 91
A.1 Setup . . . 91
A.2 Solving for Probe Sheath Width . . . 92
A.3 Chamber wall: . . . 100

A.3.1 Another way to solve the wall sheath: 105

A.4 Conclusion 111

List of Figures

1.1 LTPs compared to other plasmas 4
1.2 Numerically-Calculated Plasma Sheath Example 10
1.3 RF Reflection Probes 21
1.4 RF Transmission Probes 23
2.1 S-Parameters 24
2.2 Reflection-Type and Transmission-Type Impedance Probes 25
2.3 Plasma Circuit Models 26
3.1 DODECA 35
3.2 RaFyL 36
3.3 Circuit diagram for simultaneous RF and DC measurements. 37
3.4 Impedance Probes 37
3.5 Experimental Spectra 39
3.6 Fitting data with two Gaussian curves 40
3.7 Double Gaussian fit Result 41
3.8 Gaussian fit widths and center frequencies 42
3.9 Error calculation requires full 6-D χ^2 analysis 43
3.10 3D χ^2 error ellipsoids 45
3.11 2D χ^2 map: refitting vs full 6-D analysis 46
4.1 vna.py Plasma Circuit Modeling Flowchart 49
4.2 Determining Sheath Thickness 51

4.3 Solving Poisson's Equation in the Plasma Chamber 55
4.4 Simulated Transmission of RF Signal 58
4.5 Simulation vs. Experiment 59
4.6 High Frequency Problem – Double Probe 60
4.7 High Frequency Problem – Single Probe 61
4.8 High Frequency Circuit Models 62
4.9 The Δ-Y Transform 63
4.10 Using $\Delta - Y$ Transform to Find Plasma Capacitance 64
4.11 High Frequency Correction Results 65
4.12 Effect of n_e near probes 66
4.13 Effect of n_e far from probes 67
4.14 Experimental data were fit using vna.py objects and methods. 70
4.15 Plasma Parameters Found with vna.py 71
4.16 Spectra with ω_{pe} fits 72
5.1 Comparison of Analyses: Qualitative Reproduction of Data 74
5.2 Comparison of Analyses: Quantitative Interpretation of Fits 76
5.3 Improved measurement circuit block diagram. 77
5.4 Image: impedance probes creating a dust void 78
5.5 Proposed electrode-to-electrode APRS measurements 79
5.6 COMPACT 80

List of Tables

3.1 Experiment Parameters 38

3.2 Data fitting with two gaussian curves, one positive and one negative. DODECA plasma chamber, probe separation $\sim$ 2 mm, neutral pressure 6 Pa (45 mTorr), electrode V_{RMS} 41

Chapter 1

Dusty Plasmas

A dusty plasma, also called a complex plasma, is a low temperature plasma containing a significant amount of dust. A low temperature plasma (LTP) is a partially-ionized gas, containing three particle species: ions, electrons, and neutrals, by which we mean non-ionized gas atoms or molecules. A dusty plasma, then, is a four-component plasma; it consists of ions, electrons, neutrals, and dust.

Dusty plasmas are ubiquitous in astrophysical and space physics, appearing in protoplanetary nebulae, comet tails, and planetary rings, to name a few [42, 37]. Closer to Earth, meteorites and man-made objects alike ignite plasmas around themselves as they enter Earth's atmosphere at hypersonic speeds ($u \gtrapprox 5u_{sound}$). Fine particles may flake off of rocky surfaces or ceramic heat shields, which can effect these encasing plasmas. One presumes that this effect is also important for hypersonic vehicles and weapons within the atmosphere, though if such research were indeed ongoing, I would not know about it. Here on Earth's surface, dusty plasmas appear in lightning strikes and campfires, and, much to the chagrin of scientists and shareholders alike, dusty plasmas appear within the plasma processing chambers used in the manufacture of silicon wafer electronics [45].

The dust component of a complex plasma significantly effects the plasma phenomena common to all LTPs, as well as creating entirely new phenomena that only exist in dusty plasmas. The presence of dust also complicates the use of some common LTP

diagnostic methods, especially Langmuir probes, which perturb the dust and whose measurements are in turn effected *by* the dust [28, 27]. Plasma impedance probes (PIPs) are a promising diagnostic technique for use in dusty plasmas because these probes, and the experiments they're used in, may be designed in such a way as to be less perturbing to plasma and dust than Langmuir probes.

PIPs represent one method among a class of diagnostic methods called Active Plasma Resonance Spectroscopy (APRS). Low-power signals in the radio-frequency (RF) range are applied to a plasma, and the plasma's response to this signal is measured. In the case of PIPs, this response is measured as the signal reflected off of or transmitted through the plasma. Many PIP designs are possible for various applications. In this work, we will focus on the PIP measurements of RF signals transmitted between two cylindrical probe tips submerged in plasma.

Before further discussing the use of impedance probes in a dusty plasma, it is useful to define some of the terms and concepts used in this thesis, especially because some of these terms can have slightly different meanings in different contexts. To that end, we will start with a discussion of dusty plasmas. We shall first discuss plasmas and especially LTPs, and then we will discuss the impact of adding dust. We shall then turn our attention to plasma impedance probes and their application to plasma with and without dust.

1.1 General Plasma Concepts

This section may be considered a primer of plasma concepts, but herein I shall only discuss those concepts relevant to this work. A more complete introduction to plasma physics may be found in, for example, "Introduction to Plasma Physics and Controlled Fusion," by Francis Chen [12] or "Fundamentals of Plasma Physics," by Paul Bellan [5]. For dusty plasmas in particular, there is an excellent 2002 review article by Alexander Piel and Andre Melzer [42], and a more conversational 2004 Physics Today article by Bob Merlino and John Goree [37].

1.1.1 What is a Plasma?

A plasma is a type of fully- or partially-ionized gas. Electrons around the gas molecules are energized to the extent that some significant proportion of these electrons escape their potential wells to move freely from the gas molecule. There are competing definitions of what separates a plasma from a mundane ionized gas.

We will take the very broad definition that a plasma is any gas with significant enough ionization fraction that plasma concepts are useful in describing the physics involved. A neon light is a plasma. Fire is a plasma. A "plasma ball" toy contains plasma.

By some definitions of plasma, including that presented in Chen's excellent textbook recommended above [12], these examples are not plasmas, they are merely ionized gases. Indeed, it can be argued that there will be no plasmas discussed in this dissertation at all because, for the RF discharges in question, gas drag dominates over long-range Coulomb forces. But it is useful to refer to these RF discharges as plasmas, and so we shall do so with the acknowledgment that these plasmas do not meet the definitions used in some other contexts.

1.1.2 Low Temperature Plasmas

Gas discharges are relatively diffuse, cold plasmas with small ionization fractions ($\sim 10^{-6}$) and plasma densities ($n \sim 10^{-14}$ to $10^{-16} m^{-3}$). The ions are typically assumed to be exclusively singly-ionized. The ions' temperatures are often near room temperature ($T_i \approx \frac{1}{40} eV$), whereas the electrons tend to be warmer ($T_e \sim 10^0 eV$). Gas discharges are denser, warmer plasmas than many space plasmas, but we nevertheless categorize them as Low Temperature Plasmas (LTPs). This categorization serves to differentiate LTPs from other *laboratory* plasmas, such as fusion plasmas, which must operate at temperatures hotter than the sun. LTP electron parameters are shown vis-a-vis other types of plasmas in Figure 1.1.

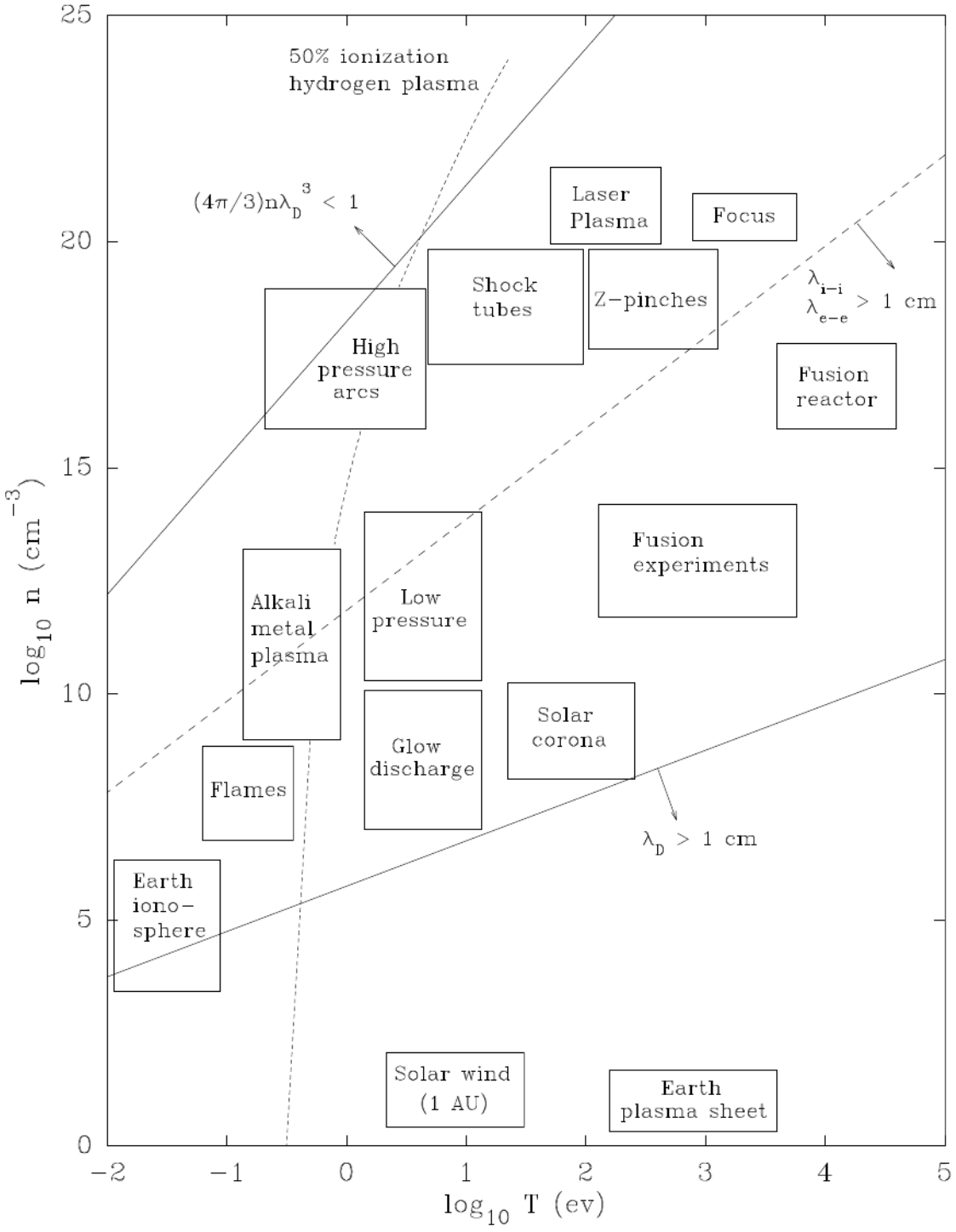

Figure 1.1: Plasmas are categorized according to their plasma parameters, such as temperature and density. This diagram, reproduced from the NRL Plasma Formulary [10], shows various types of plasmas categorized by their electron plasma parameters. The work in this thesis pertain to RF and DC glow discharges.

1.1.3 Quasineutrality

One of the most fundamental aspects of plasma physics is the phenomenon of quasineutrality. That is, on a macroscopic scale, a given region of plasma tends to maintain the condition of containing equal numbers of positive and negative charges. Assuming singly-ionized ions, we may write this in terms of the electron and ion densities, n_e and n_i, respectively:

$$n_i - n_e \approx 0. \tag{1.1}$$

However, at fast temporal scales and short spatial scales, these densities are constantly undergoing small fluctuations. By "fast," we mean that the fluctuations happen with frequencies on the order of the plasma frequency, ω_p. By "short," we mean that they happen on spatial scales shorter than a few Debye lengths, λ_D.

The quantities ω_p and λ_D are ubiquitous in plasma physics, critical to many plasma phenomena. There are, therefore, a number of equally-valid ways to introduce these concepts. With an eye towards the work in this thesis, let us introduce them as the temporal and spatial limits of quasineutrality: plasmas are quasineutral on timescales slower than ω_p and on spatial scales bigger than λ_D. With this context in mind, we shall now discuss both the plasma frequency and the Debye length in more detail.

1.1.4 The Plasma Frequency

When fluctuations in plasma density occur, the nearby plasma particles rearrange themselves so as to remove these nonuniformities in density and restore quasineutrality. For each charged plasma species, α, there is a characteristic frequency, $\omega_{p\alpha}$, called the plasma frequency, which is associated with this restoring motion [11]. This restoring motion leads to self-excited oscillations which arise purely from the electrostatic equations of motion of charged particles in a plasma. We shall now demonstrate this for electrons.

Within a bulk plasma of uniform 0^{th} order plasma density, n_0, consider a small volume of plasma where random motion produces small fluctuations in the local electron density,

$$n_e = n_0 + \widetilde{n} \tag{1.2}$$

where these 1^{st} order fluctuations take the form,

$$\widetilde{n} = n_1 e^{i\omega t}, \tag{1.3}$$

where n_1 is the (small) amplitude of density fluctuation, ω is the frequency of this fluctuation, and $i = \sqrt{-1}$ is the imaginary unit number. We could have equivalently defined the fluctuations in terms of trigonometric functions, but this exponential form allows for the convenient analysis of derivatives:

$$\frac{\partial n_e}{\partial t} = \frac{\partial}{\partial t}\widetilde{n} = i\omega\widetilde{n}. \tag{1.4}$$

The electron motion associated with the fluctuating density will be governed by the electron continuity condition, which we express in terms of the divergence of electron fluid velocity, $\mathbf{u}$:

$$\nabla \cdot \mathbf{u} = \frac{-1}{n_e}\frac{\partial n_e}{\partial t}. \tag{1.5}$$

The electrons will of course be subject to Gauss's Law, which we express in a similar manner,

$$\nabla \cdot \mathbf{E} = \frac{-en_e}{\epsilon_0}. \tag{1.6}$$

We may describe the electron motion with the usual Momentum (conservation) Equation, which is a form of Newton's 2^{nd} Law:

$$\frac{D\mathbf{u}}{Dt} = \left(\frac{\partial}{\partial t} + (\mathbf{u} \cdot \nabla)\right)\mathbf{u} = \Sigma\mathbf{F}, \tag{1.7}$$

where $\mathbf{F}$ are the various forces acting on the electrons and D/Dt is the so-called convective derivative, which is the time derivative in the reference frame that follows the electron flow velocity, $\mathbf{u}$.

For now, we shall assume that there is no 0^{th} order electron flow ($\mathbf{u}_0 = 0$), and thus the convective derivative is equal to the partial derivative ($D/Dt = \partial/\partial t$), at least for 0^{th} and 1^{st} order terms.

As an aside, even though we have only introduced fluctuations of the 1^{st} order of smallness, and even though we have assumed that $\mathbf{u}_0 = 0$, D/Dt *does* nevertheless differ from $\partial/\partial t$ in its 2^{nd} order terms, by which we mean terms containing the multiplication of two quantities that are of the 1^{st} order of smallness.

Regardless, we shall proceed by similarly assuming that $\mathbf{E} = 0 + \widetilde{\mathbf{E}}$ and writing the acceleration of electrons due to the electric field as,

$$\frac{\partial \mathbf{u}}{\partial t} = \frac{-e}{m_e}\widetilde{\mathbf{E}}, \tag{1.8}$$

With Equations 1.5 and 1.6 in mind, we consider the divergence of this motion:

$$\frac{\partial}{\partial t}\left(\nabla \cdot \mathbf{u}\right) = \frac{-e}{m_e}\left(\nabla \cdot \widetilde{\mathbf{E}}\right). \tag{1.9}$$

and we use these equations to rewrite Equation 1.9 as,

$$\frac{1}{n_e^2}\left(\frac{\partial}{\partial t} n_e\right)^2 - \frac{1}{n_e}\frac{\partial^2}{\partial t^2} n_e = \frac{e^2 \widetilde{n}}{m_e \epsilon_0}. \tag{1.10}$$

These time derivatives may readily be evaluated using Equation 1.4 and the identity, $i^2 = -1$, resulting in,

$$\omega^2\left(\frac{\widetilde{n}}{n_e} - \frac{\widetilde{n}^2}{n_e^2}\right) = \frac{e^2 \widetilde{n}}{m_e \epsilon_0}. \tag{1.11}$$

We now expand n_e into $n_0 + \widetilde{n}$ and solve for the value of ω which satisfies Equation 1.11. After some algebra, we my write this frequency, which we name the plasma

frequency, in the following form:

$$\omega_{pe}^2 \approx \frac{e^2 n_0}{m_e \epsilon_0}. \tag{1.12}$$

This approximate solution to Equation 1.11 is valid to the 0^{th} and 1^{st} order of fluctuations, which is also the limit of the derivation *leading* to Equation 1.11 anyway. For greater precision, we would need to have written Equation 1.8 using the proper convective derivative.

The derivation above considers only the self-excited motion of electrons. In Chapter 2, we shall expand on this to describe the motion of electrons driven in the near field of a radio-frequency (RF) voltage source. In that discussion, we will see that ω_{pe} is critically important to the analysis of impedance probe spectra.

1.1.5 The Debye Length

In Section 1.1.3, we said that quasineutrality holds true for timescales slower than the plasma frequency and length scales larger than the Debye length. Having introduced ω_p in the previous section, we now turn our attention to the Debye length, λ_D.

Consider a "small" test charge of charge q immersed in a plasma. The charge produces the usual Coulomb potential in the surrounding area, $\phi(r) = q/4\pi\epsilon_0$, but this Coulomb potential rearranges the electrons and ions in the vicinity, which in turn changes the effective potential "seen" by charges near this test charge. As it turns out [12, 31], the resulting effective potential structure is the usual Coulomb potential modified by an exponential screening term:

$$\phi(r) = \frac{q}{4\pi\epsilon_0} e^{-r/\lambda_D}. \tag{1.13}$$

This screened Coulomb potential is sometimes called the Debye-Huckel potential, and λ_D is the Debye length:

$$\lambda_D = \sqrt{\frac{\epsilon_0 k_B T_e}{n_e e^2}}. \tag{1.14}$$

This screening drastically diminishes the importance of electrostatic effects in plasma from sources farther away than a few Debye lengths. Looking ahead to the case of plasma crystals, which we shall discuss in Section 1.2.3, this screening is the reason that the spacing between dust particles in liquid or crystalline phase tends to be about a Debye length [31].

1.1.6 Sheathes

Large objects immersed in plasma cause much greater perturbations than those described in the previous section. We refer to the plasma volume near a macroscopic charged object in plasma as the "plasma sheath" [2].

Because the electrons have much higher mobility than the ions in plasma, an object in plasma will experience a much higher rate of collisions with electrons, and this object will typically acquire a highly negative charge. This negative charge pushes away electrons and attracts ions, and the plasma sheath has a suppressed electron density as a result, as shown in Figure 1.2.

Finding the electric potential, ϕ, and the electron and ion densities, n_e and n_i, in the sheath is typically accomplished by numerically solving Poisson's equation in the region,

$$\nabla^2 \phi(\mathbf{r}) = \frac{e\left(n_e(\mathbf{r}) - n_i(\mathbf{r})\right)}{\epsilon_0}. \tag{1.15}$$

for ion and electron densities, n_i and n_e, at any point, $\mathbf{r}$, in the plasma sheath. We have here made the assumption that all ions are singly-ionized. We can solve Equation 1.15 by making some further assumptions about the behavior of ions and electrons in the sheath.

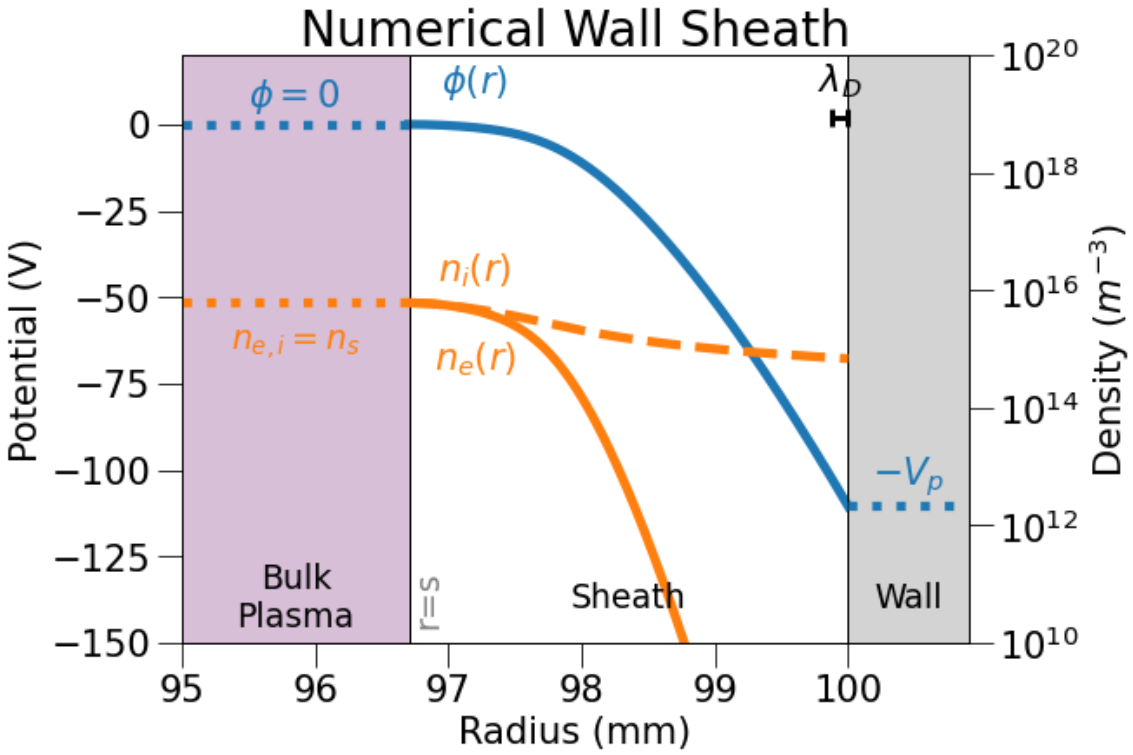

Figure 1.2: A numerical solution of electric potential and particle number densities in a sheath between a (bulk) plasma and the spherical chamber wall. The wall is here assumed to be grounded, but that need not be the case. The sheath edge is at radius, s, and the electron and ion plasma densities at the sheath edge are both n_s. Quasineutrality does *not* hold in a plasma sheath; electron density is highly suppressed in this region. By convention, we define the bulk plasma to have electric potential $\phi = 0$. This means that the (grounded) chamber wall is at $\phi = -V_{plasma}$. This choice is arbitrary, as only $\nabla\phi$ has physical meaning, not the value of ϕ.

We may immediately write an expression for n_e by assuming that electron energy is Boltzmann distributed:

$$n_e(\mathbf{r}) = n_0 \, exp\left(\frac{e\phi(\mathbf{r})}{k_B T_e}\right). \tag{1.16}$$

To find n_i, we first invoke the Bohm sheath criterion, which states that ions must enter the sheath with the ion sound speed:

$$|\mathbf{u}_i(sheath\,edge)| = u_B = \left(\frac{k_B T_e}{m_i}\right)^{1/2}. \tag{1.17}$$

We note that ions do not accumulate in the sheath, and we use this Bohm criterion to express ion continuity:

$$n_0 u_B = n_i(\mathbf{r}) u_i(\mathbf{r}). \tag{1.18}$$

Meanwhile, taking the bulk plasma to have potential $\phi = 0$, and neglecting ion collisions, we write ion conservation of energy as,

$$\frac{1}{2} m_i u_B^2 = \frac{1}{2} m_i u_i^2(\mathbf{r}) + e\phi(\mathbf{r}). \tag{1.19}$$

We use Equations 1.18 and 1.19 to construct an expression for the ion density in the sheath as a function of only $\phi(\mathbf{r})$ and not $u_i(\mathbf{r})$:

$$n_i(\mathbf{r}) = n_0 \left(1 - \frac{e}{\frac{1}{2} m_i u_B^2} \phi(\mathbf{r})\right)^{-1/2} \tag{1.20}$$

And so we rewrite Equation 1.15 using Equations 1.16 and 1.20,

$$\nabla^2 \phi(\mathbf{r}) = \frac{n_0 e}{\epsilon_0} \left(exp\left(\frac{e\phi(\mathbf{r})}{k_B T_e}\right) - \left(1 - \frac{e}{\frac{1}{2} m_i u_B^2} \phi(\mathbf{r})\right)^{-1/2} \right). \tag{1.21}$$

Given appropriate boundary conditions for the sheath in question, Equation 1.21 may be solved numerically. For example, Figure 1.2 shows the resulting electric potential and plasma densities for a grounded spherical chamber wall. The object need not be grounded; the same process can be used to solve sheathes around electrically floating objects, as well as objects with DC voltages imposed upon them by an outside voltage source.

1.2 Dusty Plasmas

Dusty plasma effects have long been known to be important in various astrophysical and space physics system. The field of *laboratory* dusty plasmas began in earnest in the late 1980s in the silicon microchip manufacturing industry, when Selwyn accidentally

discovered dust electrically suspended above microchips made in a plasma processing device [45].

In this industry, dust is a problematic contaminant, whose presence can cause shorts between the fine components of a microchip. Much cost and effort is expended on building advanced clean rooms to avoid dust contamination, but Selwyn discovered that a significant source of this contamination is dust generated by the industrial process itself, or else etched from the walls of the vacuum vessels in which these processes are performed. Thus, much of the early focus of laboratory dusty plasma research focused on the mitigation of dust contamination in these processing devices. These days, dust mitigation research is ongoing, but results tend to be the closely-guarded intellectual property of silicon manufacturing companies.

In the laboratory, dusty plasmas dynamics are a robust research topic in their own right. Dust in plasma is typically studied by illuminating the dust with monochromatic laser light and observing the Mie scattering of the light from the dust. In this way, dust particles are observed with the naked eye (so to speak – please wear eye protection when operating lasers). More importantly, dusty plasmas may be observed with off-the-shelf cameras and optics for use in the visible light range.

Because the dynamics of the dust particles are so easily recorded and studied, dust particles in plasma are a convenient vehicle for studying the plasmas in which they are immersed. Further, dusty plasmas represent a macroscopic, easily observed way to study fully classical analogues of concepts and interactions important in the fields of solid state physics, chemistry, statistical mechanics, and others.

1.2.1 Forces on Dust Particles

Electric and gravitational forces are typically the dominant dust forces for Earth-based experiments. Gas drag and ion drag are also usually important. Other forces are usually only important when intentionally introduced by the researcher, such as by

applying heat to an electrode to introduce a thermophoretic force away from the heat source.

As for the electric force on a dust particle, recall that bulk plasmas are quasineutral (Section 1.1.3), whereas plasma sheaths are characterized by large potential gradients (Section 1.1.6). A consequence of this is that, in the presence of appreciable gravitational force, dust typically may only levitate in a plasma sheath, where an upwards electric force may balance out the gravitational force.

$$\mathbf{F}_g + \mathbf{F}_E = 0. \tag{1.22}$$

More explicitly, the dust particle levitates at some height, y, where,

$$m_d \mathbf{g} + Z_d e \mathbf{E}(y) = 0, \tag{1.23}$$

where m_d is the dust mass, $\mathbf{g}$ is the acceleration due to gravity, and z_d is the number of elementary charges on the dust particle. The levitation height of the dust particle, then, is determined by the balance between the dust particle mass and the dust particle charge.

1.2.2 Dust Charge

Dust particles immersed in plasma collect charges from various sources until a steady-state surface potential, ϕ_d, is found, where charging currents are in equilibrium. The primary currents determining the dust charge in laboratory plasmas are the collection of electrons and ions. Because of the much higher electron mobility relative to ion motion, laboratory dust typically acquire highly negative net charge. In astrophysical plasmas, photoelectric charging and secondary electron emissions can also be important or even dominant, and thus dust particles in space may even acquire net positive charge.

The OML Model

The most common method for calculating dust charge is to assume conservative potentials for electron and ion motion, which is to say that electrons and ions are collisionless. This charging model is called Orbital Motion Limited (OML) theory, which was originally developed with Langmuir probes in mind [38, 60], which we shall discuss in Section 1.3. OML theory is so-named because it neglects ion currents from decaying (collisional) ion orbits. In OML theory, the capture of such an ion is incorrectly identified as scattering event between the dust and ion. Regardless, OML theory is considered to be a good model for dust particles smaller than the Debye length, λ_D [32, 25, 50].

Because we have assumed collisionless motion, we may write the dust's collection currents for electrons and ions purely in terms of kinetic energy distributions. Expressed as a function of dust ϕ_d, the electron and ion currents for a dust particle of radius, r_d, are

$$I_e(\phi_d) = -en_e\sqrt{\frac{k_B T_e}{m_e}}e^{e\phi_d/k_B T_e}4\pi r_d^2 \tag{1.24}$$

and

$$I_i(\phi_d) = en_i\sqrt{\frac{k_b T_i}{m_i}}\left(1-\frac{e\phi_d}{k_B T_i}\right)4\pi r_d^2 \tag{1.25}$$

where T_α is the kinetic temperature of species α (usually expressed in units of eV). We have here assumed that electrons follow the Boltzmann distribution and that ions obey the Bohm criterion. We find ϕ_d by requiring that the dust be in a steady state, $I_i + I_e = 0$. Using the above expressions, we find that

$$n_i\left(1-\frac{e\phi_d}{k_B T_i}\right) = n_e\sqrt{\frac{Te}{Ti}}e^{e\phi_d/k_B T_e}, \tag{1.26}$$

which we may solve to find ϕ_d. With dust potential in hand, dust charge is typically found by assuming a simple capacitive relation between dust charge, Q, and potential:

$$Q = C\phi, \tag{1.27}$$

with the capacitance, C, of a spherical dust particle of radius, r_d,

$$C = 4\pi\epsilon_0 r_d. \tag{1.28}$$

Overall, dust charge is weakly dependent on n_e and n_i and strongly dependent on T_e and r_d. For laboratory plasmas, dust particles of radius in the range of $1 - 10\mu m$ can typically be expected to collect net charges in the range of $10^3 - 10^4$ electron charges. These absorbed charges may constitute an appreciable fraction of the available electrons in the plasma, leading to a modified quasineutrality condition for dusty plasmas:

$$n_i - n_e - zn_d \approx 0, \tag{1.29}$$

where n_α is the number density of species α. The phenomenon of electron density being suppressed by dust charging is usually expressed using the Havnes parameter:

$$P_H = \frac{zn_d}{n_i}. \tag{1.30}$$

Measuring Dust Charge

Dust charge is one of the most important parameters describing dusty plasma phenomena [35, 42], but it is difficult to directly measure, as one cannot physically access the dust particles without greatly perturbing the plasma around them, and therefore changing the dust charge. However, dust charge can sometimes be determined by observing the motion of the dust particles.

One method of determining dust charge is to observe a collision between dust particles [29, 30]. By measuring the trajectories and deflection of the particles, one can determine the strength of their Yukawa-screened interaction, and thus measure the dust charge. Another method of determining dust charge from dust motion is to analyze

dust acoustic density waves (DAWs) [36]. The dispersion relations of these compressional waves through a dust cloud are strongly dependent on dust particle charge, and are a good way to measure it [52, 57, 53, 3]. Other ways of approximating dust charge analyze the position and motion of individual particles, for example by using the levitation condition in the sheath, $q_{dust}E = m_{dust}g$, and studying the oscillation frequencies of particles in the sheath. None of these methods are without assumptions, and they produce particle charge estimates of low accuracy.

1.2.3 Dust Crystals

The biggest watershed event in the field of dusty plasmas was the discovery of 2-dimensional dust crystals in the mid 1990s [13, 20, 54]. First predicted by Ikezi in the mid 1980s [23], dust crystals demonstrate that dust in plasma can exhibit collective and statistical behavior such as phase transitions. Moreover, because dust can so easily be observed using illumination lasers and video cameras, dusty plasmas are a particularly convenient way to study these topics.

It is natural to wonder if a dust crystal may be constructed in three dimensions. For ground-based experiments, the answer so far seems to be "only somewhat." Dust bilayers may be readily constructed using dust particles of multiple sizes, and this can be extended somewhat to several layers of dust particles, in structures sometimes referred to as 2.5D systems. One can force monodisperse dust to form long "chains" via tight confinement. Additionally, one can sometimes construct Yukawa balls via long hours of trial and error. The ion drag and its associated wake force is simply too disruptive in the sheath for a satisfying 3D extension of 2D dust crystals.

So, one might ask, how do we get out of the sheath? One way is to use very small particles ($< 1\mu$m in diameter, say), but optically observing the dynamics of very fine particles is often more difficult than for microparticles. Another way is to go to space.

1.2.4 Microgravity

By removing the gravitational force effects from experiments, we can unlock the bulk plasma for dusty plasma experiments. Microgravity conditions can be achieved in several ways. Drop towers can achieve microgravity conditions for an experiment lasting a few seconds. Sounding rockets can achieve hundreds of seconds, but you only get one shot per rocket launch. Parabolic flights can achieve repeated periods of microgravity lasting 30 to 45 seconds each, interspersed with periods of approximately doubled gravity. More, parabolic flight experiments are typically performed with the researchers on board, able to interact directly with the experiment to achieve the desired experimental conditions. For experiments intended to last longer than this, the best option is to conduct the experiment aboard the International Space Station (ISS).

Space station experiments present an interesting set of challenges not present in other microgravity experiments. Perhaps the largest practical and logistical difference is that the experimental apparatus will be sent to the ISS for a predetermined stretch of time, and then no plasma physicist will physically interact with this experiment until it returns to Earth. The apparatus must be designed with the understanding that alterations or repairs are very difficult, and sometimes impossible, during the experimental campaign.

It is primarily for this reason that no ISS or Mir dusty plasma experiment has ever featured a Langmuir probe [39, 55, 15]. If, for example, a motor were to fail and leave an actuated probe protruding into the plasma volume, this could seriously hamper the rest of the (very expensive) experimental campaign.

1.3 LTP Diagnostic Methods

1.3.1 Langmuir Probes

Langmuir probes are simultaneously the gold standard for LTP diagnostics, and also somewhat incompatible with dust. The development of these probes represent some

of the earliest works in experimental plasma physics [58, 38] and continue to be a ubiquitous diagnostic device for LTPs.

The basic concept of a Langmuir probe is to apply a known voltage to the probe tip immersed in the plasma, and to record the resulting current flowing to or from the probe. Typically, a Langmuir probe is operated by sweeping the applied voltage across a wide span of values in the range of tens of volts positive and negative. The resulting voltage vs current graph is analyzed to determine plasma parameters [1].

Immersing a probe tip into a plasma will intrinsically perturb the plasma as well as any dust that plasma may contain. But the process of sweeping the voltage makes the perturbation even stronger. This effect is especially troublesome for dusty plasmas – at high positive voltages, the probe tips tend to collect dust particles and become contaminated, at high negative voltages, probe tips create very large dust voids, completely altering the dusty plasma, whose plasma parameters one is presumably attempting to measure [28, 27]. Much work has been done in this area to attempt to mitigate these effects on Langmuir probe measurements [59, 6]. Much work has also been done to characterize these probe-induced voids [56, 34, 44, 26, 19, 18, 47, 48, 16].

1.4 Impedance Probes

There are many measurement techniques that can be achieved by applying electrical perturbations in various frequency ranges to langmuir probes and measuring the plasma response [14]. Broadly speaking, we refer to such measurements utilizing radio-frequency (RF) signals as plasma impedance probes (PIPs).

Said another way, PIPs are instruments used for performing active plasma resonance spectroscopy, wherein a low-power RF signal is applied to a plasma, and the plasma response to this signal is analyzed to diagnose plasma parameters. There are various designs of impedance probe, and they are appropriate for different applications.

1.4.1 Early Work

To the author's knowledge, the first instance of an RF probe used in plasma was the work of K. Takayama and H. Ikegami in 1960 [49], in which the nonlinearity of the sheath impedance was investigated. A planar probe (2 cm diameter nickel disk) was immersed in plasma, and an RF signal was applied to the probe, as well as a possible DC offset. For RF voltage magnitudes ranging from 0.2 V to 0.8 V, the RF frequency was swept across a broad frequency range, and the experimenters monitored the DC component of the probe current. They observed three distinct frequency regimes. At low frequency ($\omega << \omega_{pe}$), the DC current was constant with applied frequency, but increased with increasing RF voltage. At $\omega \approx \omega_{pe}$, the DC current spiked in a sharp resonance behavior. And at $\omega >> \omega_{pe}$, the DC current fell off towards a constant value, independent of both RF frequency and RF voltage.

This result is interpreted in light of the motion of the electrons as they react to the applied RF signal. The negative voltage half-cycle of the RF signal pushes electrons away from the probe tip, but the positive voltage half-cycle cannot efficiently pull the electrons back towards the probe because of screening effects. This results in an electron beam directed away from the probe tip, and the measured increase in net current into the probe. At $\omega << \omega_{pe}$, this effect is independent of frequency, it only depends on the magnitude of the applied RF voltage. As ω is increased towards ω_{pe}, the electron beam current density increases dramatically as the applied signal becomes resonant with the natural fluctuations of the electrons. And as ω passes the resonance, the electrons are no longer able to react at all to the RF signal, and no electron beam is created in the plasma.

These effects become smaller for lower voltages. The voltages applied by the device used in this dissertation work are an order of magnitude smaller than those in this paper, and this effect is not considered in the analysis.

Similar works in this vein were continued throughout the 1960s and 1970s [22, 17]. These days, PIPs are most commonly used for space plasmas and plasmas high in Earth's atmosphere [46].

1.4.2 Models

Measuring plasma parameters from PIP spectra must be done using some plasma physics model, and many choices are available. Kinetic theory approaches [33, 40] offer a powerful theoretical basis for PIP analysis. Lumped element models, wherein the continuous plasma medium is modeled as a series of discrete circuit elements [8, 9], are convenient options for their more direct analysis.

Lumped circuit models do require a great deal of measurement and/or modeling to correctly identify the values of the circuit elements involved. The approach we will take in this dissertation, is to geometrically solve for the relevant plasma capacitances, and to use a plasma fluid model to interpret the electron motion as inductors and resistors. Ions may also be taken into account, but in this work, we shall only consider frequencies at which the ion contribution is negligable.

The inductance and resistance in such a model describe the inertia of the electrons and the drag forces operating on those electrons, respectively. Consider the sudden application of an electric field to a single electron at rest in an otherwise neutral gas. The electron will not immediately be moving as the field is applied, the electron will have to accelerate for some small time before coming up to its terminal velocity. So current follows voltage, and this current ramps from zero up to some maximum value. The behavior we are describing is the same behavior as the electric current passing through an inductor in series with a resistor.

1.4.3 Probe Design

The possible designs for RF impedance measurement devices are myriad, but we shall shortly describe several common probe designs. Figure 1.3a depicts the simplest probe

design: a single-tipped impedance probe used for RF reflection measurements. The probe tip may be of various geometries; dipole probes [7, 46] (depicted in Figure 1.3b), spherical [8, 9], and planar [22, 43] probe tips are all used. These probes may also be used as single-tipped Langmuir probes, but for RF measurements, the wire leading to the probe tip must be adequately RF-shielded.

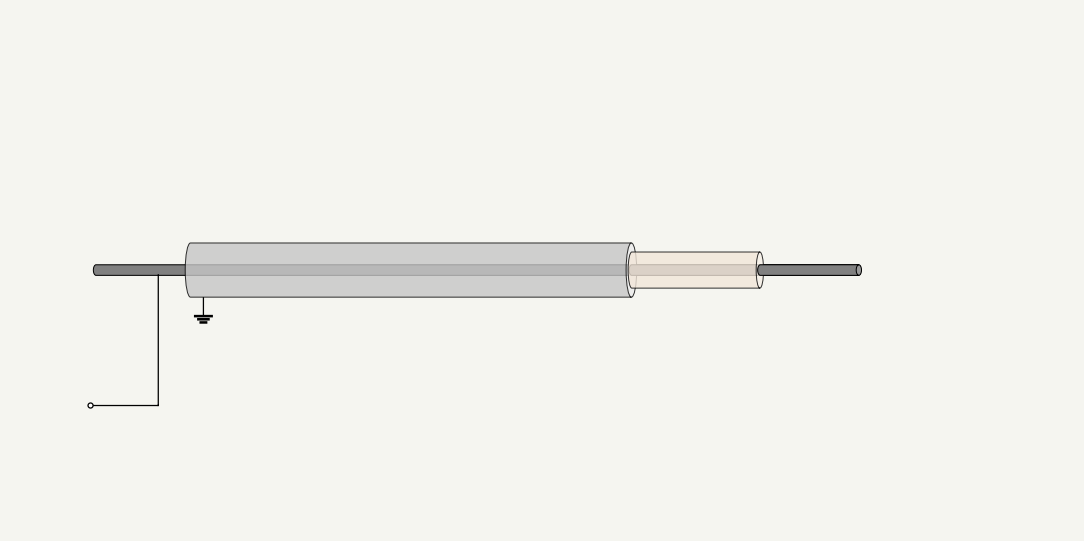

(a) A single-tipped cylindrical impedance probe

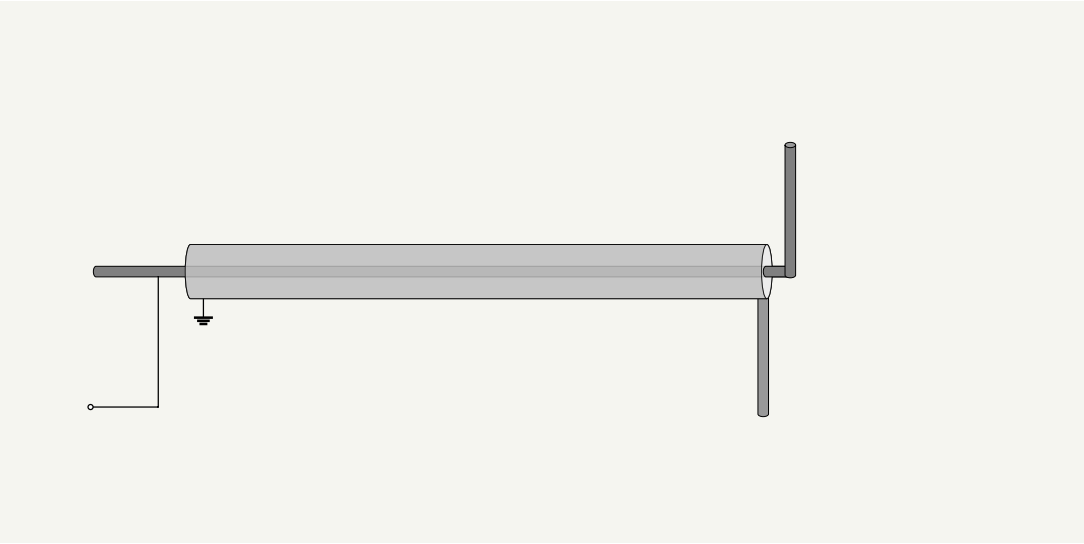

(b) A dipole impedance probe

Figure 1.3: RF Reflection Probes

Figure 1.4 depicts two different styles of transmission probes, which are the focus of this dissertation. Figure 1.4a shows two single-tipped cylindrical probes, to be immersed in the same plasma and used for RF transmission measurements. Figure 1.4b shows a similar setup with both probe tips threaded through the same probe body.

The biggest difference between these two probes is that the probe tips in Figure 1.4b are likely to be within each other's plasma sheathes, whereas the probe tips in Figure 1.4a are likely to be separated from each other by the bulk plasma.

These probes are functionally identical to double-tipped Langmuir probes at low frequency, and may directly be used as such. As stated above, these probes are unlike typical Langmuir probes in that they are shielded for use with radio frequency signals. They are also unlike some other RF probe designs because their RF behavior is capacitor-like instead of wave-like; these transmission-probes operate in the near-field limit of the applied RF signal.

In a glow discharge plasma, electrons are mobile enough that T_e is expected to be approximately constant across the entire space. However, n_e may vary greatly in the plasma chamber. One advantage of transmission-type impedance probes for use these plasmas is that the transmission spectra measured are separately sensitive to plasma parameters near the probe tips compared to plasma parameters farther away in the plasma. This separate sensitivity for n_e will be demonstrated (in simulations) in Section 4.3.

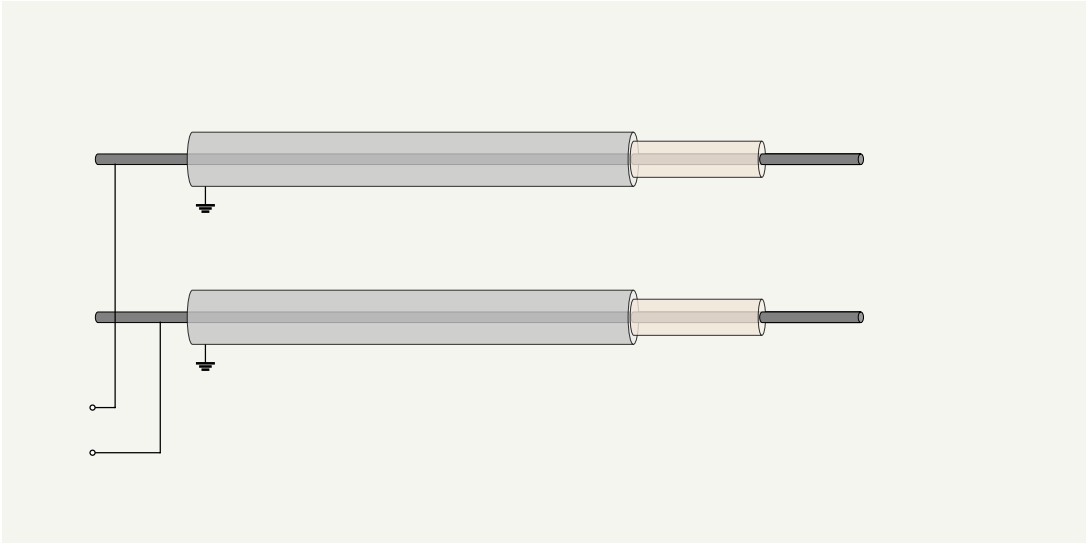

(a) Two single-tipped cylindrical impedance probes

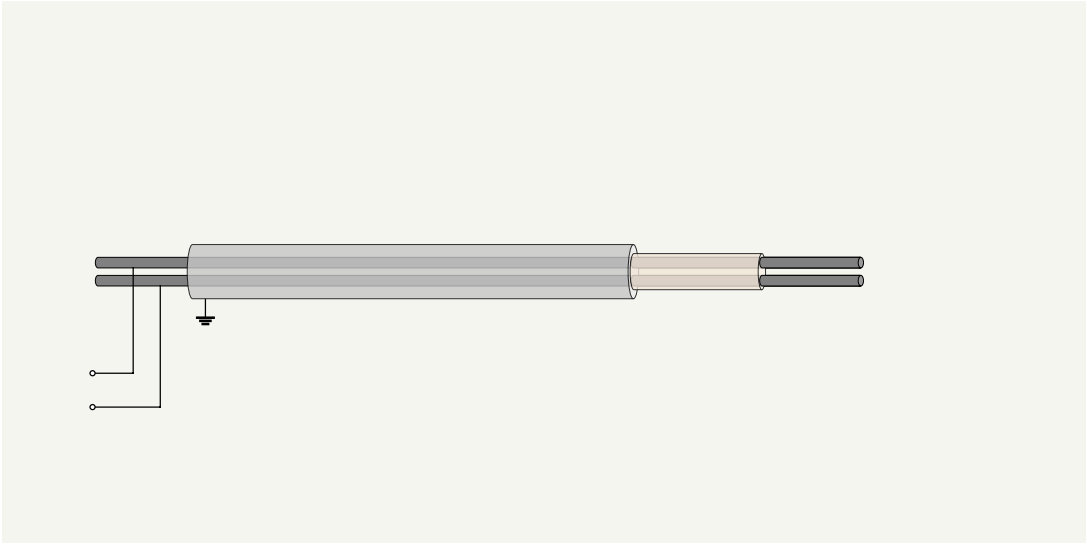

(b) A double-tipped cylindrical impedance probe

Figure 1.4: RF Transmission Probes

Chapter 2

Theory

2.1 Impedance Probes

Impedance probe diagnostics are a type of active plasma resonance spectroscopy useful for measuring electron density and temperature in low-temperature plasmas in laboratory environments [58, 49, 8] and in atmospheric and space environments [46].

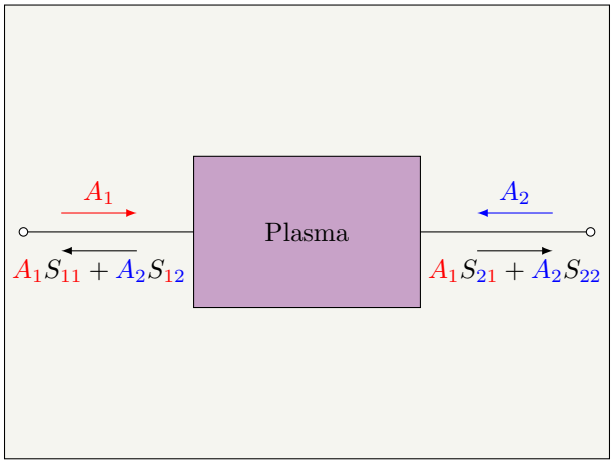

Figure 2.1: Reflection and transmission characteristics are often expressed with S-parameters. A Vector Network Analyzer (VNA) measures the impedance of the device under test by applying a known signal (A_1) and measuring either the reflected signal (A_1S_{11}) or transmitted signal (A_1S_{21}).

An impedance probe utilizes a Vector Network Analyzer (VNA), or an equivalent measurement device, to measure the plasma's frequency-dependent response to low-power radio signals. Plasma parameters are determined from analysis of resonances at or near the electron plasma frequency, ω_{pe}. For relatively steady-state plasmas, such

as most low temperature laboratory plasmas, the input signal is typically swept in frequency, with one VNA spectrum taking a few seconds to tens of seconds to measure.

A VNA running an impedance probe measures plasma impedance by comparing the VNA output signal (A_1) to the signal reflected back from the plasma ($A_1 S_{11}$), or the signal transmitted through the plasma ($A_1 S_{21}$), with S-parameters defined as shown in Figure 2.1. Transmission-type impedance probes (Figure 2.2) may have some advantages for use with dusty plasmas, and these are the probes used in experiments presented in this work.

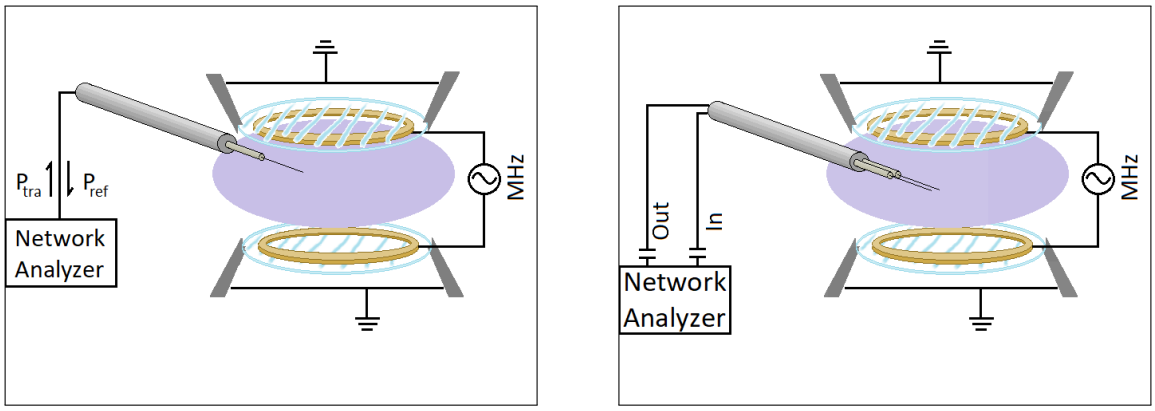

Figure 2.2: A reflection-type impedance probe (left) determines plasma parameters by analyzing reflected (S_{11}) signal from the probe tip. A transmission-type impedance probe (right) determines plasma parameters by analyzing transmitted (S_{21}) signal through the plasma chamber.

To relate the S-parameters to the electron plasma density, n_e, we model the plasma as a simple circuit composed of discrete ("lumped") circuit elements (Figure 2.3). These lumped circuit elements approximate the collective behavior of the continuous plasma. The electron temperature, T_e, may also be found from this model, but it requires more careful analysis than does n_e.

2.2 Circuit Model

Consider the case of a single-tipped probe (Figure 2.3a). The plasma sheathes are assumed to be completely free of electrons ($n_e = 0$), and are therefore modeled simply as capacitors, whose values are calculated from the geometry of the probe and plasma

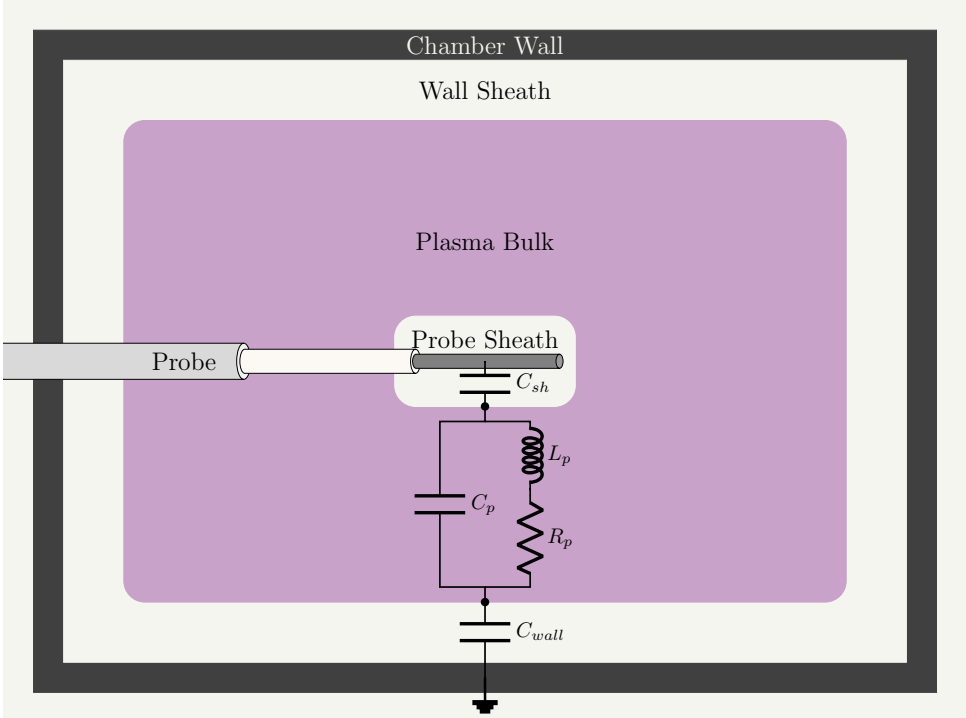

(a) Single-Tipped Probe

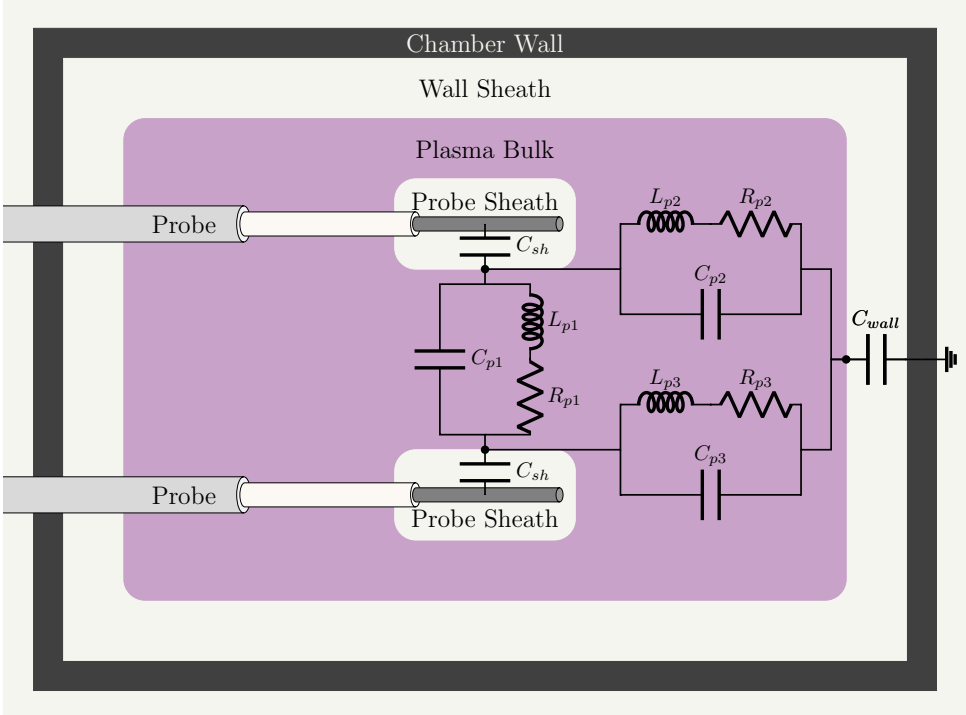

(b) Double-Tipped Probe

Figure 2.3: Plasma circuit model for impedance probes operating in (a) reflection mode with a single-tipped probe, and (b) transmission mode with either one double-tipped probe or two single-tipped probes.

chamber, as well as the thickness of the sheathes around the probe and at the wall. Sheath thicknesses are calculated as described in Section 4.1.1.

For the bulk plasma, an applied signal is transmitted in two ways: via direct capacitive coupling across the bulk volume, and via electron motion. Ion motion is neglected, because it occurs on a much slower time scale. The bulk plasma is thus modeled as a capacitance (C_p) between the relevant sheath boundaries, in parallel with an inductance (L_p) and resistance (R_p), which together describe the collective motion of electrons. C_p is calculated geometrically, similarly to the sheath capacitance, whereas L_p and R_p are determined from a fluid model for the bulk plasma. In the next section, we shall show that, these circuit element values are approximately,

$$L_p \approx \omega_{pe}^{-2} C_p^{-1}, \tag{2.1a}$$

and

$$R_p \approx \nu L_p, \tag{2.1b}$$

where ω_{pe} is the electron plasma frequency, and ν is the frequency for electron momentum loss, which for these plasmas is simply the electron-neutral collision frequency.

2.3 Fluid Model for Bulk Plasma

These expressions for L_p and R_p come from the fluid model plasma impedance, which may be derived from the momentum equation for electrons,

$$\frac{D\mathcal{P}_e}{Dt} = \mathcal{F}_{Lorentz} + \mathcal{F}_{collisions} + \mathcal{F}_{pressure} + \ldots, \tag{2.2}$$

where $\mathcal{P}_e$ is the electron momentum density, and $\mathcal{F}$ are the various force densities. Here, we include only the Lorentz force and forces from electron-neutral collisions and electron pressure gradients. The convective derivative, D/Dt, is the time derivative

in the reference frame that follows the motion of the plasma fluid element. We write Equation 2.2 in the plasma chamber's reference frame and with explicit expressions for the included forces:

$$m_e \left[\frac{\partial}{\partial t} + (\mathbf{u} \cdot \nabla) \right] (n_e \mathbf{u}) = -e n_e (\mathbf{E} + \mathbf{u} \times \mathbf{B}) - n_e m_e \nu \mathbf{u} - \gamma k_B T_e \nabla n_e, \tag{2.3}$$

where m_e is the electron mass, $\mathbf{u}(\mathbf{x}, t)$ and $n_e(\mathbf{x}, t)$ are the electron fluid velocity and number density, $\mathbf{E}(\mathbf{x}, t)$ and $\mathbf{B}(\mathbf{x}, t)$ are the electric and magnetic fields, ν is the electron-neutral collision frequency for momentum transfer, k_B is the Boltzmann constant, T_e is the electron temperature, and γ is a dimensionless constant of order unity, whose value depends on the electron electron flux assumption. We may solve Equation 2.3 by linearizing the fluctuating quantities; $\mathbf{u}$, n_e, $\mathbf{E}$, and $\mathbf{B}$; in terms of plane wave solutions.

2.3.1 Plane Wave Solutions

Consider some quantity, α, which is characterized by a steady-state value, α_0, which is constant in time but not necessarily space, in linear combination with a small perturbation, $\widetilde{\alpha}$, which takes the form of a plane wave oscillation. We may write,

$$\alpha(\mathbf{x}, t) = \alpha_0(\mathbf{x}) + \widetilde{\alpha}(\mathbf{x}, t), \tag{2.4a}$$

with

$$\widetilde{\alpha}(\mathbf{x}, t) = \alpha_1 e^{i(\omega t - \mathbf{k} \cdot \mathbf{x})}, \tag{2.4b}$$

where i is the imaginary unit, $i = \sqrt{-1}$. We could have equivalently defined $\widetilde{\alpha}$ in terms of sines and cosines, but we have used Euler's Identity, $exp(\pm i\theta) = cos(\theta) \pm i\, sin(\theta)$, to write these oscillations as exponential expressions. We do this so that the spatial and time derivatives of $\widetilde{\alpha}$ may be conveniently written as,

$$\frac{\partial}{\partial t} \widetilde{\alpha} = +i\omega \widetilde{\alpha} \tag{2.5a}$$

$$\nabla \widetilde{\alpha} = -i\mathbf{k} \widetilde{\alpha} \tag{2.5b}$$

$$\nabla \cdot \widetilde{\alpha} = -i\mathbf{k} \cdot \widetilde{\alpha} \tag{2.5c}$$

$$\nabla \times \widetilde{\alpha} = -i\mathbf{k} \times \widetilde{\alpha} \tag{2.5d}$$

The signs of the exponential term in Equation 2.4b are arbitrary and chosen for convenience. We choose the sign of $+i\omega t$ because it will produce expressions for plasma impedance which conform to the convention that inductive reactance is positive and imaginary, and capacitive reactance is negative and imaginary. Meanwhile $-i\mathbf{k} \cdot \mathbf{x}$ takes the opposite sign to conform to the convention that the $+\hat{\mathbf{k}}$ direction indicates the plane wave's direction of propagation.

To solve Equation 2.3, we assume that the quantities, $\mathbf{u}$, n_e, $\mathbf{E}$, and $\mathbf{B}$ take the form of Equations 2.4 and 2.5. We will further assume that there is no steady-state flow of electrons ($\mathbf{u}_0 = 0$), but do not yet make any such restriction for $\mathbf{E}_0$, $\mathbf{B}_0$, or n_{e0}:

$$\mathbf{u} = \cancelto{0}{\mathbf{u}_0} + \widetilde{\mathbf{u}}, \tag{2.6a}$$

$$\mathbf{E} = \mathbf{E}_0 + \widetilde{\mathbf{E}}, \tag{2.6b}$$

$$\mathbf{B} = \mathbf{B}_0 + \widetilde{\mathbf{B}}, \tag{2.6c}$$

$$n_e = n_{e0} + \widetilde{n}_e. \tag{2.6d}$$

2.3.2 Ohm's Law

We may now use Equations 2.5 and 2.6 to linearize the fluid momentum equation (Equation 2.3),

$$\begin{aligned} m_e \left[\frac{\partial}{\partial t} + (\widetilde{\mathbf{u}} \cdot \nabla)\right] ((n_{e0} + \widetilde{n}_e)\, \widetilde{\mathbf{u}}) = \\ -e\,(n_{e0} + \widetilde{n}_e) \left(\left(\mathbf{E}_0 + \widetilde{\mathbf{E}}\right) + \widetilde{\mathbf{u}} \times \left(\mathbf{B}_0 + \widetilde{\mathbf{B}}\right)\right) - n_{e0} m_e \nu \widetilde{\mathbf{u}} - \gamma k_B T_e \nabla\,(n_{e0} + \widetilde{n}_e)\,, \end{aligned} \tag{2.7}$$

The 0^{th} and 1^{st} order fluctuations of Equation 2.7 become two separate equations. The 0^{th} order terms of Equation 2.7 obey,

$$0 = -en_{e0}\mathbf{E}_0 - \gamma k_B T_e \nabla n_{e0}, \tag{2.8}$$

or,

$$\mathbf{E}_0 = -\frac{\gamma k_B T_e}{e}\frac{\nabla n_{e0}}{n_{e0}}. \tag{2.9}$$

Meanwhile, the 1^{st} order terms of Equation 2.7 are,

$$i\omega m_e n_{e0}\widetilde{\mathbf{u}} = -e\left(\widetilde{n}_e\mathbf{E}_0 + n_{e0}\widetilde{\mathbf{E}} + n_{e0}\widetilde{\mathbf{u}}\times\mathbf{B}_0\right) - n_{e0}m_e\nu\widetilde{\mathbf{u}} + i\mathbf{k}\gamma k_B T_e\widetilde{n}_e. \tag{2.10}$$

Regrouping terms, we write,

$$\widetilde{\mathbf{u}}n_{e0}m_e(\nu + i\omega) = -en_{e0}\left(\widetilde{\mathbf{E}} + \widetilde{\mathbf{u}}\times\mathbf{B}_0\right) + \widetilde{n}_e\left(i\mathbf{k}\gamma k_B T_e - e\mathbf{E}_0.\right). \tag{2.11}$$

We now use Equation 2.9 to eliminate the explicit dependence on the steady state electric field from Equation 2.11, resulting in an equation of motion for the electron fluid in the plasma,

$$\widetilde{\mathbf{u}}n_{e0} = \frac{-en_{e0}}{m_e(\nu + i\omega)}\left(\widetilde{\mathbf{E}} + \widetilde{\mathbf{u}}\times\mathbf{B}_0\right) + \frac{\gamma k_b T_e}{m_e(\nu + i\omega)}\left(\frac{\nabla n_{e0}}{n_{e0}} + i\mathbf{k}\right)\widetilde{n}_e. \tag{2.12}$$

We wish to obtain an expression for the plasma impedance by interpreting this electron motion as a version of Ohm's Law,

$$\mathbf{j} = \sigma\mathbf{E}. \tag{2.13}$$

To this end, we can relate $\widetilde{n}_e$ to $\widetilde{\mathbf{E}}$ using the 1^{st} order linearized Poisson' Equation,

$$\widetilde{n}_e = \frac{\epsilon_0}{e}i\mathbf{k}\cdot\widetilde{\mathbf{E}}, \tag{2.14}$$

and we can write $\widetilde{\mathbf{u}}$ as a 1^{st} order current density fluctuation,

$$\widetilde{\mathbf{j}} = -en_{e0}\widetilde{\mathbf{u}}. \tag{2.15}$$

We may now use Equations 2.14 and 2.15 to re-write Equation 2.12 into the following rather unweildly form,

$$\widetilde{\mathbf{j}} = \frac{1}{m_e(\nu + i\omega)}\left[n_{e0}e^2\left(\widetilde{\mathbf{E}} - \frac{1}{en_{e0}}\widetilde{\mathbf{j}} \times \mathbf{B}_0\right) - \epsilon_0\gamma k_B T_e\left(\frac{\nabla n_{e0}}{n_{e0}} + i\mathbf{k}\right)\left(i\mathbf{k}\cdot\widetilde{\mathbf{E}}\right)\right]. \tag{2.16}$$

In Equation 2.16, we notice that several common plasma quantities have amerged: ω_c, ω_{pe}, and λ_D are the electron cyclotron frequency, plasma frequency, and Debye length, respectively:

$$\omega_c = \frac{B_0 e}{m_e}, \tag{2.17}$$

$$\omega_{pe}^2 = \frac{n_{e0}e^2}{\epsilon_0 m_e}, \tag{2.18}$$

$$\lambda_D^2 = \frac{\epsilon_0 k_B T_e}{n_{e0}e^2}. \tag{2.19}$$

We use these quantities to rewrite Equation 2.16 as,

$$\widetilde{\mathbf{j}} + \left(\frac{\omega_c}{\nu + i\omega}\right)\widetilde{\mathbf{j}} \times \hat{\mathbf{b}}_0 = \sigma_0\left[\widetilde{\mathbf{E}} - \gamma\lambda_D^2\left(\frac{\nabla n_{e0}}{n_{e0}} + i\mathbf{k}\right)(i\mathbf{k}\cdot\widetilde{\mathbf{E}})\right], \tag{2.20}$$

where we have defined the quanitity,

$$\sigma_0 = \frac{\epsilon_0\omega_{pe}^2}{\nu + i\omega} = \frac{n_{e0}e^2}{m_e(\nu + i\omega)}, \tag{2.21}$$

where $\hat{\mathbf{b}}_0$ is the unit vector indicating the direction of the background magnetic field, $\mathbf{B}_0$, and σ_0 may be interpreted as the near-field plasma conductivity.

For the case that $\mathbf{B}_0 = 0$ and $\mathbf{k}||\widetilde{\mathbf{E}}$, and we simplify Equation 2.20 to,

$$\widetilde{\mathbf{j}} = \left[\sigma_0 - i\sigma_k(\hat{\mathbf{n}} \cdot \hat{\mathbf{k}}) - \sigma_{k^2}\right] \widetilde{\mathbf{E}} \tag{2.22}$$

with

$$\sigma_k \hat{\mathbf{n}} = \sigma_0 \gamma \lambda_D^2 k \frac{\nabla n_{e0}}{n_{e0}}, \tag{2.23}$$

and

$$\sigma_{k^2} = \sigma_0 \gamma \lambda_D^2 k^2, \tag{2.24}$$

where $\hat{\mathbf{k}}$ and $\hat{\mathbf{n}}$ indicate the directions of wave propagation and electron density gradient, respectively.

For the frequencies used in impedance probe measurements, and for the plasma conditions found in RF, capacitively-coupled glow discharge plasmas, it will always be true that,

$$\frac{\sigma_{k^2}}{\sigma_0} = \gamma \frac{\lambda_D^2}{\lambda_w^2} \ll 1, \tag{2.25}$$

where $\lambda_w = 1/k$ is the wavelength of the fluctuation. And so we may always neglect the effects of σ_{k^2} in this work.

The σ_k contribution will also be small in the plasma bulk, where ∇n_{e0} is small. But σ_k *can* be important in the plasma sheath, where ∇n_{e0} is large. For now, we limit our analysis to the plasma bulk, and therefore make the approximation that $\sigma \approx \sigma_0$.

2.3.3 Circuit Model Elements from Fluid Model

To find the total impedance related to this conductivity, we may in principal find the electric field by solving Poisson's Equation between the probe sheath and the wall sheath (recall Figure 2.3a), and then integrate $j = \sigma E$ in this region to find the total current flowing between the two sheathes for a given potential difference.

$$Z_{pe} = \frac{\Delta V}{I} = \frac{\Delta V}{\sigma \oiint\limits_{bulk} \widetilde{\mathbf{E}} \cdot \mathrm{d}\hat{\mathbf{S}}}, \tag{2.26}$$

where Z_{pe} is the impedance due to the electrons in the bulk plasma. In the circuit model for a single-tipped probe, it is related to the total impedance by,

$$Z = Z_{sheathes} + \frac{1}{\frac{1}{Z_{C_p}} + \frac{1}{Z_{pe}}}. \tag{2.27}$$

Meanwhile, the probe sheath and wall sheath also interact capacitively (Figure 2.3a). The capacitance of C_p is found the same way, by integrating along the electric field in the bulk region:

$$C_p = \frac{\widetilde{Q}}{\Delta V} = \frac{\epsilon_0 \oiint_{bulk} \widetilde{\mathbf{E}} \cdot \mathrm{d}\hat{\mathbf{S}}}{\Delta V} \tag{2.28}$$

The particular solutions to Equations 2.26 and 2.28 will depend on geometry. But in any geometry, we may write,

$$Z_{pe} = \frac{1}{\sigma}\frac{\epsilon_0}{C_p} = \frac{\nu + i\omega}{\omega_{pe}^2}\frac{1}{C_p} \tag{2.29}$$

We may interpret the imaginary and real parts of Equation 2.29 as an inductance with reactance, $X = \omega_{pe}^{-2} C_p^{-1}$, in series with a resistor with resistance, $R = \nu\omega_{pe}^{-2} C_p^{-1}$. And so the corresponding circuit elements in the circuit model have values given by Eqation 2.1:

$$L_p \approx \omega_{pe}^{-2} C_p^{-1}, \tag{2.1a}$$

and

$$R_p \approx \nu L_p, \tag{2.1b}$$

Chapter 3

Experiment

3.1 Plasma Devices

The Microgravity Plasma Lab (μg Lab) at Auburn University is a laboratory for terrestrial low temperature plasma research and for the development of experimental devices and techniques used in microgravity dusty plasma research. The experiments presented in this work were performed in two different plasma chambers at μg Lab: DODECA, which is an RF plasma device with a dodecahedral shape, and RaFyL, a cylindrical RF plasma device created for this work.

3.1.1 DODECA

DODECA is a device developed for studying dust voids in microgravity experiments with the design goal of creating a plasma with nearly (time-averaged) isotropic ion motion. DODECA was designed to be operated with twelve independently-powered electrodes in a dodecahedral formation. However, in this work, DODECA was operated with only seven electrodes installed: two powered electrodes at the top and bottom of the chamber and five grounded electrodes positioned around the bottom electrodes to form a "bowl." In this bowl, it was possible to create large dust clouds, about 3 cm tall. However, the complicated geometry of this orientation makes analysis of impedance probe data difficult, and there are often strong plasma density gradients in the volume. In fact, as we shall see, it often happens at low RF power that there

is only a suppressed or diffusive bulk plasma around the centrally-located impedance probe tips, making analysis of these low-power plasmas challenging if not impossible.

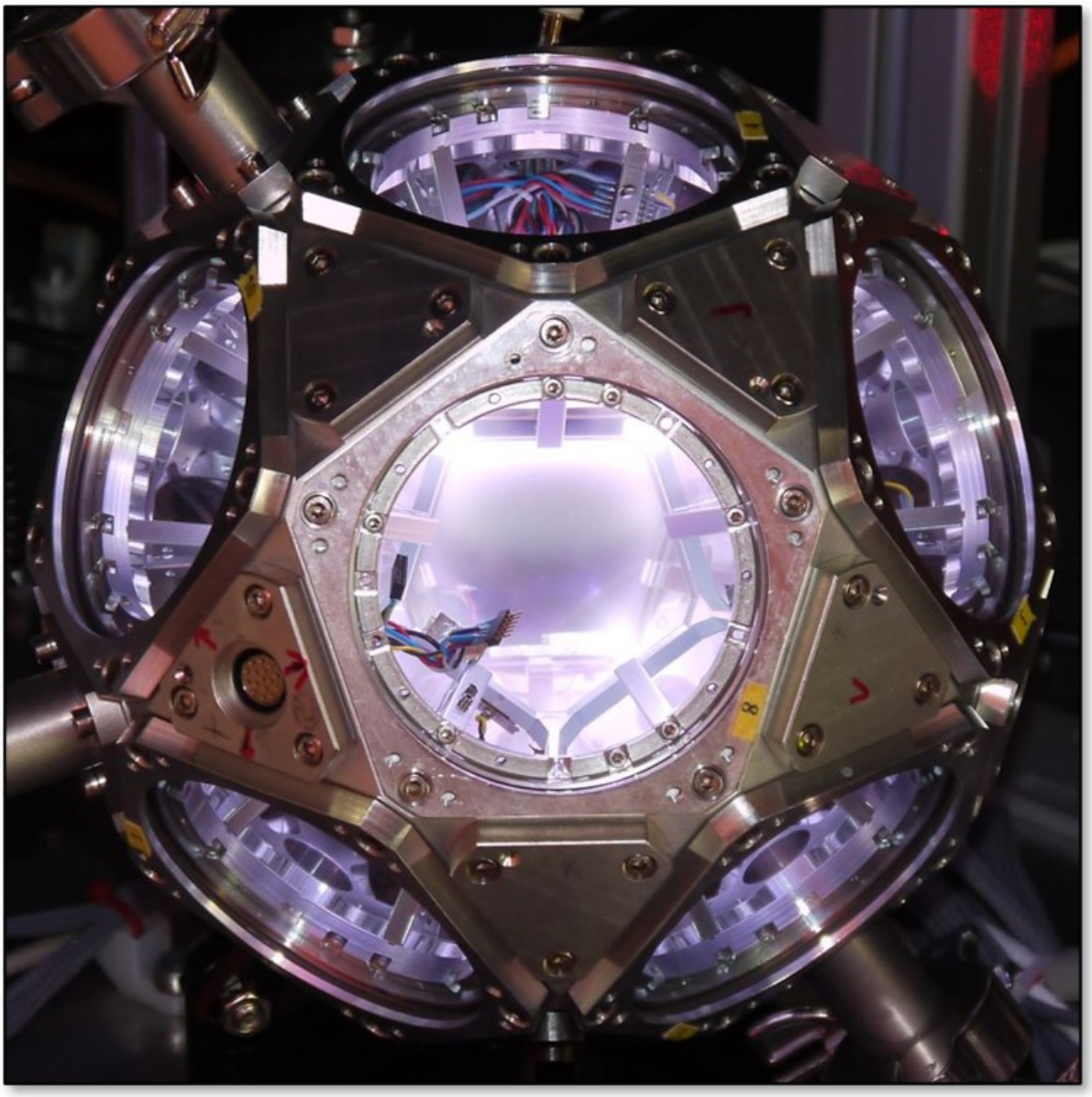

Figure 3.1: DODECA

3.1.2 RaFyL

RaFyL has a much simpler geometry: circular electrodes at the top and bottom of the chamber form a roughly cylindrical discharge. This configuration makes geometrical analysis of impedance probe measurements easier, but it is not as conducive to creating large dust clouds.

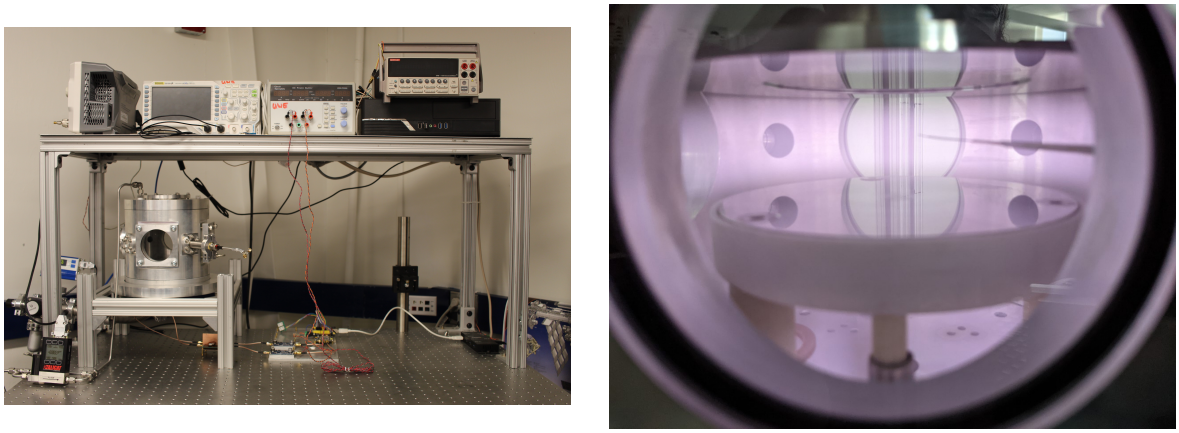

Figure 3.2: RaFyL

3.2 Impedance Probe

The impedance probes (Figure 3.4) are single- or double-tipped cylindrical probes with probe tips made of tungsten wire with a diameter 0.2 mm and a length varying between 1.5 and 2 cm. The single-tipped probes were used in conjunction – one was the broadcasting probe, and the other was the receiving probe. The double-tipped probes contained both probe tips within one 1/4 inch tube body. The probe tips were separated from the end of the tube body by a length of ceramic tube of length varying between 1 and 2 cm. These insulating tubes helped to lessen the plasma-bypassing coupling between the probe tips and the probe body. Each probe tip was connected to an RF-shielded wire that passed through the body of the probe, through a vacuum feedthrough, and terminating in an SMA connector. The probe wires in the body of the double-tipped probes were shielded both from each other and from outside RF sources and sinks.

3.3 Experimental Setup

A transmission-type impedance probe was immersed into a capacitively-coupled, RF plasma, and frequency-dependent transmission spectra were recorded.

Typical experimental parameters are listed in Table 3.1.

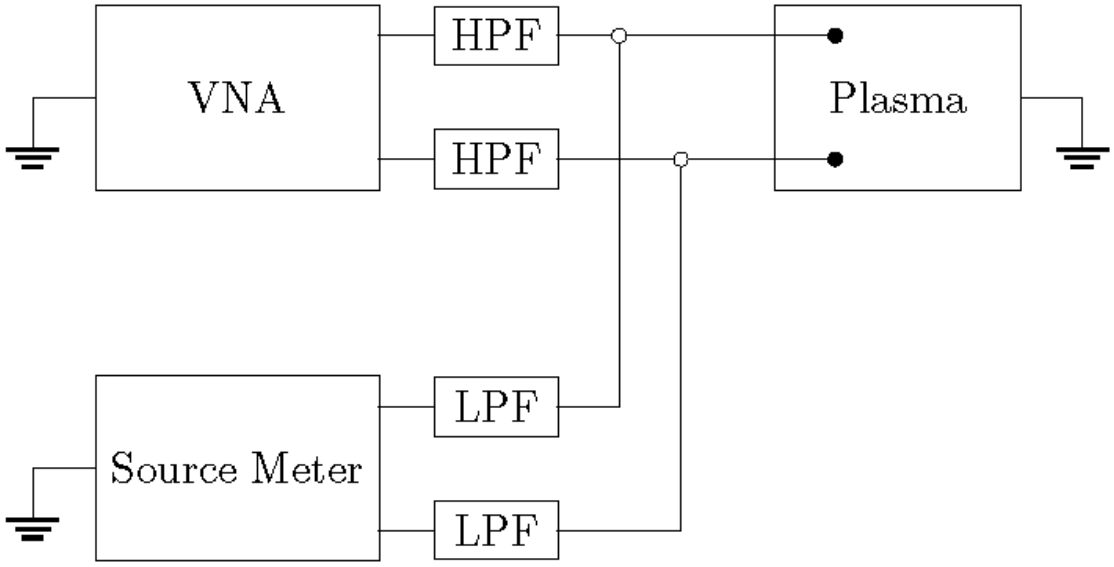

Figure 3.3: Circuit diagram for simultaneous RF and DC measurements.

These experiments were performed using automation software written as a part of this work. The software is written in C++ and makes use of Uwe Konopka's COPLA (COmplex PLasma Analysis) libraries, which are written in C. This COPLA-based control software uses serial and USB communication to interface with the various devices used; pressure transducers, mass flow controllers, RF measurement devices, and the like. The software controls the powered electrodes by interfacing with an Arduino

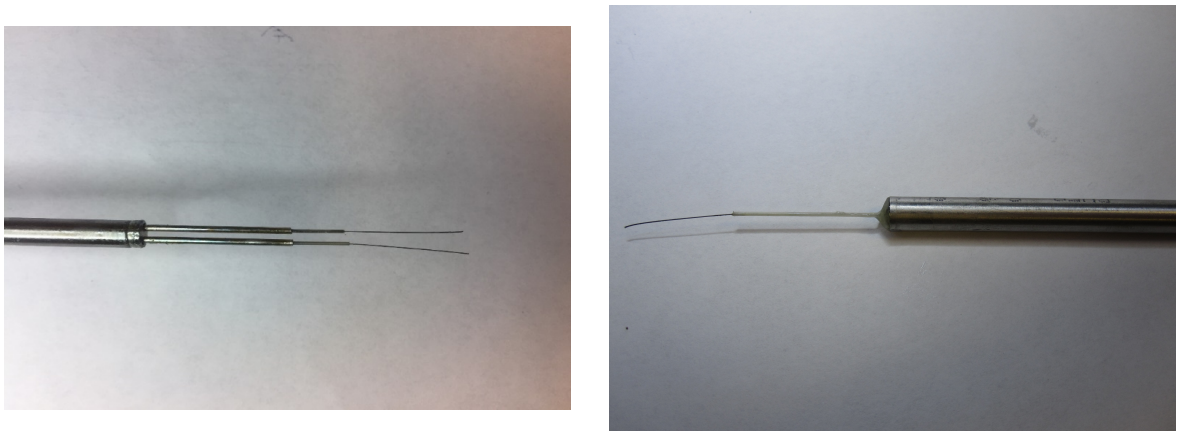

Figure 3.4: Impedance Probes

Experiments	
probe type	transmission
probe spacing	2..30mm
dust	None

Plasma Parameters	
T_e	~ 3 eV
T_i	0.025 eV
n_e	$\sim 10^{14}\ m^{-3}$
gas	Ar or Kr
P_{gas}	$1 \leftrightarrow 30\ Pa$

Table 3.1: Experiment Parameters

microcontroller, which in turn controls a 2-channel signal generator running off of an AD9959, and reading the output with AD8307 and AD8302 RF power and phase meters. This power supply is a prototype for an 8-channel signal generator (using two AD9959s) in development at μg-Lab, but only the 2-channel version was required for data collected for this work. The control software written for the Arduino makes use of the AD9959 Arduino library written by Clifford Heath, of GitHub username, "cjheath" [21].

3.4 Results and First Analysis

An example sweep of spectra is shown in Figure 3.5. These data were taken in the DODECA plasma chamber with a switched-DC plasma created by power inverter with oscillation frequency on the order of 10 kHz. Each vertical spectrum shows the transmission power gain due to the plasma. That is to say, at each inverter power on the X axis, the vertical spectrum shows the transmitted RF power with the plasma turned on minus the transmitted RF power in the chamber with the plasma off. The analysis of this dissertation focuses on the plasma resonances seen at approximately 0-200 MHz. But standing wave resonances are also visible at higher frequencies, and it should be noted that these resonances also contain information about the plasma.

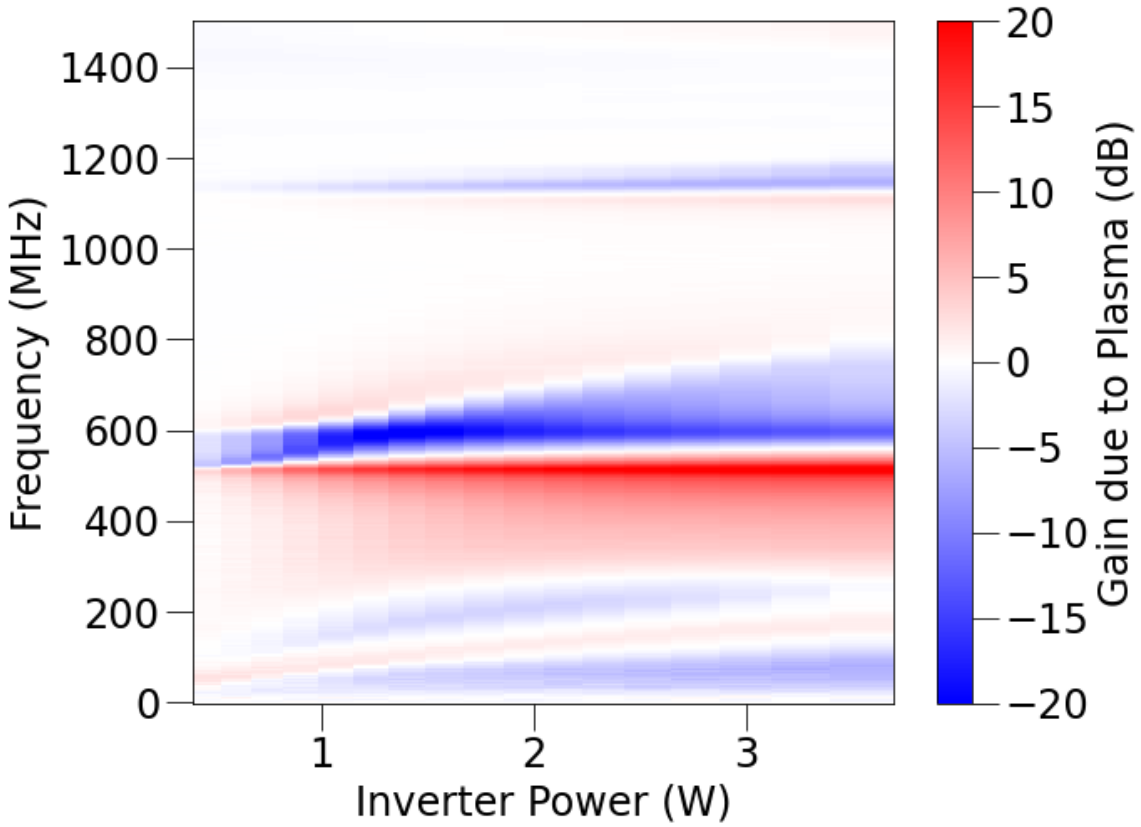

Figure 3.5: Example data taken in the DODECA plasma chamber with a switched-DC plasma created by a power inverter. From low to high frequency, the visible features in this power sweep show the plasma resonance (approx. 0-200 MHz), the chamber standing wave resonance (approx. 300-800 MHz), and another resonance (approx. 1150 MHz), which is likely a 2^{nd}-order resonance of the chamber standing wave.

3.4.1 Qualitative Fitting

The experimental spectra were fit using a linear combination of two Gaussian curves, each representing the reflection and absorption of power by the plasma near its plasma frequency (Figure 3.6). One Gaussian curve represents the suppression of transmitted power by plasma elements encountered along the electric field lines between the two probe tips. The other represents the *increase* of power transmitted between the probe tips because of the reflection of power between each probe tip and the grounded chamber wall. This second Gaussian curve should be understood to represent the conservation of energy in the system – power impeded from going to the chamber wall must either reflect back into the transmitting probe or it must be absorbed by the receiving probe. The average plasma density will be different along the transmission paths from probe to probe as compared to the transmission paths from probe to wall, and therefore these curves will not be centered around the same frequency.

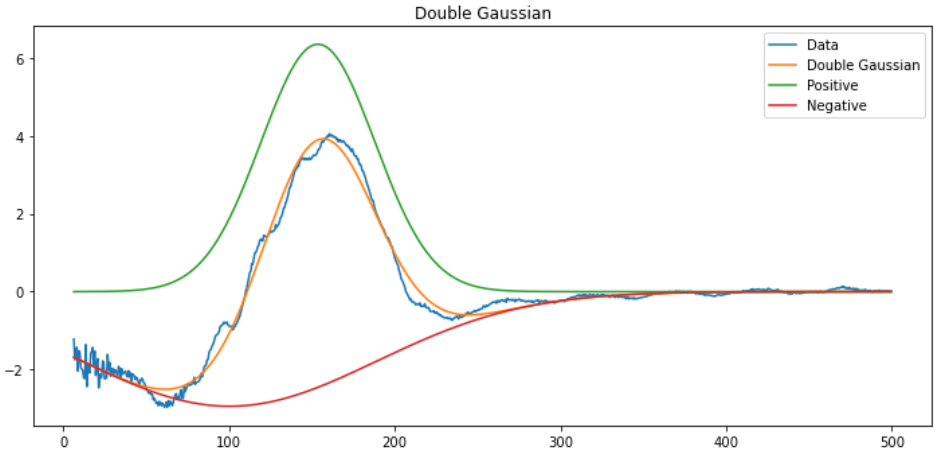

Figure 3.6: The experimental spectra of the gain due to plasma may be fit with two gaussian curves, one positive and one negative. X axis: frequency in MHz. Y axis: gain due to plasma. The blue line is an experimental transmission spectrum with no plasma minus the same spectrum without plasma in the chamber. The yellow line is the fit. It is a linear combination of a positive Gaussian curve (green) and a negative Gaussian curve (red). The negative gaussian curve should be understood to represent the plasma interfering with the probe-probe transmission near ω_{pe}. The positive curve represents the plasma interfering with the probe-wall transmission in the same way. Because energy is conserved, the decrease of energy flowing to the wall must be accounted for by an increase of energy being reflected back into the transmission probe and/or being transmitted to the receiving probe.

As shown in Figure 3.7, this method of curve fitting produces plots that visually match the experimental data very well. Table 3.2 shows an example set of fit parameters for the last electrode voltage plotted in Figure 3.7. Figure 3.8 shows the positive and negative central frequencies and associated uncertainties for all spectra, plotted over the raw data. It also shows the Full Width Half Maxima of these curves, but does not show the related uncertainty.

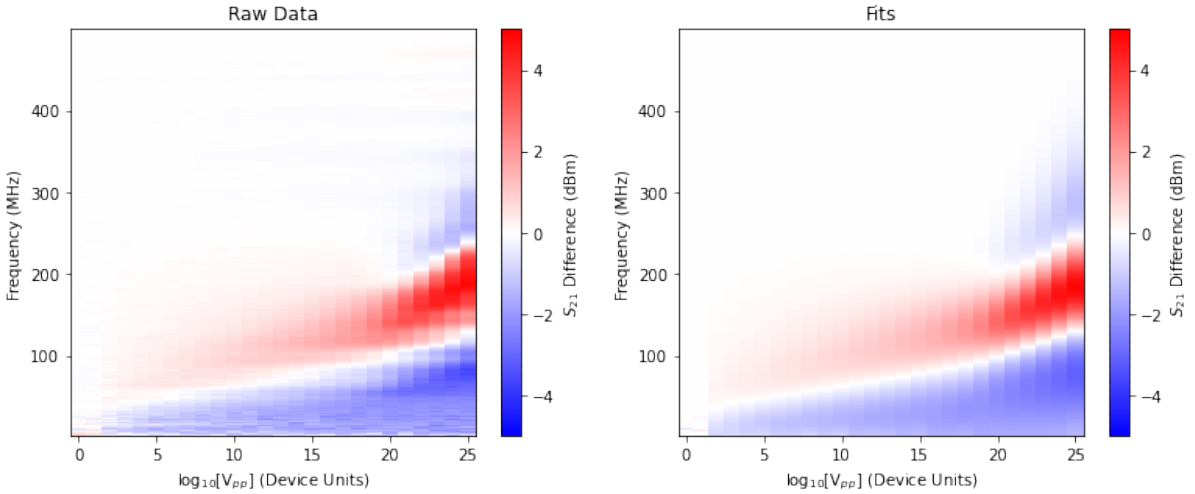

Figure 3.7: Data fit with positive and negative Gaussian curves. Data taken with double-tipped transmission PIP in DODECA plasma chamber, 6 Pa (45 mTorr), electrode V_{RMS} scan from approximately 10 to 40 V. Example fit parameters shown in Table 3.2.

Curve	Parameter	Value	Related Plasma Params.
+	Center Freq.	180.74 ± 0.41 MHz	n_e
	Width	43.13 ± 0.69 MHz	T_e and ∇n_e
	Scaling	24.03 ± 0.74	unclear
-	Center Freq.	151.49 ± 2.10 MHz	n_e
	Width	92.27 ± 2.29 MHz	T_e and ∇n_e
	Scaling	-12.52 ± 0.75	unclear

Table 3.2: Data fitting with two gaussian curves, one positive and one negative. DODECA plasma chamber, probe separation $\sim$ 2 mm, neutral pressure 6 Pa (45 mTorr), electrode V_{RMS}

3.4.2 Fit Uncertainties

The uncertainties listed in Table 3.2 are calculated via 6-dimensional χ^2 analysis that makes no assumption as to the distribution of the errors. Assuming that all errors are normal under-represents the error of this fit. This is demonstrated in Figure 3.9 using

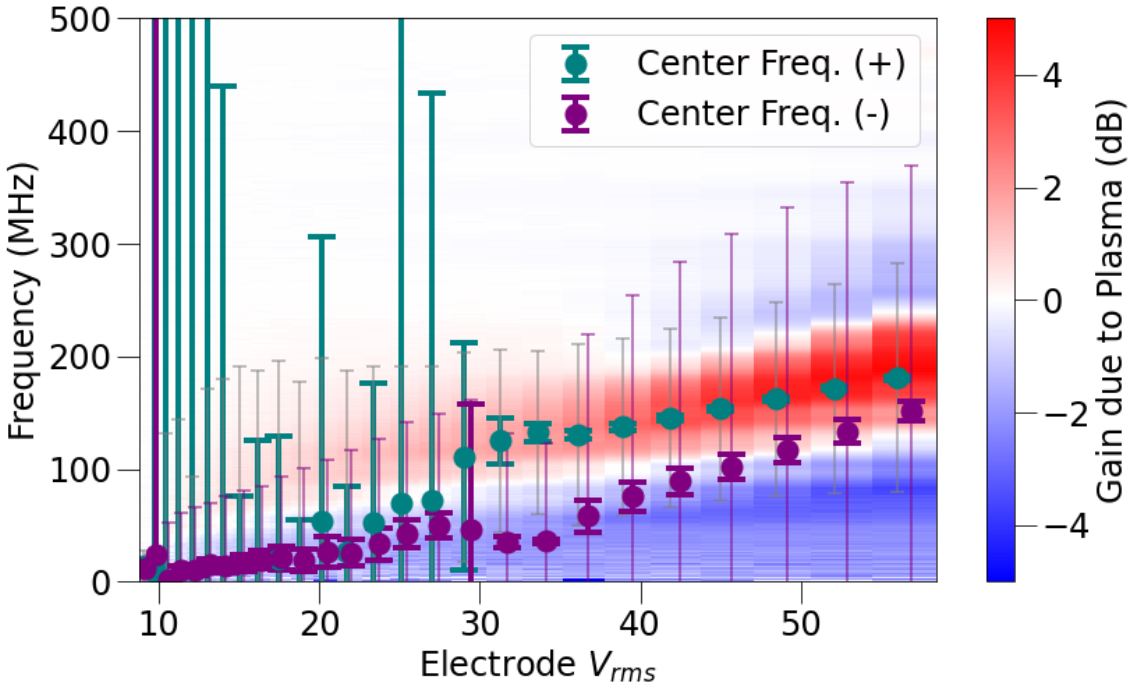

Figure 3.8: Center frequencies of Gaussian curves used to fit the data are shown. The *large* bars show the usual 2σ uncertainty limits for the center frequency values of the Gaussian curves used to fit the data. The *small* bars show the full width half maximum (FWHM) widths of these curves. The error for these widths was calculated (for example, in Table 3.2), but are not shown here. The values for the positive (teal) and negative (purple) Gaussian curves are slightly shifted from each other in their x-axis position for readability; the V_{rms} value associated with each data point is the *center* of the (vertical) spectrum as plotted here.

the 2-D error plane for positive Gaussian curve's center frequency and width parameters. The left side of Figure 3.9 shows two naive ways of performing χ^2 analysis. The gray ellipses show the intervals for 1σ, 2σ, and 3σ confidence taken from varying two fit parameters and calculating the corresponding χ^2 (color plot). The blue ellipses show the 2-D slices of the 6-D χ^2 confidence ellipsoids calculated by assuming that all errors are normal. These two methods produce almost identical confidence ellipses in this plane. But comparison to the graph to the right shows that this naive analysis is insufficient.

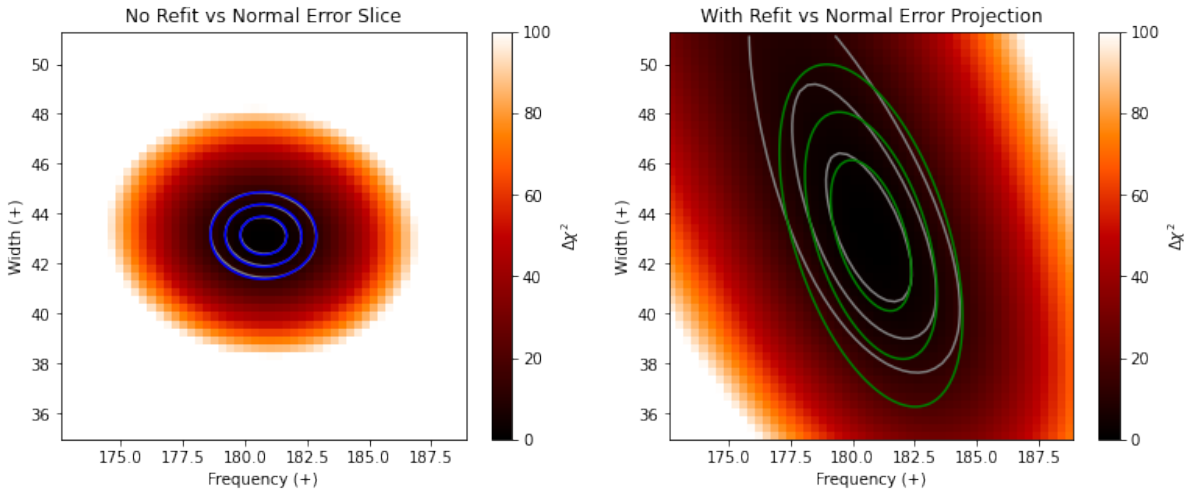

Figure 3.9: χ^2 analysis between the width (MHz) and center frequency (MHz) of the positive Gaussian fitting curve.
Left: ***Naive error analysis***. χ^2 is calculated for a span of δ values of two fit parameters near the fit solution, but all other parameters are *held constant*. The gray ellipses (hardly visible) show the $\Delta\chi^2$ boundaries for 1σ, 2σ, and 3σ confidence intervals. The blue ellipses are 2-D *slices* of the 6-D ellipsoids representing 1σ, 2σ, and 3σ confidence intervals assuming all errors are normal.
Right: ***More robust error analysis***. χ^2 is calculated for a span of δ values of two fit parameters near the fit solution, and all other parameters are *refit* to minimize χ^2. The gray ellipses show the $\Delta\chi^2$ boundaries for 1σ, 2σ, and 3σ confidence intervals. The green ellipses are 2-D *maxima projections* of the 6-D ellipsoids representing 1σ, 2σ, and 3σ confidence intervals assuming all errors are normal.

The right side of Figure 3.9 shows two more robust methods of performing χ^2 analysis. The gray ellipses show the intervals for 1σ, 2σ, and 3σ confidence taken from varying two fit parameters, *refitting the other parameters to minimize* χ^2, and then recording that minimum χ^2 value (color plot). The green ellipses show 2-D *projections* of the maxima of the 6-D confidence ellipsoids calculated by assuming normal errors. We see

that these two methods produce similar results, but the normal error assumption still under-represents the uncertainty in this 2-D fit parameter plane.

Let us not forget that these confidence ellipses are 6-dimensional surfaces in parameter space relating to the maximum $\Delta\chi^2$ for each level of confidence. To help us visualize this somewhat, Figure 3.10 shows a third dimension of the ellipses shown in the plot on the right in Figure 3.9.

We have thus far shown that we must *at least* perform the χ^2 analysis for each fit parameter by refitting all other parameters for a range of values near the fit solution. However, this is only sufficient if, referring to the full 6-D χ^2 map near the fit solution, the 6-D confidence interval surfaces are all *convex*. That is to say that, for any χ^2 plane (such as the example in Figure 3.9), if any of the confidence interval lines look like bananas instead of ellipses, our analysis might produce uncertainties that represent *local* minima of χ^2, not *total* minima, and we might therefore under-represent the related uncertainties.

To this end, a fully 6-dimensional χ^2 map was created in a region of parameter space centered about the fitting solutions. This χ^2 map was produced at low resolution due to the computational intensity of this task. The results of this work are plotted in Figure 3.11. The blue dots represent locations in this 2-D χ^2 plane where all values in the full 6-D χ^2 space are within the 2σ confidence error limit. Also plotted is the similar analysis performed by re-fitting values. We see that these two methods are in good agreement.

We may now fit the data using a combination of two Gaussian curves, and we may confidently describe the error of this fit. But the goal of this work is not to draw pictures that look like the data, the goal is to take the data and extract real plasma parameters such as n_e and T_e. We can say that the center frequency fit parameters seem like they *might* correspond to ω_{pe} for plasma between the two probe tips or between each probe tip and the chamber wall. And we can say that the Gaussian width ought

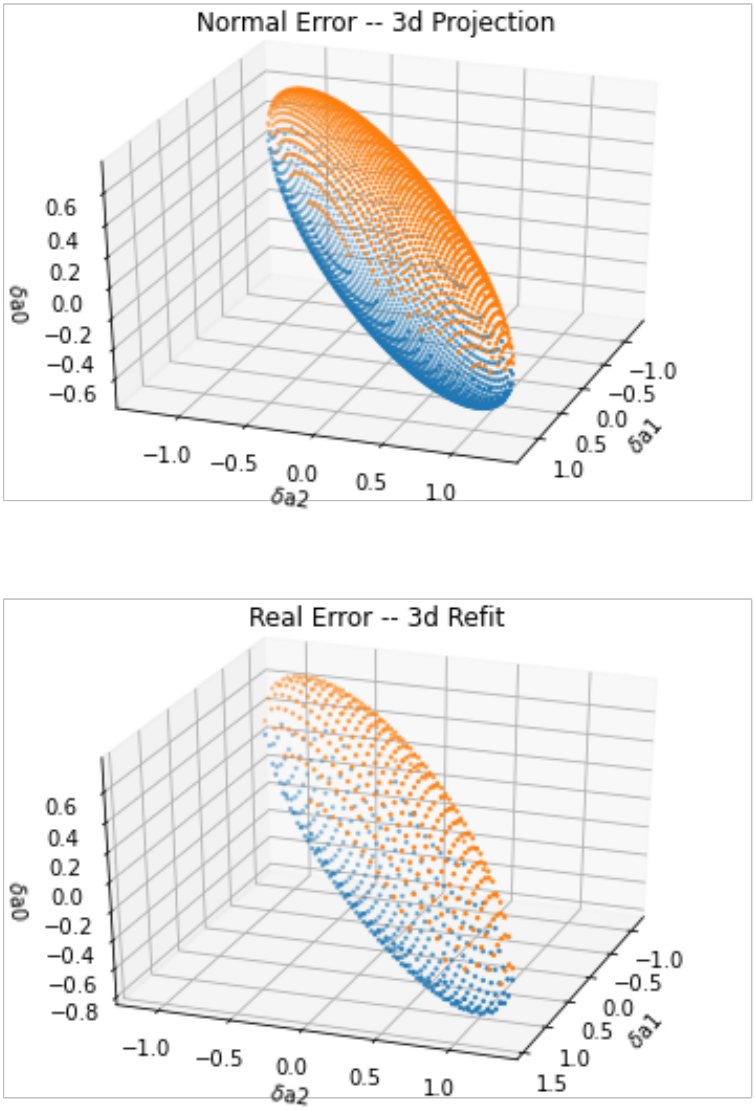

Figure 3.10: The error ellipsoids in Figure 3.9 represent 6-dimensional surfaces. They are here expanded to 3-dimensions to help visualize the true object. The axis labels, δa_0, δa_1, and δa_2 refer to small variations in the positive Gaussian fit's center frequency, width, and scaling parameter, respectively. The top ellipsoid is the 3-D projection of the green ellipses on the right side of Figure 3.9. The bottom ellipsoid is the 3-D projection of the gray ellipses.

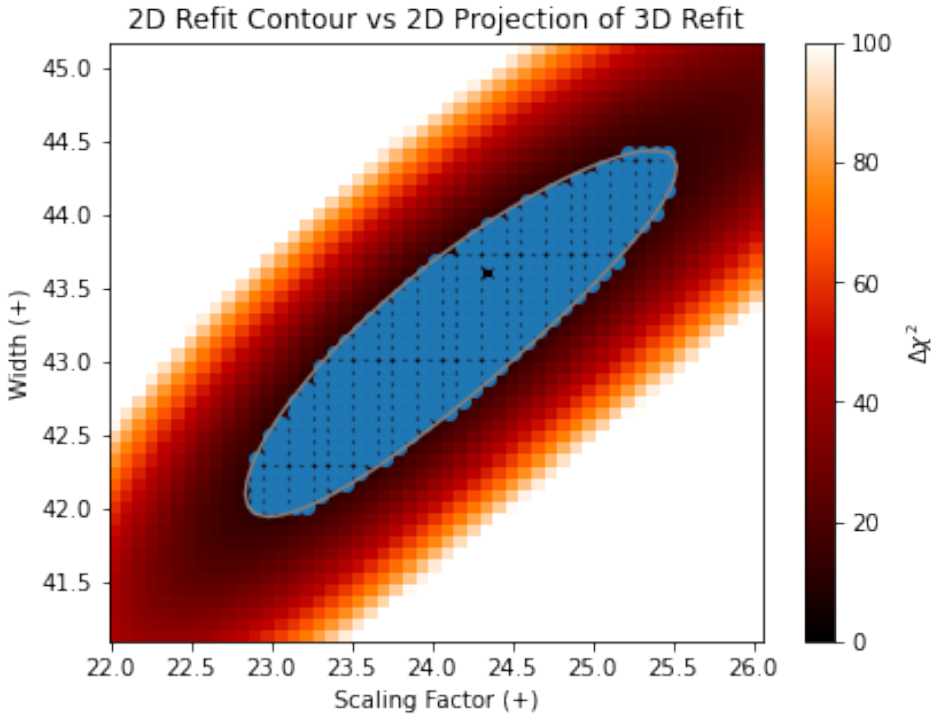

Figure 3.11: 2D χ^2 map relating the positive Gaussian curve's width (MHz) to that curve's scaling factor (unitless). This χ^2 map was created by refitting the other four parameters, as described in Figure 3.9, and the gray ellipsoid shows the boundary for the 2σ confidence region. The blue dots show the 2σ confidence region as determined via the full, proper 6-D χ^2 analysis. We see good agreement between these two error analysis techniques, but the full 6-D analysis is much more computationally intensive. This means that we may safely rely on the computationally lighter method.

to correspond to a combination of T_e and the gradient in density, ∇n_e. But this does not satisfactorily complete the goals of this thesis.

The fitting method described above starts with the shape of the data, fits it with a curve, and then attempts to interpret the curve parameters in terms of plasma physics. But this interpretation is somewhat hazy. Because of this, we decided to develop a means of interpretation whose logic flows the opposite direction: starting with the plasma physics, and then producing the model's best guess as to what the data ought to look like. To this end, we created a circuit simulation of the probe-plasma-chamber system.

Chapter 4

Circuit Simulations

The circuit model is analyzed using vna.py, a Python package I developed to perform lumped-element circuit simulations of one or more impedance probes immersed in plasma. Vna.py determines the values of the circuit elements based on the plasma model described in Chapter 2. It then performs circuit simulations using PySpice and ngspice. Vna.py can be thought of as a task-specific wrapper for PySpice. PySpice is, in turn, a Python wrapper for ngspice. At the center of this code onion, the methods included in ngspice perform the circuit simulations. This is depicted by the flowchart in Figure 4.1.

Ngspice is an open-source, mixed mode, mixed level circuit simulator, which implements the functionality of the proprietary Spice circuit simulation software. PySpice is an open-source Python package that aides in generating circuit model files, called "netlists." PySpice then uses ngspice to analyze these netlists and returns the output in a numpy format, which is ubiquitous in Python-based data analysis.

The code onion can always be peeled further – ngspice is based on the Spice3f5, Cider1b1, and Xspice packages. But for our purposes, it is sufficient to say that vna.py runs circuit simulations using PySpice and ngspice.

There are two intended uses for vna.py: simulating a transmission spectrum for known plasma parameters, and determining experiment plasma parameters by fitting

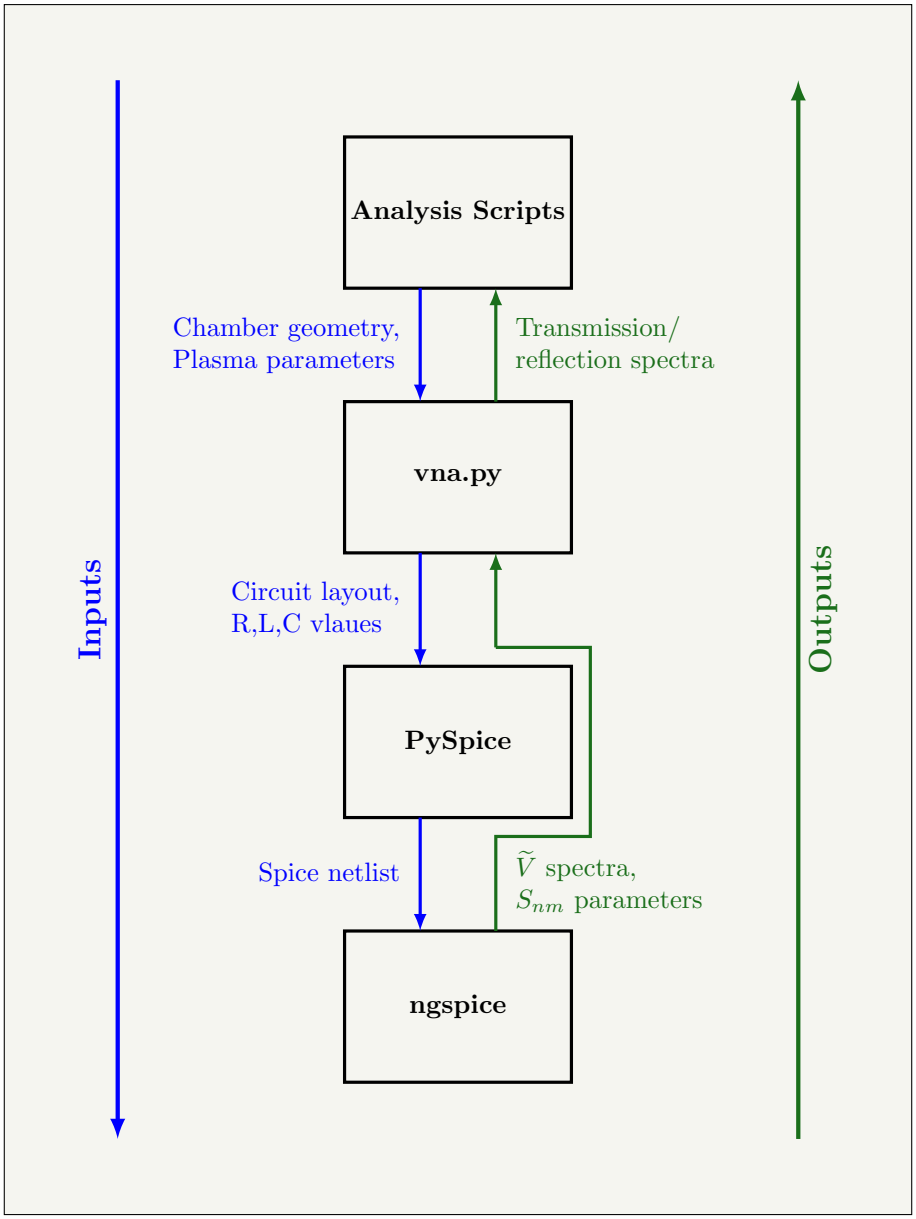

Figure 4.1: vna.py plasma circuit modeling flowchart

data from a Vector Network Analyzer (VNA). The latter is achieved by repeatedly performing the former, so we shall begin by describing the simulation of a transmission spectrum.

4.1 The Simulation Object

The centerpiece of the vna.py library is the `simulation` class. A vna.py `simulation` is given chamber geometry information, probe goemetry information,

and plasma parameters. Before the `simulation` can create a PySpice circuit object, the following quantities must be calculated:

1. Sheath thicknesses
2. Capacitances
3. Bulk plasma inductance and resistance

4.1.1 Calculating Sheath Thickness

The sheath thickness is found by numerically solving Poisson's Equation in the sheath,

$$\nabla^2\phi(r) = \frac{e}{\epsilon_0}(n_e - n_i), \tag{4.1}$$

or, written for cylindrical geometry with no $\hat{z}$ or $\hat{\theta}$ dependence,

$$\phi'' = \frac{e}{\epsilon_0}\left(n_e - n_i\right) - \frac{\phi'}{r}. \tag{4.2}$$

To solve this, we must assume or determine expressions for the electron and ion densities in the sheath, $n_e(r)$ and $n_i(r)$. At the sheath edge, $r = s$, we assume that electrons and ions are quasi-neutral,

$$n_i(s) \approx n_e(s) \approx n_s, \tag{4.3}$$

and we assume the electrons are Boltzmann-distributed,

$$n_e(r) = n_s e^{e\phi(r)/k_B T_e}. \tag{4.4}$$

We assume that the ions enter the plasma sheath from the bulk plasma at the Bohm velocity,

$$u_i(s) = u_B = \left(\frac{k_B T_e}{m_i}\right)^{1/2}, \tag{4.5}$$

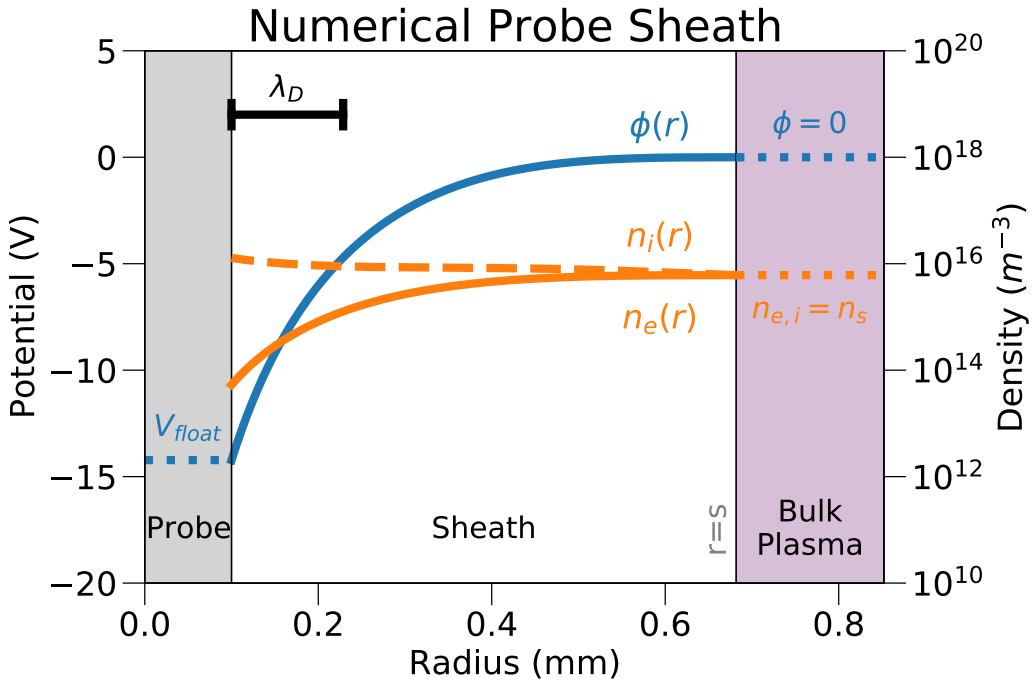

(a) Poisson's Equation is solved numerically in the sheath around an electrically-floating cylindrical probe immersed in the plasma for a given sheath thickness. From this solution, we find the potential difference across the sheath as a function of the given sheath thickness. The increaed ion density towards the probe is due to the cylindrical geometry.

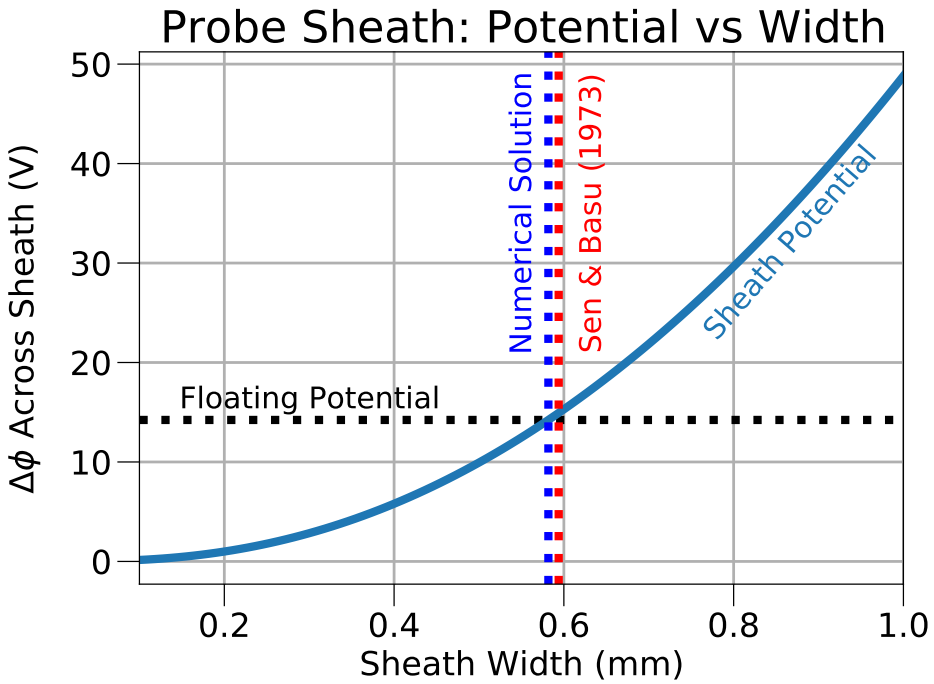

(b) We choose the sheath thickness which yields a potential difference matching the expected probe floating potential from Langmuir probe theory (Eqn 4.11). The blue dashed line shows the sheath-width using this method. The red dashed line uses the approximate solution from [4], and is plotted for comparison.

Figure 4.2: Determining Sheath Thickness

and assume collisionless, cold ions, such that each ion carries kinetic energy,

$$\frac{1}{2}m_i u_i^2(r) = \frac{1}{2}m_i u_B^2 - e\phi(r). \tag{4.6}$$

We also assume that ions are continuous in the sheath (no ionization or recombination),

$$2\pi r n_i(r) u_i(r) = 2\pi s n_s u_B. \tag{4.7}$$

Combining Equations 4.6 and 4.7, we may determine an expression for ion density in the sheath,

$$n_i(r) = n_s \frac{s}{r}\left(1 - \frac{2e}{m_i u_B^2}\phi(r)\right)^{-1/2} \tag{4.8}$$

Finally, we use Equations 4.4 and 4.8 to rewrite Poisson's Equation (Eqn 4.2) with all dependence on r made explicit:

$$\phi'' = \frac{n_s e}{\epsilon_0}\left(e^{\phi(r)/T_e} - \frac{s}{r}\left(1 - \frac{2e}{m_i u_B^2}\phi(r)\right)^{-1/2}\right) - \frac{\phi'}{r} \tag{4.9}$$

To solve Equation 4.9, we use the following boundary conditions:

$$\phi_{sheath} = 0 \tag{4.10a}$$

$$\phi'_{sheath} = 0 \tag{4.10b}$$

$$\phi_{surface} = V_{float}\ or\ V_{plasma}\ or\ V_{bias} \tag{4.10c}$$

where the potential in Equation 4.10c is chosen depending on the potential of the surface in question.

Equation 4.9 is solved numerically using the boundary conditions in Equation 4.10. The result is shown in Figure 4.2a. As shown in Figure 4.2b, the sheath thickness is found by calculating the potential difference across the sheath, and adjusting the

sheath thickness until this matches the expected surface potential. In this case, $\phi_{surface}$ is the floating potential from Langmuir probe theory,

$$\Delta V = \frac{k_B T_e}{2e} ln\left(\frac{m_i}{2\pi m_e}\right). \tag{4.11}$$

There are practical considerations to solving Equation 4.9 that we will not discuss in detail here. For example, there sometimes exist mathematically valid solutions to Poisson's equation that are non-physical, and the order in which the boundary conditions are applied (Equation 4.10) can sometimes be important. For a detailed discussion of these practical matters, see the Jupyter notebook included in Appendix A.

4.1.2 Calculating Capacitances

The `simulation` object then determines the capacitances between the probe tips and the probe sheath edge (C_{ps}), between the wall and the wall sheath edge (C_{ws}), between the two probe sheathes (C_{pp}), and between the probe sheath and the wall sheath (C_{pw}). `simulation` has two different methods which may be used to calculate these capacitances: using exact solutions for drastically simplified approximations of the relevant geometry or by numerically solving Poisson's Equation in a more robustly modeled chamber.

The default option for calculating these capacitances is to use exact solutions for drastically simplified approximations of the geometry. C_{ps} is modeled as the capacitance between two concentric cylinders, ignoring edge effects:

$$C_{ps} = 2\pi\epsilon_0 \frac{l}{ln(\frac{s_p}{r_p})}, \tag{4.12}$$

where l is probe length, r_p is the probe radius, and s_p is the probe sheath radius.

When simulating the DODECA chamber, C_{ws} is modeled as the capacitance between two concentric spheres:

$$C_{ws} = 4\pi\epsilon_0 \frac{r_w s_w}{r_w - s_w}, \tag{4.13}$$

where r_w is the wall radius and s_w is the wall sheath radius.

C_{pp} is modeled as the capacitance between two cylinders, ignoring edge effects:

$$C_{pp} = 2\pi\epsilon_0 \frac{l}{cosh^{-1}\left(\frac{d^2 - 2s_p^2}{2s_p^2}\right)}, \tag{4.14}$$

where d is the distance between the probe tips.

C_{pw} is the least realistic model; it's modeled as the capacitance between two concentric cylinders, which does not match the true shape of the chamber:

$$C_{pw} = 2\pi\epsilon_0 \frac{l}{ln(\frac{s_w}{s_p})}. \tag{4.15}$$

These calculations are computationally quick, and are sufficient for most situations. However, when greater accuracy is desired, the `simulation` object may instead calculate the mutual capacitance between these surfaces, or any other desired surfaces, by creating a 3d grid of the plasma chamber, probes, and other objects, and then numerically solving Poisson's Equation in this volume.

The capacitance between any two conducting objects modeled may be calculated by applying a series of voltage differences between the two objects, calculating the resulting charge on each object, and fitting the results to the definition of capacitance, $Q = CV$.

For each simulated voltage difference, Φ is found by solving Poisson's Equation across the entire chamber volume using the Gauss-Seidel method [24]. For example, Figure 4.3 shows Φ for one of many ΔVs which must be solved in the process of determining

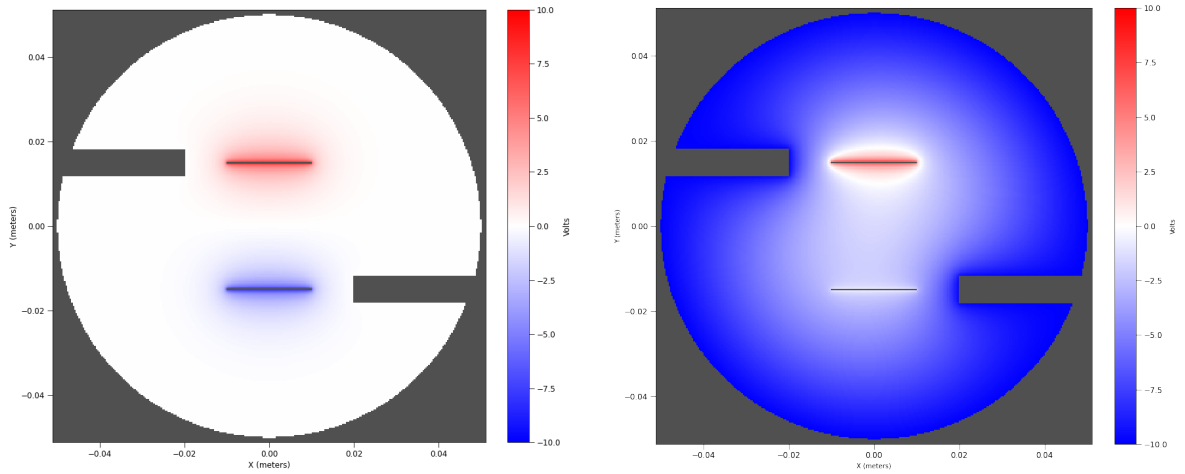

(a) Finding $C_{probe-probe}$

(b) Finding $C_{probe-ground}$

Figure 4.3: 2D Slice of Voltage in a Plasma Chamber. Poisson's Equation is solved for a series of arbitrary ΔVs between two objects whose mutual capacitance we wish to find. In both examples above, we are finding capacitance in vacuum (no plasma).

the mutual capacitance between two probe tips in a spherical plasma chamber. In this example, ΔV between the probe tips is set to 20 V, and the probe shafts and the chamber walls are assumed to be grounded. The non-conductive probe tip sleeves are not simulated here.

The surface charge density on each of the two objects in question may now be found using $\sigma = D \cdot \hat{N}$, where D is the electric displacement, $D = -\epsilon_0 \nabla \Phi$. The `simulation` then integrates σ to find Q, and ΔV vs ΔQ is fit to a linear function, where mutual capacitance, C, is the slope.

This process is computationally intensive, but may offer more accurate results than the analytical solutions of the approximated geometries presented above. In the future, the computation time may be significantly reduced by using adaptive grid spacings, but this has not been implemented.

4.1.3 Calculating Bulk Plasma Values

Recall that the goal of these calculations is to simulate a circuit such as those shown in Figure 2.3. The `simulation` has now calculated sheath thicknesses, and it has calculated the mutual capacitance between all relevant electrodes, chamber walls, and plasma sheath surfaces. What remains is to find bulk plasma resistance and inductance using Equations 2.1, reproduced here:

$$L_p \approx \omega_{pe}^{-2} C_p^{-1}, \tag{2.1a}$$

and

$$R_p \approx \nu L_p. \tag{2.1b}$$

The value for ω_{pe}, Equation 2.18, is readily calculated from values already known to the `simulation`, but finding the momentum transfer frequency, ν, requires values for electron-neutral momentum transfer cross sections, σ_{en}:

$$\nu = \frac{V_{th,e}}{\lambda_{mfp}} = \left(\frac{8 k_B T_e}{\pi m_e}\right)^{1/2} (n_n \sigma_{en}), \tag{4.17}$$

where $V_{th,e}$ is the electron thermal velocity, λ_{mfp} is the electron mean free path traveled between collisions, m_e is the electron mass, and n_n is the neutral density. All values are readily available to the `simulation` except for σ_{en}. For this, we extrapolate from data contained in Table I of Pack et. al. [41], which contains empirical values for σ_{en} as a function of T_e for plasmas of various noble gases. Armed with these values, the `simulation` now has all information required to analyze the circuit using PySpice.

4.1.4 Basic Circuit Simulation Results

The circuit model for a single-tipped probe (Figure 2.3a) yields results (Figures 4.4a and 4.4b) which match literature [8]. The transmitted power is suppressed at f_{pe}, where the natural oscillation of the electrons allows the plasma to absorb more power.

It also has a transmission peak at a lower frequency, which is due to a series resonance between the sheath capacitances and the bulk plasma impedance. These resonances correspond with a phase shift of 0 degrees.

A similar result is obtained for the double-tipped probe (Figures 4.4c and 4.4d), with additional resonance behavior due to the more complicated circuit model (Figure 2.3b). The transmission spectrum still has the expected suppression at the plasma frequency due to absorbed power, but the transmission peak is now split into two peaks, due to additional circuit resonances in the plasma model. The higher-frequency transmission peak corresponds with a phase difference of 0 degrees, similar to the transmission maximum of the single-tipped probe. The lower-frequency double-probe transmission peak corresponds to a phase difference of 180 degrees.

4.1.5 Qualitative Comparison to Experiment

In Figure 4.5, we show experimental transmission spectra taken in the DODECA plasma chamber, and compare them to simulated spectra. At the top left, we show transmission spectra as gas pressure was increased from 10 to 20 Pa (45 to 90 mTorr). The data features did not shift in frequency, but did shift in amplitude. This is compared to the top right, where the simulation gas pressure parameter was swept in the same range. The two plots show qualitative agreement in that the same basic behaviour is displayed in the experiment as in the simulation. We note that the peak in transmission gain due to plasma (the horizontal red "stripe") decreases by about 4 dB in the experiment, and decreases by about 5 dB in the simulation.

On the bottom row of this figure, we see that sweeping the electrode voltage shifts the transmission data features strongly in the frequency domain. We compare an experimental sweep of the electrode V_{RMS}^2, which goes roughly but not precisely with the power absorbed by the plasma, with a simulated sweep of the plasma density. Again, we mostly see qualitative agreement between the experiment and simulation.

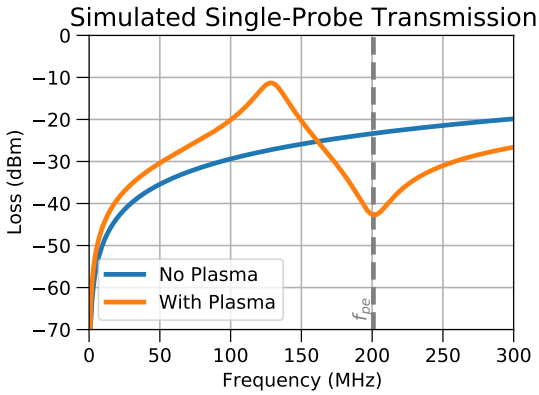

(a) Simulated transmission loss from a single probe tip to the chamber wall is shown for the probe in an empty plasma chamber (blue) and in the same chamber with the plasma turned on (orange). The plasma frequency is approximately 200 MHz (dashed gray).

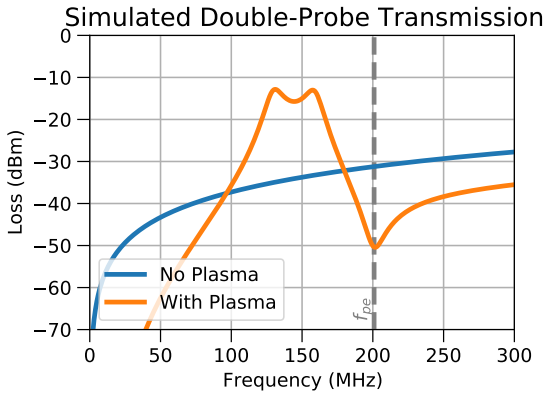

(b) Simulated transmission loss between probe tips for a double-tipped transmission probe is shown for the probe in an empty plasma chamber (blue) and in the same chamber with the plasma turned on (orange). The plasma frequency is approximately 200 MHz (dashed gray).

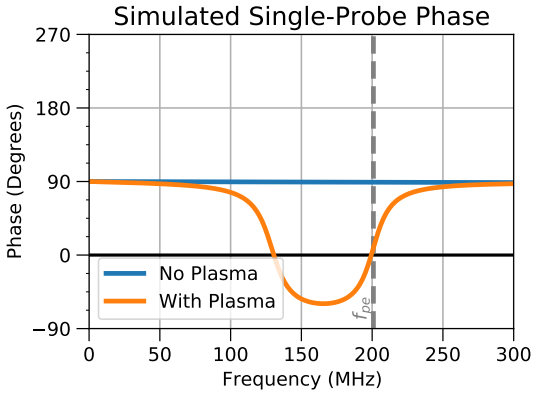

(c) Simulated transmission phase difference between chamber wall and probe tip is shown for the probe in an empty plasma chamber (blue) and in the same chamber with the plasma turned on (orange). The plasma frequency is approximately 200 MHz (dashed gray).

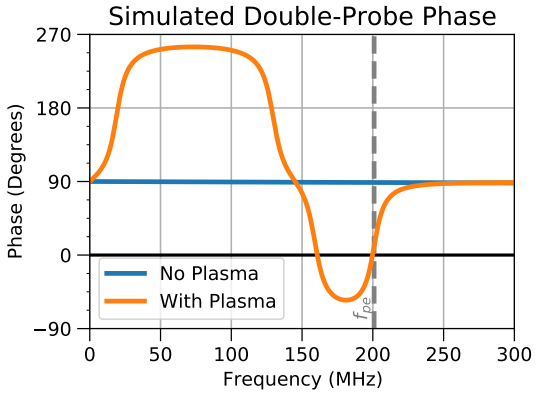

(d) Simulated transmission phase difference for a double-tipped transmission probe is shown for the probe in an empty plasma chamber (blue) and in the same chamber with the plasma turned on (orange). The plasma frequency is approximately 200 MHz (dashed gray).

Figure 4.4: Simulated transmission loss (top row) and phase (bottom row) for a single-tipped probe (left column) and a double-tipped probe (right column)

We do see one issue with the simulation that needs to be addressed: the simulated plasma does not become optically clear at frequencies well above the plasma frequency, but it is well known that plasma should not strongly interact with high-frequency electromagnetic signals. We shall now address this problem.

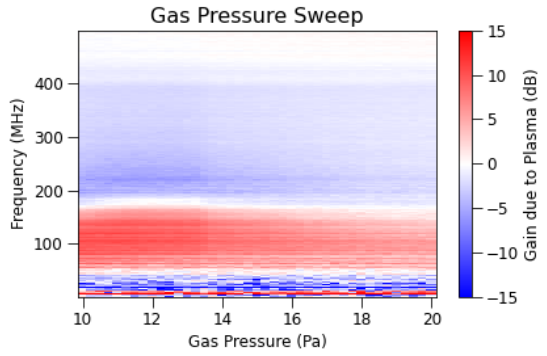

(a) Experiment gas pressure sweep: Krypton gas, $V_{RMS} \approx 56\,V$, probe separation $\approx$ 3 cm

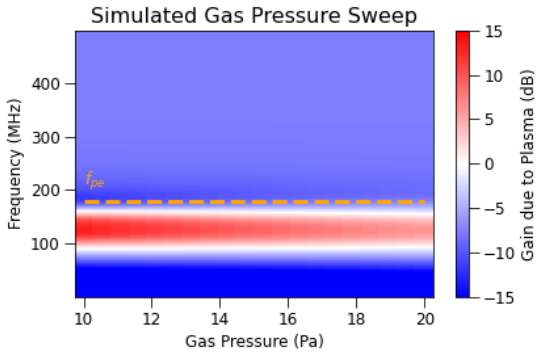

(b) Simulated gas pressure sweep: Krypton gas, $n_e = 4 \times 10^{14} m^{-3}$, probe separation = 3 cm

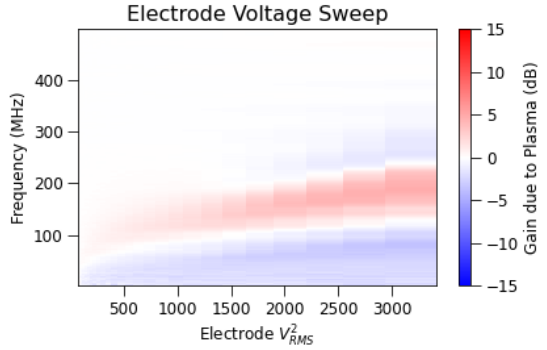

(c) Experiment electrode voltage sweep: Argon gas, $P_{gas} \approx 6\,Pa$, probe separation $\approx$ 0.3 cm

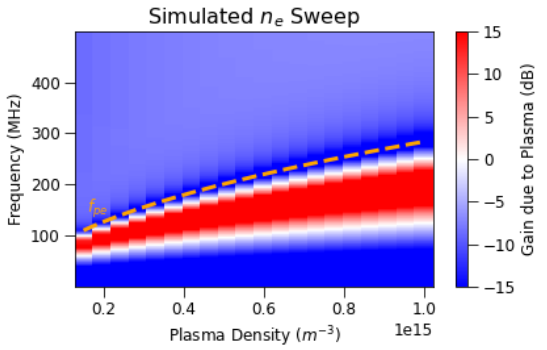

(d) Simulated n_e sweep: Argon gas, $P_{gas} = 6\,Pa$, probe separation = 3 cm

Figure 4.5: Comparison of simulated and experimental gas pressure and electron density sweeps.

4.2 High Frequency Limit

In the high-frequency limit of electric signals passing through plasma ($\omega >> \omega_{pe}$), the plasma is optically clear, and the signal passes through unimpeded. Thus, at high frequency, the transmitted power through the plasma should match the transmitted power in the vacuum case. However, the circuit model does not correctly model this

behavior. This mismatch is shown clearly for a single transmission spectrum in Figure 4.6. We need to solve this issue.

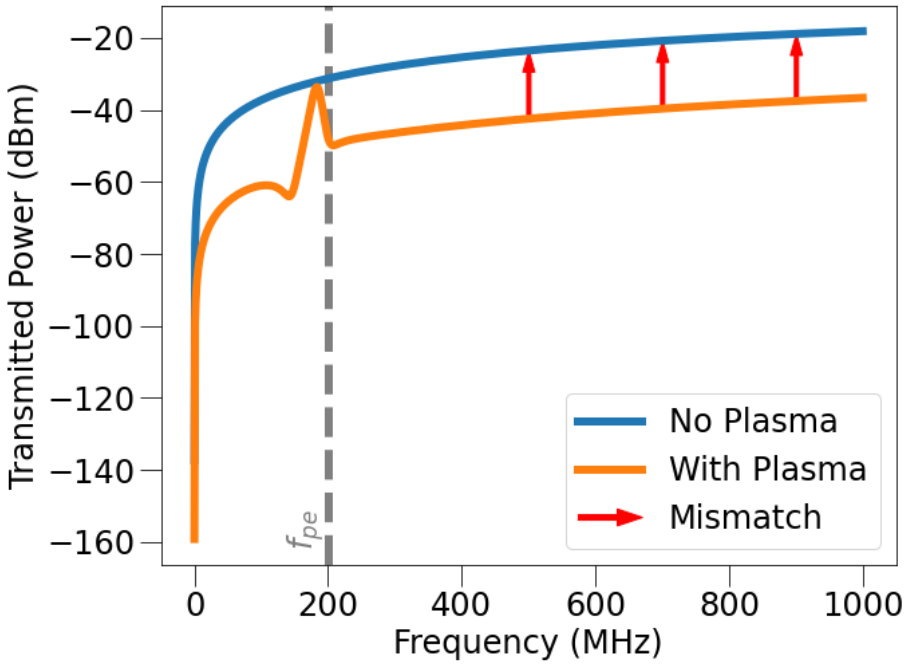

Figure 4.6: Simulated transmission power with and without plasma in the chamber fail to match at $f \gg 2\pi\omega_{pe}$

4.2.1 Reproducing the Mismatch in a Simplified Circuit

To investigate this further, we briefly consider a fictitious measurement of power transmitted from a single probe tip to the chamber ground (Figure **??**). By "fictitious," we mean that this is not a measurement that would be possible in any of the plasma chambers used in this work because those plasma chambers are directly mounted to the grounded optical bench.

For the probe and chamber geometries that match our experiments, a cylindrical probe in a spherical chamber, we see this same high frequency mismatch between simulation with and without plasma (Figure 4.7a). However, for the case of a spherical probe tip in a spherical plasma chamber, the high frequency behavior *does* successfully describe an optically clear plasma (Figure 4.7b). There are two reasons that the model fails in this limit for high-frequency behavior. Firstly, the model's approximations for the

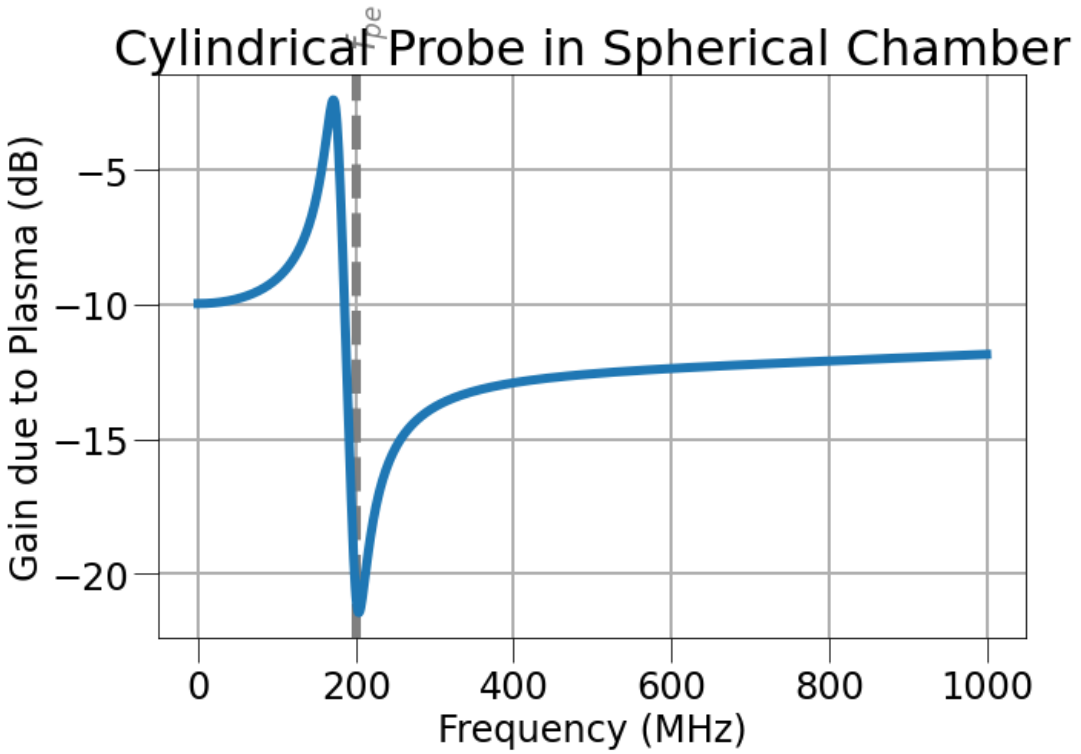

(a) Simulated transmission gain due to plasma for a single cylindrical probe tip in a spherical plasma chamber. The high-frequency limit fails to correctly approach 0 dB.

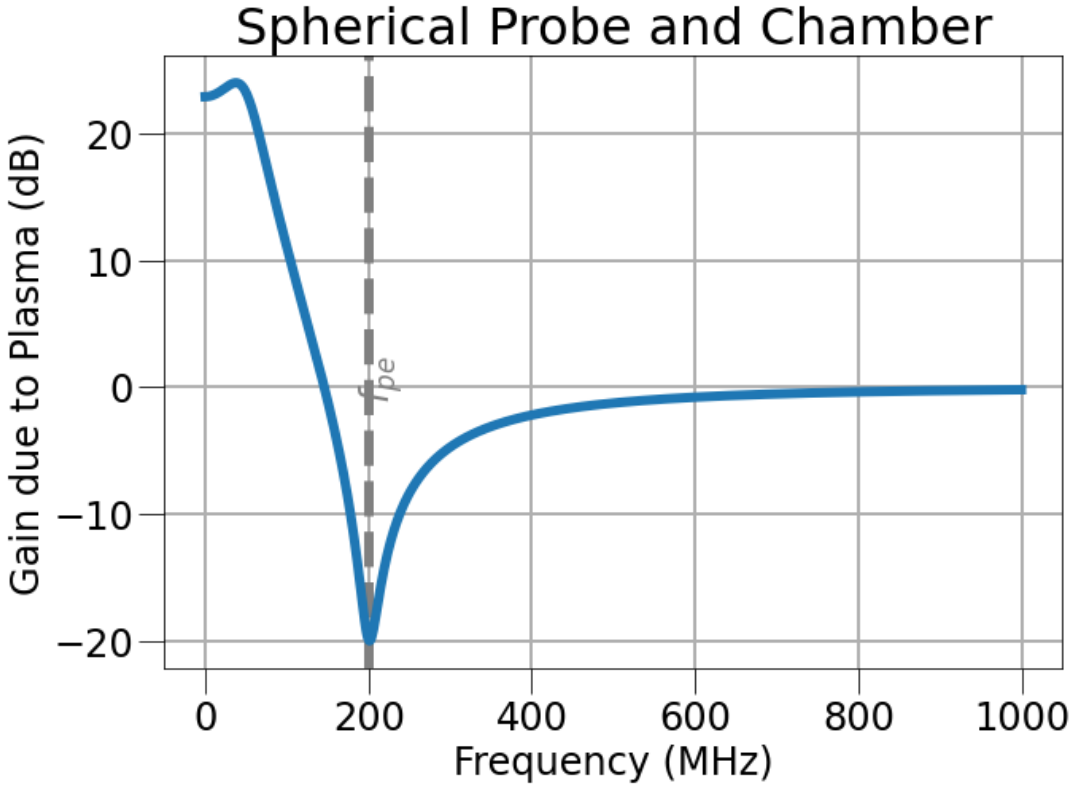

(b) Simulated transmission gain due to plasma for a single spherical probe tip in a spherical plasma chamber. The high-frequency limit correctly approaches 0 dB.

Figure 4.7: The high-frequency limit behaves appropriately for a spherical probe in a spherical chamber, but behaves inappropriately in the case of a cylindrical probe in a spherical chamber.

capacitance between a cylindrical object in the center of a hollow sphere may be insufficiently accurate. Secondly, The circuit model may fail in this extreme because, for the case of a cylindrical probe tip in a spherical chamber, the sheath boundaries in the plasma-on condition do not lie on equipotential lines for the plasma-off condition. Therefore the capacitance of the plasma-off condition is not identical to the total capacitance of the sheaths in series with the bulk capacitance in the plasma-on condition.

4.2.2 Fixing the High Frequency Limit

Recall that most of the work done by the circuit `simulation` is in finding relevant capacitances to describe the coupling between probes, sheath surfaces, and chamber walls. Once the capacitances are found, it is relatively straightforward to calculate the corresponding resistances and inductances. Moreover, the physically unrealistic part of the simulated spectra occur at very high frequency, and all parts of the circuit but the capacitances may be neglected in this frequency range. We thus modify the circuits in Figure 2.3 by neglecting the bulk plasma resistances and inductances, leaving only the parts shown in 4.8.

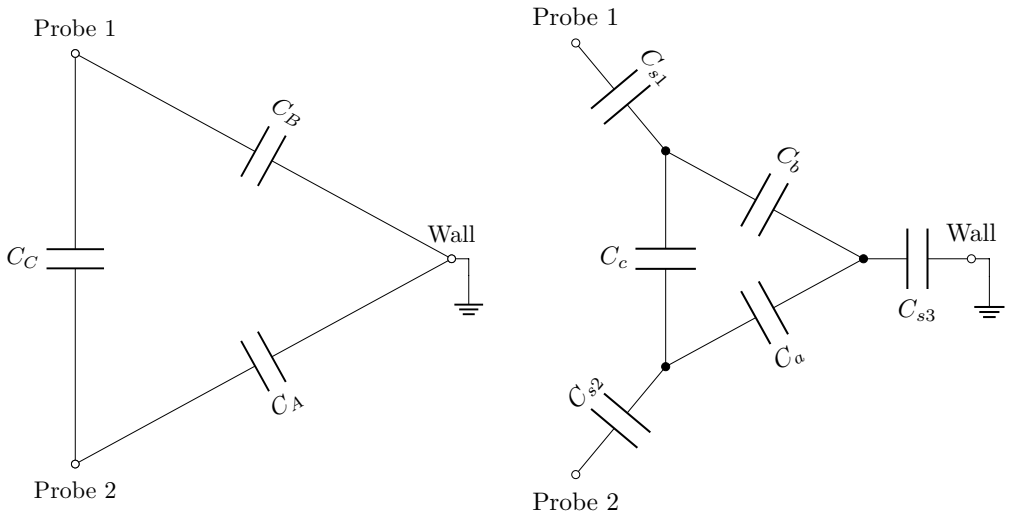

(a) Vacuum chamber circuit

(b) Plasma circuit for $\omega >> \omega_{pe}$

Figure 4.8: Circuit Models for High Frequency Limit. We expect the transmission spectra with and without plasma to converge at $\omega >> \omega_{pe}$.

At high frequency, the transmission spectra ought to be identical for the chamber with and without plasma. We can achieve this result by constraining the total capacitance between any two ports to be the same in the vacuum case and in the plasma-on (high frequency) case. Note what a frustratingly simple solution this is to a problem that persisted for nearly three years.

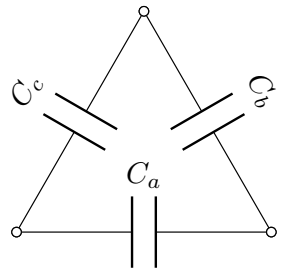

Δ shape

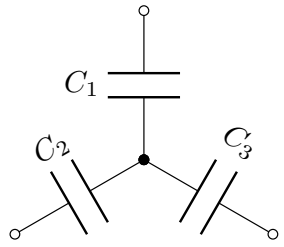

Y shape

Δ to Y	Y to Δ
$C_1 = \frac{C_aC_b+C_aC_c+C_bC_c}{C_a}$	$C_a = \frac{C_2C_3}{C_1+C_2+C_3}$
$C_2 = \frac{C_aC_b+C_aC_c+C_bC_c}{C_b}$	$C_b = \frac{C_1C_3}{C_1+C_2+C_3}$
$C_3 = \frac{C_aC_b+C_aC_c+C_bC_c}{C_c}$	$C_c = \frac{C_1C_2}{C_1+C_2+C_3}$

Figure 4.9: Δ-Y Transform. The Δ-shaped circuit and the Y-shaped circuits are equivalent. The table shows how to convert between the two.

Solving the circuits to force the high-frequency transmission with and without plasma to match may be achieved using the $\Delta - Y$ Transform identity (Figure 4.9) to convert the circuit in Figure 4.8b into an equivalent circuit with the same form as that shown in Figure 4.8a. Figure 4.10 depicts how this is done: first we transform the Δ-shaped arrangement of capacitors in the interior of Figure 4.8b into its equivalent Y-shaped arrangement of capacitors. The resulting equivalent circuit is entirely Y-shaped, and we may transform this *entire* resulting circuit into *its* equivalent Δ-shaped capacitor arrangement. Using the relations in Figure 4.9, we may now determine the values of each bulk plasma capacitance, that is $C_{a,b,c}$ in Figure 4.8b, such that the high-frequency S_{nm} parameters match the vacuum case, Figure 4.8a.

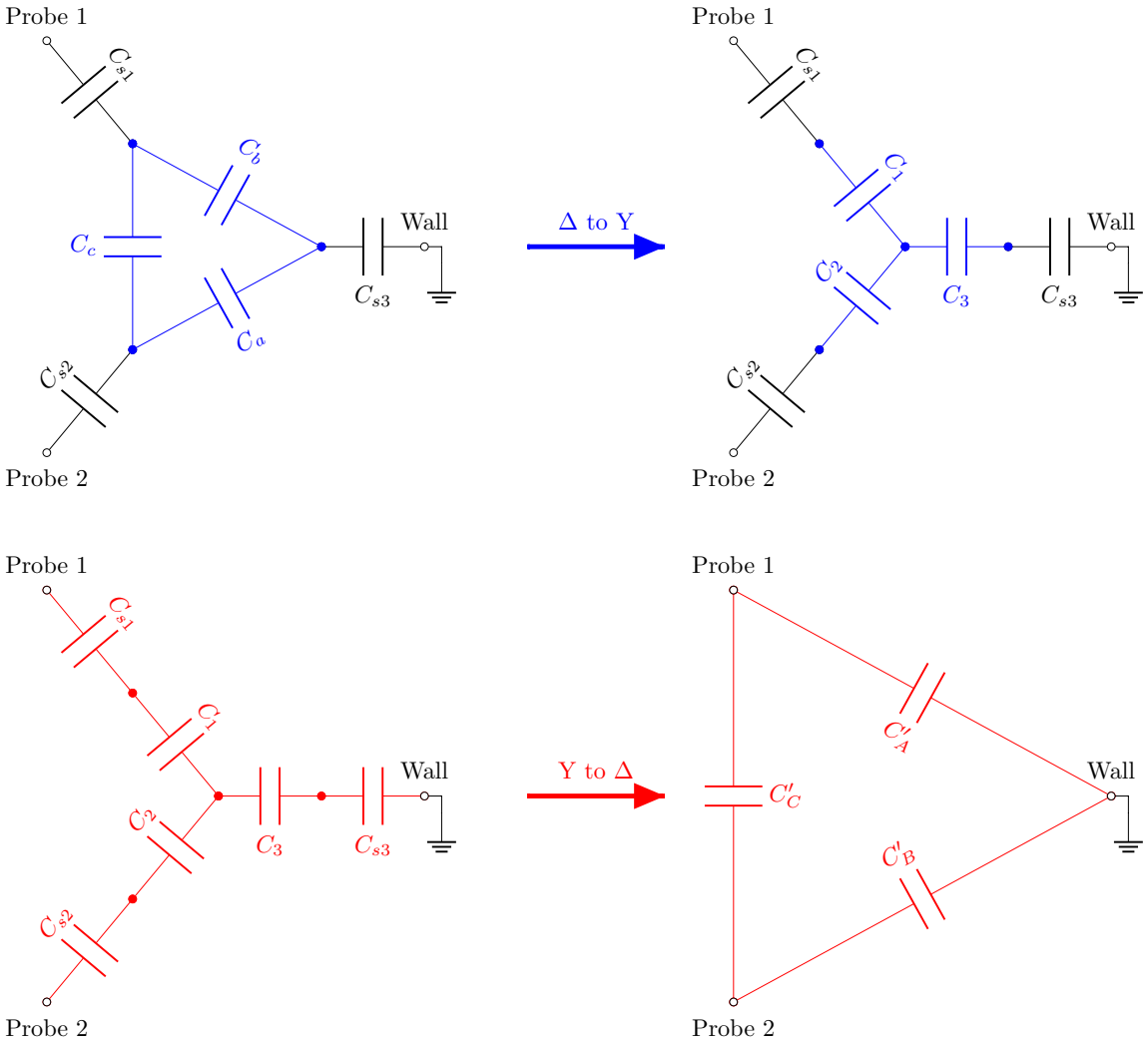

Figure 4.10: Using $\Delta - Y$ Transform to Find Plasma Capacitance: The top left shows the transmission impedance probe circuit with plasma on for $f >> 2\pi\omega_{pe}$. The interior Δ-shaped triangle of this circuit is transformed to a Y-shape (in blue). Then, the resulting circuit is transformed into a Δ-shape (in Red), which now may be directly compared to the plasma-off circuit.

Having forced the plasma capacitance to be equivalent to the vacuum chamber capacitance, the circuit simulation transmission spectra now correctly match each other at high frequency, as shown in Figure 4.11. We have solved the high-frequency issue, and gained the additional benefit of bypassing the computationally intensive capacitance calculations described in Section 4.1.2. We are now, finally, prepared to use the `simulation` object to analyze real data. However, first let us take a brief detour to discuss a claim made in Section 1.4.3, that transmission-type impedance probes are separately sensitive to plasma parameters near and far from the probe tips.

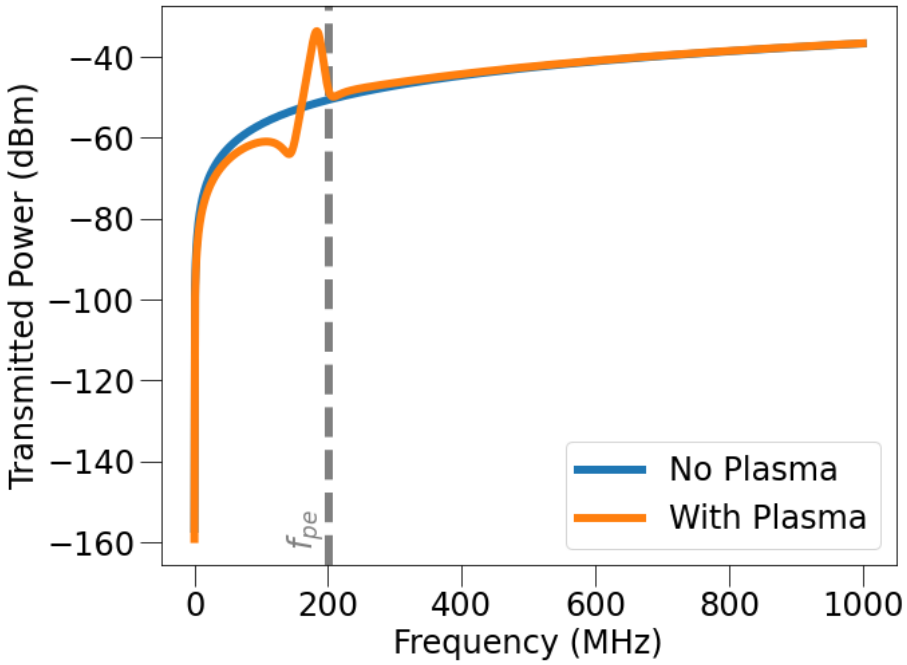

Figure 4.11: Simulated transmission power after forcing total capacitance with plasma to match vacuum case. High frequency transmission power now appropriately matches for plasma-on and plasma-off conditions

4.3 Density Near and Far

One of the benefits of the transmission-type impedance probe is that the measurement is separately sensitive to plasma parameters near and far from the probe tips. The RF signals passed through the plasma are transmitted as a near-field oscillation of a compressional wave mode. We expect these compressional signals mostly travel along the electric field lines connecting the various conducting surfaces in the plasma

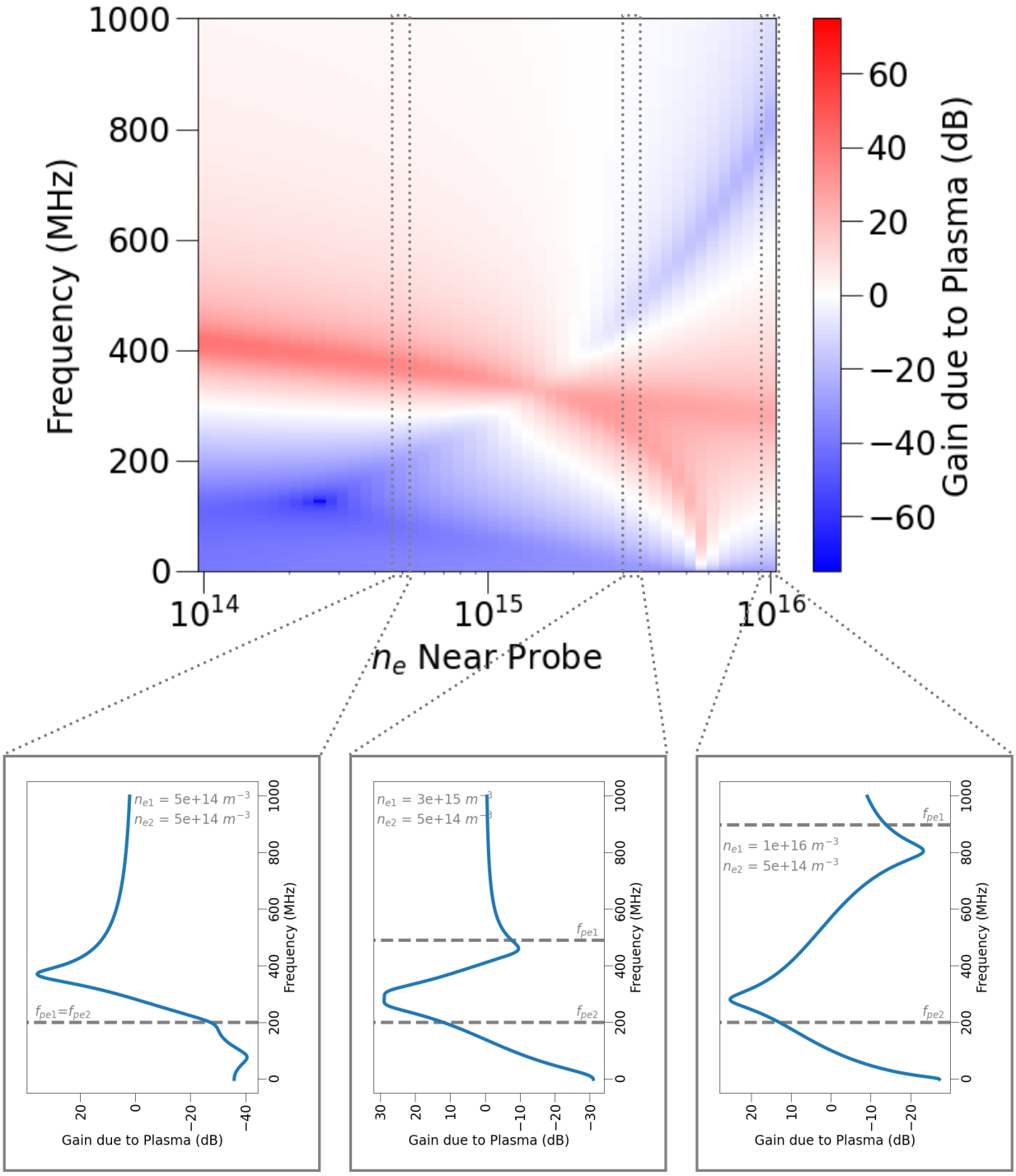

Figure 4.12: Transmission-type impedance probes are separately sensitive to n_e *near* the probe tips and farther away. The electron density near the probe tips is n_{e1}, and the density far away is n_{e2}. This simulation shows that changing n_e near the probe tips primarily shifts the frequency of the transmission *minimum*.

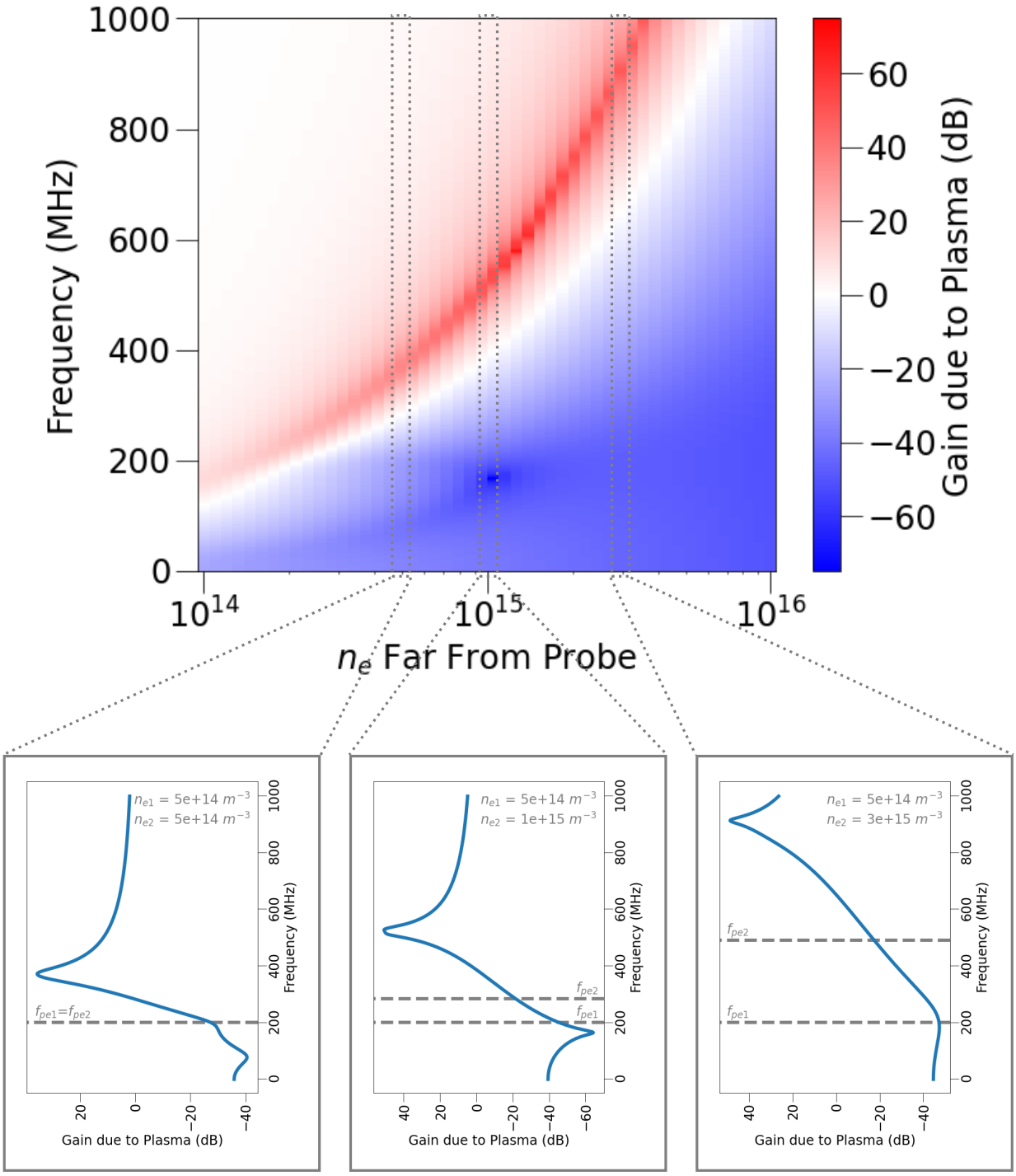

Figure 4.13: Transmission-type impedance probes are separately sensitive to n_e near the probe tips and farther away. The electron density near the probe tips is n_{e1}, and the density far away is n_{e2}. This simulation shows that changing n_e *far* from the probe tips primarily shifts the frequency of transmission *maximum*.

chamber, and the nature of these signals are governed by the plasma encountered *along* those field lines. Because of the shape of these electric field lines, the electrons *far* from the probes primarily influence the transmission of RF signal between the probe tips and the grounded chamber wall. Conversely, the electrons *near* the probe tips more strongly influence the transmission of signal from probe tip to probe tip. We then expect that the electrons near the probe tips and the electrons far away will have, in some sense, opposite effects on the probe tip to probe tip transmission spectra.

Recall that the basic response of plasma to RF signals can be thought of as a band-stop filter, where signals of frequency near ω_{pe} are met with high real and (positive) imaginary impedance. The primary effect of the nearby electrons ("between" the probes) will govern a local *minimum* in transmission power between the probe tips, which represents the stop band of the tank circuit between the probe tips. This effect is shown in Figure 4.12. On the other hand, electrons *far* from the probes ("between" probe and grounded chamber wall) will govern a local *maximum* in transmission power, where less power is allowed to go to the ground, and thus more power is transmitted between the probe tips, as shown in Figure 4.13.

4.4 Fitting Data With vna.py

In addition to modeling RF signal transmission through a plasma of defined plasma parameters, we also wish to use vna.py to measure plasma parameters for experimental RF transmission data. The usual Python curve fitting methods may be used; we wrote worker routines to pass fit parameters into the `simulation` object and compare the output to the experimental data.

Figure 4.14 shows experimental data taken in the DODECA plasma chamber, and the simulated spectra created by fitting the data using the `simulation` class. The resulting n_e and T_e are shown in Figure 4.15. These values for T_e are overestimates: our model does not yet make any account for spectrum broadening due to gradients in n_e. The fit values of n_e were used to calculate related ω_{pe} values, which are plotted on

top of the experimental data in Figure 4.16. We have not yet completed uncertainty analysis.

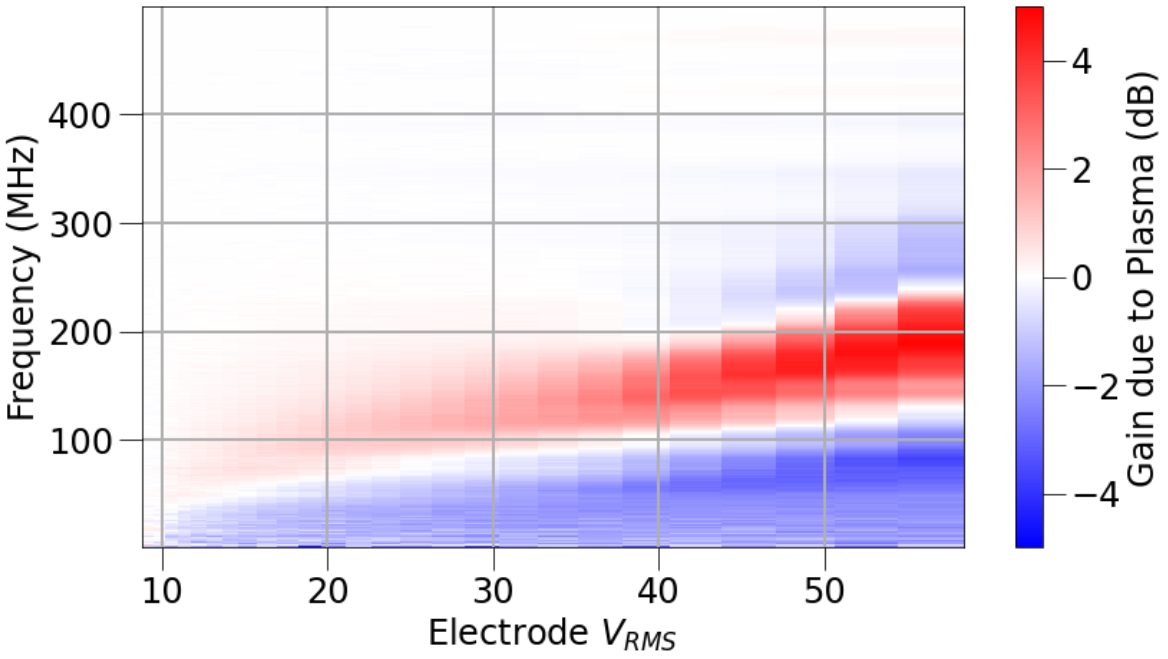

(a) Transmission spectra for a double probe immersed in a plasma in DODECA. The experiments were performed in the DODECA chamber with a neutral gas pressure of 6 Pa

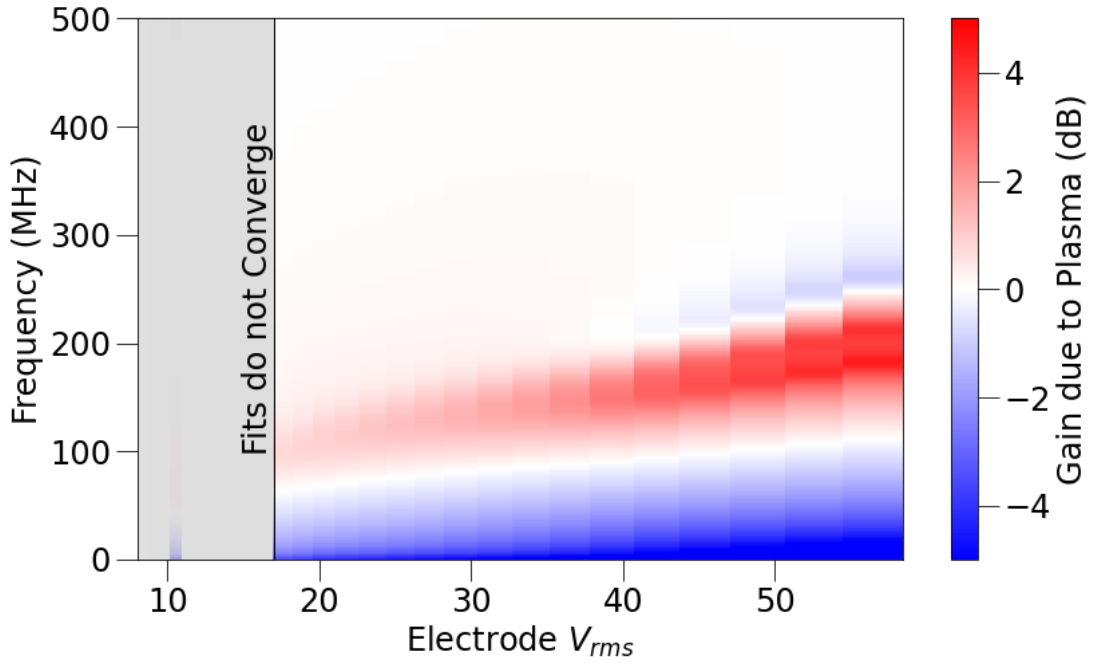

(b) Transmission spectra produced from the circuit simulation using plasma values determined from fitting the data in Figure 4.14b

Figure 4.14: Experimental data were fit using vna.py objects and methods.

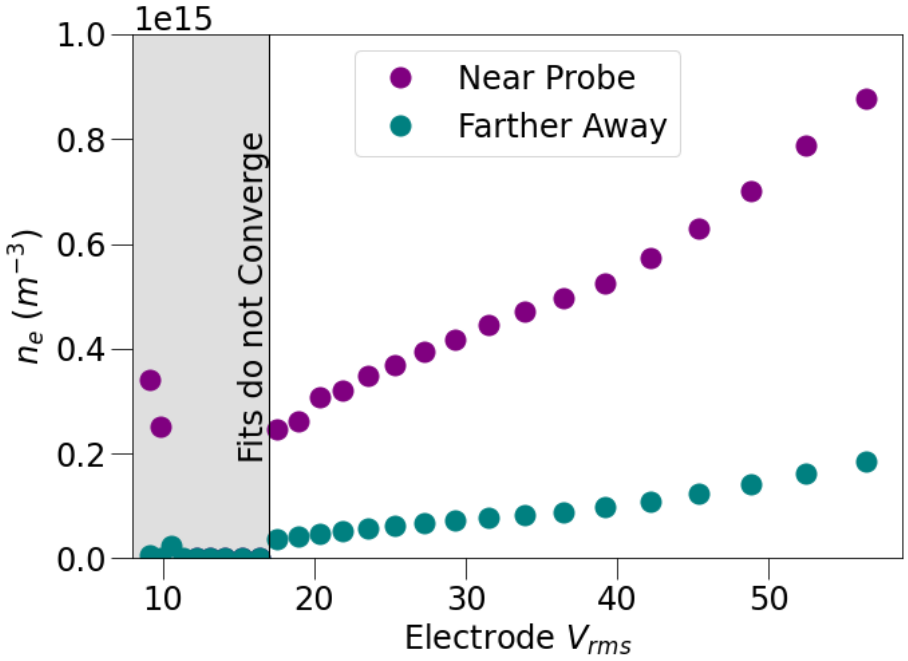

(a) n_e increased as electrode power increased. Especially in the area near the probe, in the center of the chamber. For low-voltage spectra, the probe tips were not fully immersed in the plasma, and the fits did not converge.

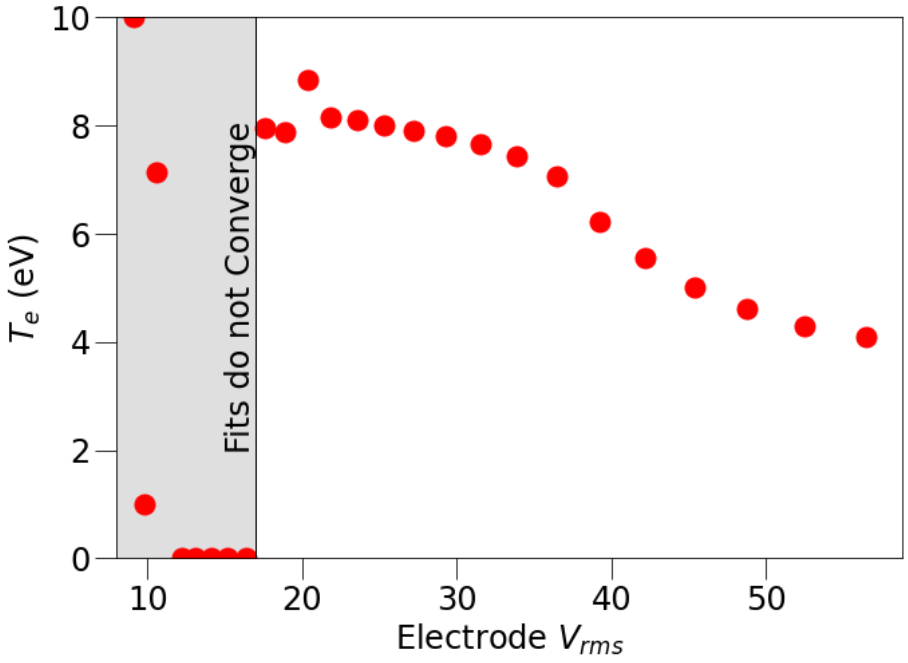

(b) T_e appears to have declined as electrode power increased. However, these measured values are higher than typical T_e values in an RF glow discharge such as DODECA. For low-voltage spectra, the probe tips were not fully immersed in the plasma, and the fits did not converge.

Figure 4.15: vna.py was used to determine plasma parameters from the data in Figure 4.14

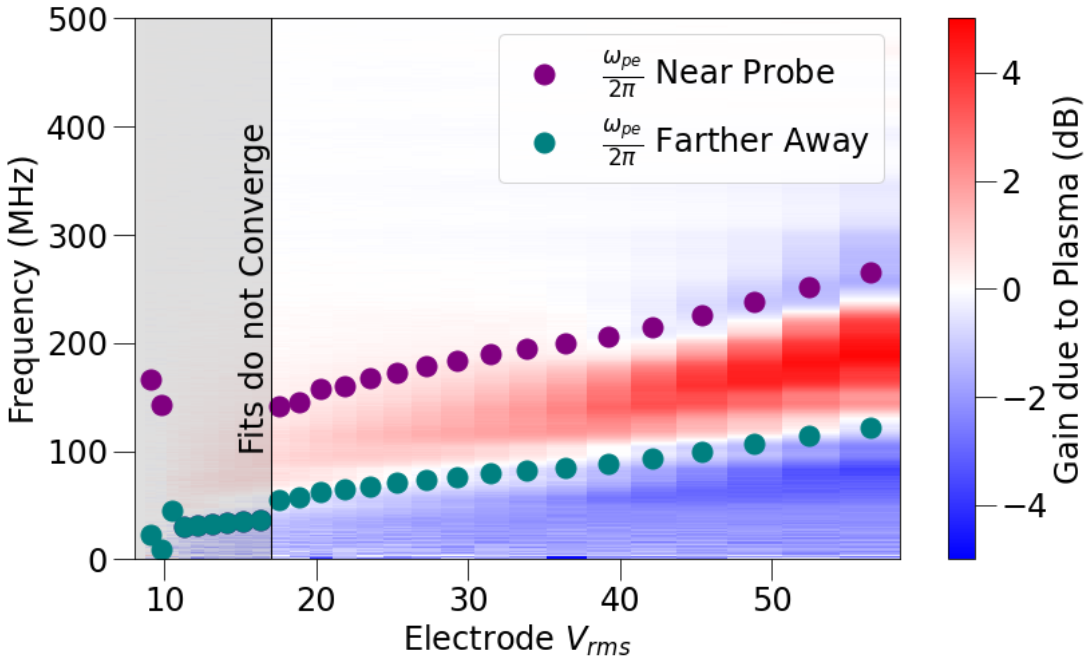

Figure 4.16: Transmission spectra for a double probe immersed in a plasma in DODECA. Dots show $2\pi\omega_{pe}$ calculated from the n_e found by fitting this data. For low-voltage spectra, the probe tips were not fully immersed in the plasma, and the fits did not converge.

Chapter 5

Conclusion and Outlook

Experiments were performed using transmission-type plasma impedance probes (TPIPs) in capacitively-coupled, RF glow discharge plasmas (Chapter 3). The resulting spectra were analyzed in two different ways: by fitting the data using a pair of Gaussian curves (Section 3.4.1) and by creating a robust circuit model analysis and simulation tool (Chapter 4). We shall compare these two analysis methods (Section 5.1), then we shall discuss the next steps in terms of experimental and theoretical/computational work for this topic (Sections 5.2 and 5.3).

5.1 Comparison of Analyses

Sections 3.4.1 and 4.4 present two very different methods of analyzing the same data. The first method describes the suppression of transmission due to plasma as a Gaussian-shaped suppression in the transmission spectrum. There are, therefore, a negative Gaussian curve associated with probe-probe transmission, and a positive Gaussian curve associated with the suppression of probe-wall transmissions. The second method begins with a plasma model, develops an associated circuit model describing the probe-plasma-chamber system, and uses SPICE algorithms to simulate the transmission in this circuit. Let us compare and contrast them here.

Figure 5.1 shows that both analysis techniques are able to qualitatively reproduce the shape of the transmission spectra to a satisfactory degree. The double-Gaussian fitting method more faithfully reproduces the image, especially the shapes of the frequency

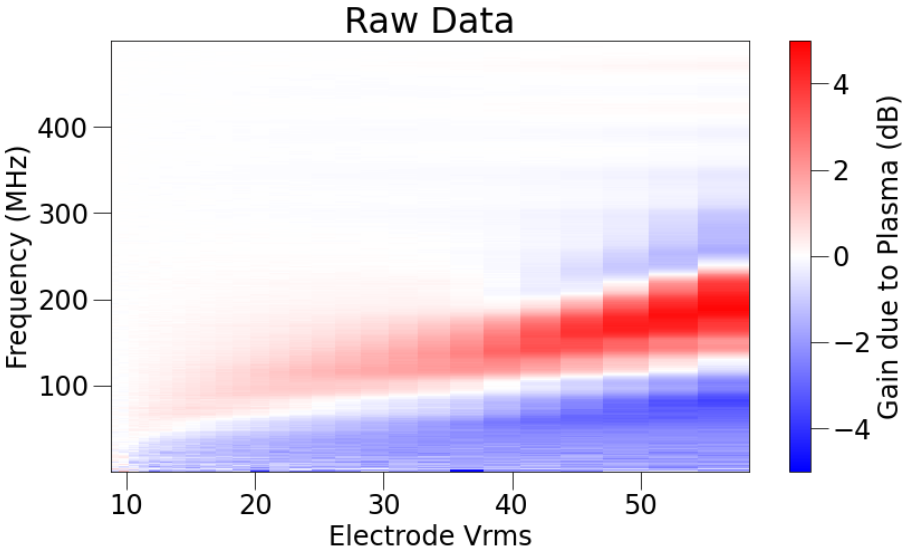

(a) We begin with the same data, from an RF transmission experiment performed in the DODECA plasma chamber with an ambient pressure of 6 Pa (45 mTorr).

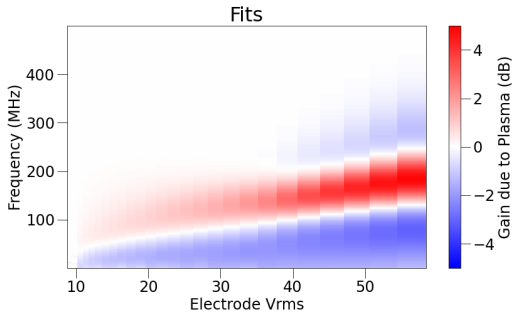

(b) The spectra above were fit two Gaussian curves, the resulting synthetic fit spectra are shown here

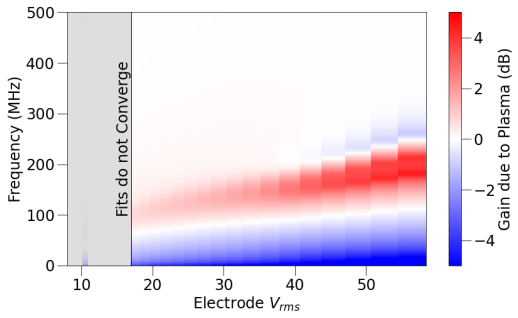

(c) The spectra above were fit using the `vna.py` package, the resulting synthetic fit spectra are shown here

Figure 5.1: Qualitatively speaking, both fitting methods reproduce the shape of the data to an acceptable degree, with the double-Gaussian fit method more closely resembling the data than the fits produced using the `vna.py` package.

ranges in which transmission was *suppressed*. We are nonetheless satisfied with the qualitative agreement between the data and the spectra produced using the `vna.py` package.

Turning now to quantitative analysis, Figure 5.2 tells a different story. In the regions where each fitting routine seemes to successfully reproduce the experimental spectra, the double-Gaussian fitting method indicates that the plasma density near the probes is *lower* than the density farther away. The physics-first, `vna.py` approach produces exactly the opposite result: the density near the probes is *higher* than the density far away. These two analyses, then, stand in direct opposition to each other in terms of their ability to determine plasma parameters from experimental spectra.

We trust the `vna.py` result more than the result from the double-Gaussian fit method for two reasons. First, the `vna.py` analysis is a physics-first analysis process. It starts with a fluid model for the electrons, develops a circuit model that reproduces the various modeled impedances in the plasma chamber, and uses SPICE algorithms to simulate the transmission spectra. Secondly, the result that n_e is higher in the center of the chamber agrees with the experimental observation that there is increased plasma glow in the center of the chamber as compared to the edges.

5.2 Future Experimental Work

There are various experimental improvements we are making to the RaFyL plasma chamber. These improvements will help in performing more robust experiments with and without dust. We also have begun very early development of RF transmission diagnostics in a form that might be more suitable for future microgravity experiments in the COMPACT plasma chamber.

5.2.1 RaFyL Development

We are continuing to develop the RaFyL plasma chamber for more robust experiments in this line of research. Recall (Section 3.1.2) that this plasma chamber produces

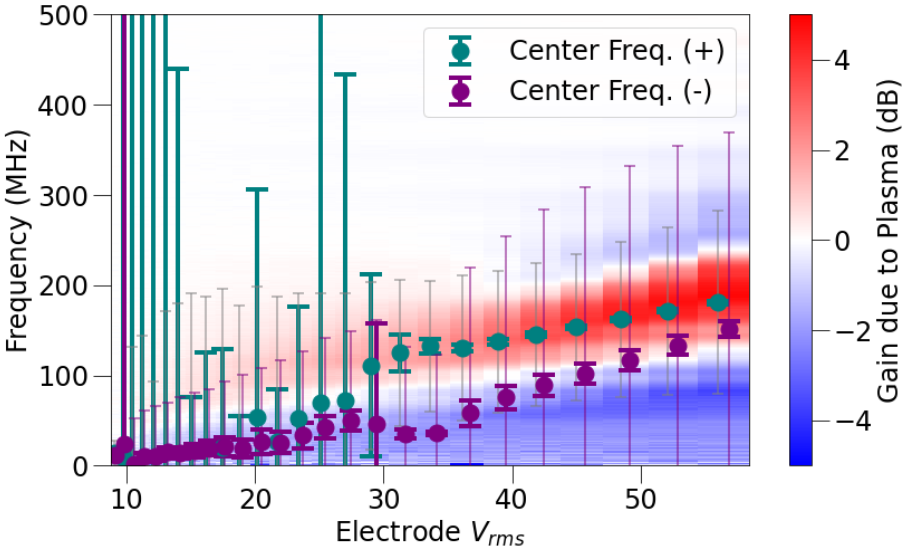

(a) Experimental spectra are shown with double Gaussian analysis superimposed. The dots show the center frequencies of the positive and negative Gaussian curves, which are assumed to represent the plasma frequency of plasma far from the probes and near the probes, respectively. The large bars show the usual 2σ uncertainty limits of the center frequencies. The small, fainter bars show the full width half maximum widths of these Gaussian curves used to fit the data.

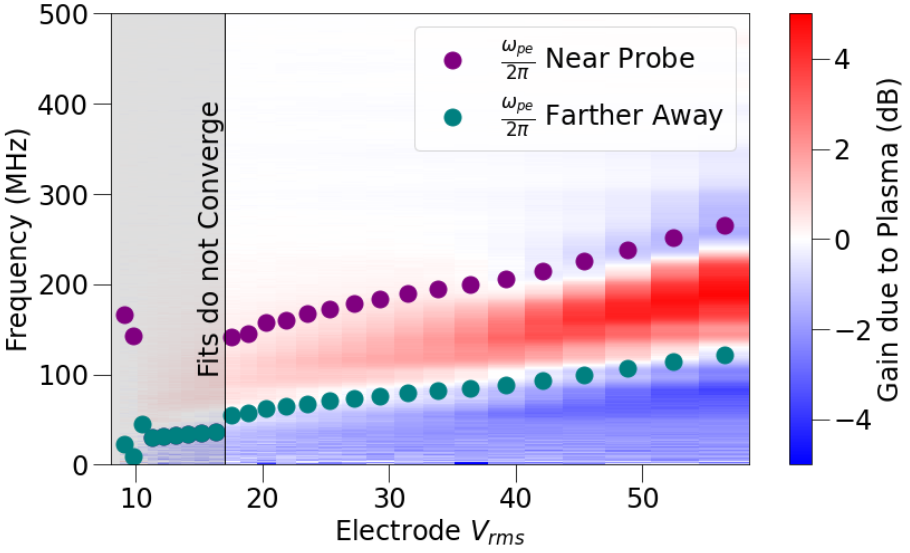

(b) Experimental spectra are shown with `vna.py` analysis superimposed. The dots show the plasma frequencies related to the plasma densities determined for plasma near the probes and plasma farther away in the chamber.

Figure 5.2: Quantitatively speaking, the results of the analyses are very different from each other. In the regions where each fitting routine seemed to successfully reproduce the spectra, the double-Gaussian fitting method indicates that the plasma density near the probes is *lower* than the density farther away. The physics-first, `vna.py` approach produces exactly the opposite result: the density near the probes is *higher* than the density far away. The `vna.py` result agrees with the experimental observation of increased plasma glow in the center of the chamber as compared to the edges.

plasmas whose plasma glows, and therefore presumably plasma densities, are more evenly distributed throughout the chamber, as compared to plasmas created in the DODECA plasma chamber. RF transmission impedance probe measurements are expected to more accurately measure T_e in this chamber, because the transmission effects of a strong ∇n_e cannot yet easily be distinguished from the transmission effects of high electron temperature.

We also are developing the probe measurement system to use the same probe tips to perform both RF transmission measurements as well as DC Langmuir probe measurements using the same probe tips (Figure 5.3). For experiments with dust, these DC measurements can be made using voltage pulses whose timescales lie between the reaction times of dust and ions.

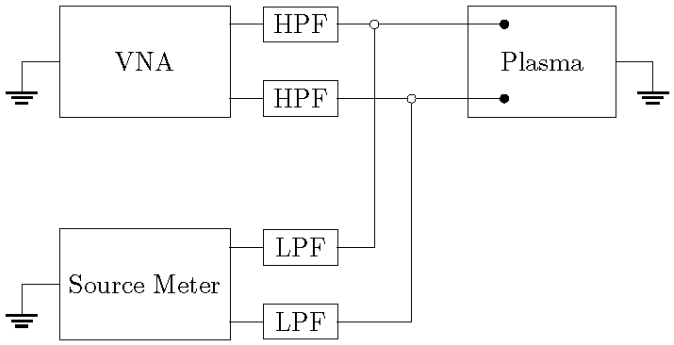

Figure 5.3: The measurement circuit will be improved to perform RF transmission measurements and DC Langmuir probe measurements using the same probe tips. The vector network analyzer (VNA) performs RF measurements, and the voltage source meter performs DC measurements. "HPF" and "LPF" stand for high-pass filter and low-pass filter, respectively.

5.2.2 Future Experiments

Having developed analysis tools to use TPIPs in glow discharge plasmas, there are several experiments we intend to perform. Firstly, we will perform experiments exploring the effect of the probe-to-probe spacing on TPIP measurements. These experiments will provide interesting insight into the changing nature of transmission

characteristics between the probes and out to the chamber wall as the capacitive coupling between the probe tips changes. These experiments will also help characterize the need for improving the model's treatment of plasma sheathes, especially for cases where the probes' sheathes overlap each other.

We will also implement these TPIP techniques in *dusty* plasmas. A few preliminary experiments were performed with dust, and we saw that further improvements are needed. As we discussed in Chapter 1, PIPs are *less* perturbing to dust and plasma than Langmuir probes, but that is not to say that they are *non*-perturbing. The probe tips electrically pushed dust particles away, forming dust voids (Figure 5.4).

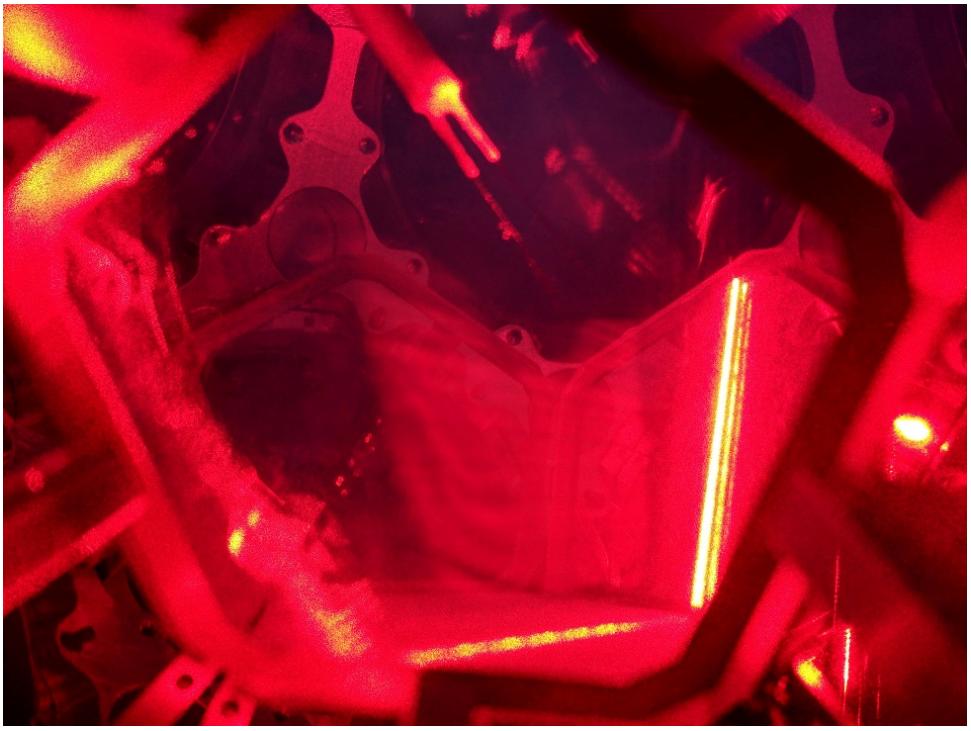

Figure 5.4: A plasma impedance double-probe forming a void in a dust cloud in the DODECA plasma chamber. The dust cloud is illuminated by a low-power laser spread vertically by a cylindrical lens. The laser's reflection off of the far electrode is clearly visible as a bright red line. The dust is more difficult to see in this image – it appears as a red haze left of that line.

The size of these voids may be controlled to some extent by changing the DC offset voltage of the probe [51, 56, 34]. It is our intention in future experiments with dust to use a DC offset to pull the dust closer to the probe tips.

5.2.3 COMPACT

We are working on performing transmission-type active plasma resonance spectroscopy (APRS) using electrodes in the plasma chamber as the "probes" for our TPIP diagnostic method (Figure 5.5). This will make the measurements truly non-perturbing to the dust and plasma. However, this is a difficult measurement to perform, requiring the high-voltage, 13.56 MHz signal powering the plasma (and its associated harmonics) to be strongly filtered out from the low-voltage signals we wish to measure in frequency ranges only a few tens of MHz above the power frequency. The COMPACT plasma chamber provides an opportunity to implement this measurement technique with out *needing* to filter out the powering frequency.

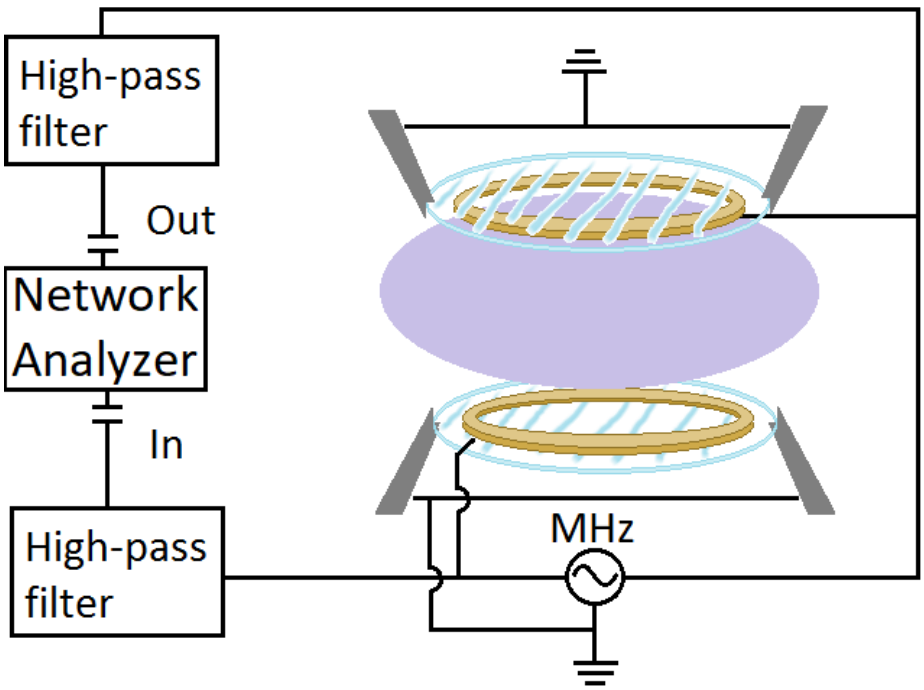

Figure 5.5: We are working on implementing transmission APRS as an electrode-to-electrode measurement utilizing the electrodes already present in the plasma chamber. This will make these RF transmission measurements truly non-perturbing to dust and plasma. However, sufficiently filtering out the power frequency is a difficult challenge.

COMPACT (Figure 5.6) is capacitively-coupled RF plasma device in development for future microgravity experiments for dusty plasma. One key feature of COMPACT is its innovative electrode configuration. COMPACT is a cylindrical device featuring

four electrodes, the usual top and bottom electrodes are each divided into a central circular electrode and an outer ring electrode. Each of these four electrodes is powered by its own individually-controllable RF voltage source. Further, each top/bottom electrode pair is actuated to change the electrode spacing in the plasma chamber, allowing for highly-configurable dust confinement characteristics.

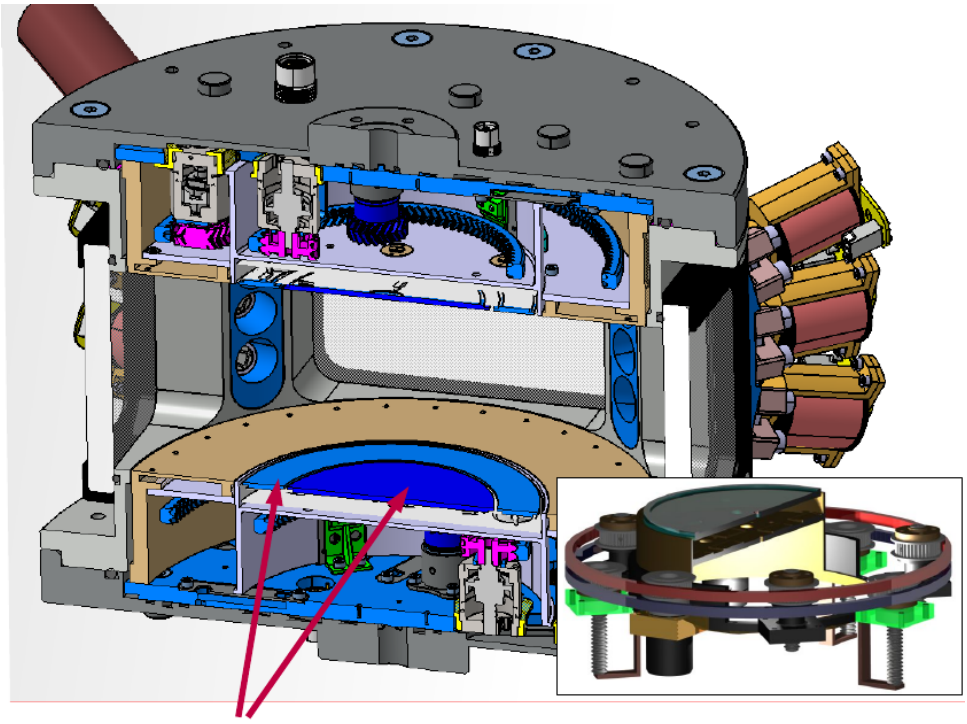

Figure 5.6: The COMPACT plasma chamber's advanced electrode design makes it a perfect candidate for performing electrode-to-electrode RF transmission measurements. Image courtesy of C. Knapek, DLR/University of Greifswald

We are exploring the possibility of performing APRS measurements in COMPACT by using two electrodes to power the plasma and two electrodes to perform transmission impedance measurements. As previously mentioned, this would allow the measurement to be non-perturbing to the dust and plasma. Also, this implementation is more conducive to space station experiments aboard the ISS, because there is no possibility of a failure-state of the measurement that leaves a probe protruding into the plasma, which could severely hamper experiments in COMPACT for the remainder of the campaign.

5.3 Future Modeling Work

There are two models involved with the analysis of these TPIP spectra. There is the computer circuit model that simulates the transmission of RF signals, and there is the plasma physics model which determines the values of elements of the circuit model. Both need some improvements.

5.3.1 vna.py Improvements

The model used in the analysis of the transmission PIP measurements has been developed to a functional level, but various improvements are underway. This includes streamlining the `vna.py` library – the library is easy to use to create simulations of plasma given a set of desired plasma parameters. However, using the library to analyze experimental data is still a functionality under construction.

Analysis of data using `vna.py` is currently achieved by writing a series of fitting algorithms that are effectively *wrappers* for the included `vna.py` objects and methods. Implementing these analysis methods directly into the `simulation` objects requires some structural changes to these objects. This improvement is underway, but is not completed at time of publishing this dissertation.

However, the most direly-needed improvement to the analysis of data is error estimation. Using the error estimation methods built into the usual scientific Python libraries *vastly* under-represent the error of these analyses. A robust treatment of the error of these methods is required, perhaps in a similar vein as the error analysis performed in Section 3.4.1.

5.3.2 Plasma Model Improvements

The main improvement needed to the theoretical model is the treatment of plasma sheathes. Some of the improvements may be easily made, and others are very difficult.

The easiest improvement needed is to include electron-neutral and ion-neutral collisions in the sheath width calculations. The ionization fraction in glow discharge plasmas is typically of the order of 10^{-6}, only about one atom in a million is ionized. Collisions with neutrals are a dominant effect in these types of plasmas, and they should be included in the sheath calculation.

Of the next order of difficulty is to model the sheathes as *lossy* capacitors, not pure capacitors. Recall that the capacitive sheath model is equivalent to the assumption that there are no electrons in the plasma sheath. As we have shown, this is simply not true. Firstly, if we *are* to make this approximation, the width of the plasma sheath is not the best characterization of the region devoid of electrons. We should be picking a width for our capacitance calculations based on where the electron density dips below a carefully-chosen cutoff value. Better yet, we can include small resistive and inductive components to the impedance of the sheath to represent the lossiness imparted by the electrons to the capacitive coupling across the sheath.

Lastly, we would like to better understand the coupling between probe tips that are close enough as to be within each other's sheath widths. There should be terms describing the probe-probe coupling through the reduced electron density in the region, the coupling between each probe and their combined sheath edge, and the coupling between this sheath edge and the plasma. *Properly* treating this scenario is a very complicated proposition, and threatens to turn into another dissertation worth of work. But there are likely improved approximations that can begin to address this shortcoming of the model.

References

[1] J E Allen. Probe theory - the orbital motion approach. *Physica Scripta*, 45(5):497, may 1992.

[2] JE Allen. The plasma–sheath boundary: its history and langmuir's definition of the sheath edge. *Plasma Sources Science and Technology*, 18(1):014004, 2008.

[3] S V Annibaldi, A V Ivlev, U Konopka, S Ratynskaia, H M Thomas, G E Morfill, A M Lipaev, V I Molotkov, O F Petrov, and V E Fortov. Dust-acoustic dispersion relation in three-dimensional complex plasmas under microgravity. *New Journal of Physics*, 9(9):327, sep 2007.

[4] J Basu and C Sen. Sheath thickness for a cylindrical or spherical probe placed in a plasma. *Japanese Journal of Applied Physics*, 12(7):1081, 1973.

[5] P.M. Bellan. *Fundamentals of Plasma Physics*. Cambridge University Press, 2008.

[6] N Bilik, R Anthony, B A Merritt, E S Aydil, and U R Kortshagen. Langmuir probe measurements of electron energy probability functions in dusty plasmas. *Journal of Physics D: Applied Physics*, 48(10):105204, feb 2015.

[7] D. D. Blackwell, C. D. Cothran, D. N. Walker, E. M. Tejero, G. R. Gatling, C. L. Enloe, and W. E. Amatucci. Advances in Impedance Probe Applications and Design in the NRL Space Physics Simulation Chamber. *IEEE Transactions on Plasma Science*, 43(8):2649–2657, 2015.

[8] David D. Blackwell, David N. Walker, and William E. Amatucci. Measurement of absolute electron density with a plasma impedance probe. *Review of Scientific Instruments*, 76(2):1–7, 2005.

[9] David D. Blackwell, David N. Walker, Sarah J. Messer, and William E. Amatucci. Characteristics of the plasma impedance probe with constant bias. *Physics of Plasmas*, 12(9):1–7, 2005.

[10] David L Book. *NRL plasma formulary*. Naval Research Lab., Washington, DC, 1983.

[11] Kenneth M Case. Plasma oscillations. *Annals of physics*, 7(3):349–364, 1959.

[12] Francis F. Chen. *Introduction to Plasma Physics and Controlled Fusion*. Springer Publishing Company, 2016.

[13] J. H. Chu and Lin I. Direct observation of coulomb crystals and liquids in strongly coupled rf dusty plasmas. *Phys. Rev. Lett.*, 72:4009–4012, Jun 1994.

[14] FW Crawford and RF Mlodnosky. Langmuir probe response to periodic waveforms. *Journal of Geophysical Research*, 69(13):2765–2773, 1964.

[15] V Fortov, G Morfill, O Petrov, M Thoma, A Usachev, H Hoefner, A Zobnin, M Kretschmer, S Ratynskaia, M Fink, et al. The project 'plasmakristall-4'(pk-4)—a new stage in investigations of dusty plasmas under microgravity conditions: First results and future plans. *Plasma physics and controlled fusion*, 47(12B):B537, 2005.

[16] J. Goree, G. E. Morfill, V. N. Tsytovich, and S. V. Vladimirov. Theory of dust voids in plasmas. *Phys. Rev. E*, 59:7055–7067, Jun 1999.

[17] R. S. Harp and F. W. Crawford. Characteristics of the Plasma Resonance Probe. *Journal of Applied Physics*, 35(12):3436–3446, 07 2004.

[18] B. J. Harris, L. S. Matthews, and T. W. Hyde. Dusty plasma cavities: Probe-induced and natural. *Phys. Rev. E*, 91:063105, Jun 2015.

[19] Brandon Joseph Harris, Lorin Swint Matthews, and Truell Wayne Hyde. Vertical-probe-induced asymmetric dust oscillation in complex plasma. *Physical Review E*, 87(5):053109, 2013.

[20] Y. Hayashi and K. Tachibana. Observation of coulomb-crystal formation from carbon particles grown in a methane plasma. *Jpn. J. Appl. Phys.*, 33:L804, 1994.

[21] Clifford J. Heath. Ad9959, 2017.

[22] Yoshi H Ichikawa and Hideo Ikegami. Theory of resonance probe. *Progress of Theoretical Physics*, 28(2):315–322, 1962.

[23] Hiroyuki Ikezi. Coulomb solid of small particles in plasmas. *The Physics of fluids*, 29(6):1764–1766, 1986.

[24] Harold Jeffreys and Bertha Jeffreys. *Cambridge mathematical library: Methods of mathematical physics*. Cambridge University Press, Cambridge, England, 3 edition, November 1999.

[25] R. V. KENNEDY and J. E. ALLEN. The floating potential of spherical probes and dust grains. ii: Orbital motion theory. *Journal of Plasma Physics*, 69(6):485–506, 2003.

[26] Sergey Khrapak, Peter Huber, Hubertus Thomas, Vadim Naumkin, Vladimir Molotkov, and Andrey Lipaev. Theory of a cavity around a large floating sphere in complex (dusty) plasma. *Phys. Rev. E*, 99:053210, May 2019.

[27] M. Klindworth, O. Arp, and A. Piel. Langmuir probe system for dusty plasmas under microgravity. *Review of Scientific Instruments*, 78(3), 2007.

[28] M. Klindworth, A. Piel, A. Melzer, U. Konopka, H. Rothermel, K. Tarantik, and G. E. Morfill. Dust-free regions around Langmuir probes in complex plasmas under microgravity. *Physical Review Letters*, 93(19):1–4, 2004.

[29] U Konopka, GE Morfill, and L Ratke. Measurement of the interaction potential of microspheres in the sheath of a rf discharge. *Physical review letters*, 84(5):891, 2000.

[30] U. Konopka, L. Ratke, and H. M. Thomas. Central collisions of charged dust particles in a plasma. *Physical Review Letters*, 79(7):1269–1272, 1997.

[31] S Vidhya Lakshmi, R Bharuthram, and PK Shukla. Debye shielding in a dusty plasma. *Astrophysics and space science*, 209:213–219, 1993.

[32] MARTIN LAMPE. Limits of validity for orbital-motion-limited theory for a small floating collector. *Journal of Plasma Physics*, 65(3):171–180, 2001.

[33] M. Lapke, J. Oberrath, T. Mussenbrock, and R. P. Brinkmann. Active plasma resonance spectroscopy: A functional analytic description. *Plasma Sources Science and Technology*, 22(2), 2013.

[34] Spencer Paul LeBlanc. *Investigation of Probe-Induced Dust Voids in a Weakly Magnetized Dusty Plasma*. PhD thesis, Auburn University, 2019.

[35] R. L. Merlino, A. Barkan, C. Thompson, and N. D'Angelo. Laboratory studies of waves and instabilities in dusty plasmas. *Physics of Plasmas*, 5(5):1607–1614, 05 1998.

[36] Robert L. Merlino. 25 years of dust acoustic waves. *Journal of Plasma Physics*, 80(6):773–786, 2014.

[37] Robert L. Merlino and John A. Goree. Dusty Plasmas in the Laboratory, Industry, and Space. *Physics Today*, 57(7):32–38, 07 2004.

[38] H. M. Mott-Smith and Irving Langmuir. The theory of collectors in gaseous discharges. *Physical Review*, 28(4):727–763, 1926.

[39] Anatoli P Nefedov, Gregor E Morfill, Vladimir E Fortov, Hubertus M Thomas, Hermann Rothermel, Tanja Hagl, Alexei V Ivlev, Milenko Zuzic, Boris A Klumov, Andrey M Lipaev, Vladimir I Molotkov, Oleg F Petrov, Yuri P Gidzenko, Sergey K Krikalev, William Shepherd, Alexandr I Ivanov, Maria Roth, Horst Binnenbruck, John A Goree, and Yuri P Semenov. Pke-nefedov*: plasma crystal experiments on the international space station. *New Journal of Physics*, 5(1):33, apr 2003.

[40] J. Oberrath and R. P. Brinkmann. Active plasma resonance spectroscopy: A kinetic functional analytic description. *Plasma Sources Science and Technology*, 23(4), 2014.

[41] J. L. Pack, R. E. Voshall, A. V. Phelps, and L. E. Kline. Longitudinal electron diffusion coefficients in gases: Noble gases. *Journal of Applied Physics*, 71(11):5363–5371, 06 1992.

[42] A Piel and A Melzer. Dynamical processes in complex plasmas. *Plasma Physics and Controlled Fusion*, 44(1):R1, dec 2001.

[43] Yoshifumi Saitou. A simple method of dust charge estimation using an externally applied oscillating electric field. *Physics of Plasmas*, 25(7):1–6, 2018.

[44] Mierk Schwabe, Sergey Zhdanov, T Hagl, Peter Huber, AM Lipaev, VI Molotkov, VN Naumkin, Milenko Rubin-Zuzic, PV Vinogradov, Erich Zähringer, et al. Observation of metallic sphere–complex plasma interactions in microgravity. *New Journal of Physics*, 19(10):103019, 2017.

[45] G. S. Selwyn, J. Singh, and R. S. Bennett. In situ laser diagnostic studies of plasma-generated particulate contamination. *Journal of Vacuum Science & Technology A*, 7(4):2758–2765, 07 1989.

[46] E. Spencer, S. Patra, T. Andriyas, C. Swenson, J. Ward, and A. Barjatya. Electron density and electron neutral collision frequency in the ionosphere using plasma impedance probe measurements. *Journal of Geophysical Research: Space Physics*, 113(9), 2008.

[47] Kazuo Takahashi, Jiashu Lin, Marie Hénault, and Laïfa Boufendi. Measurements of ion density and electron temperature around voids in dusty plasmas. *IEEE Transactions on Plasma Science*, 46(4):704–708, 2017.

[48] Kazuo Takahashi, Jiashu Lin, Marie Hénault, and Laïfa Boufendi. Measurements of ion density and electron temperature around voids in dusty plasmas. *IEEE Transactions on Plasma Science*, 46(4):704–708, 2018.

[49] K. Takayama, H. Ikegami, and S. Miyazaki. Plasma resonance in a radio-frequency probe. *Physical Review Letters*, 5(6):238–240, 1960.

[50] Xian-Zhu Tang and Gian Luca Delzanno. Orbital-motion-limited theory of dust charging and plasma response. *Physics of Plasmas*, 21(12):123708, 12 2014.

[51] E. Thomas, B. M. Annaratone, G. E. Morfill, and H. Rothermel. Measurements of forces acting on suspended microparticles in the void region of a complex plasma. *Phys. Rev. E*, 66:016405, Jul 2002.

[52] E. Thomas and R.L. Merlino. Dust particle motion in the vicinity of dust acoustic waves. *IEEE Transactions on Plasma Science*, 29(2):152–157, 2001.

[53] Edward Thomas, Ross Fisher, and Robert L Merlino. Observations of dust acoustic waves driven at high frequencies: Finite dust temperature effects and wave interference. *Physics of Plasmas*, 14(12), 2007.

[54] H. Thomas, G. E. Morfill, V. Demmel, J. Goree, B. Feuerbacher, and D. Möhlmann. Plasma crystal: Coulomb crystallization in a dusty plasma. *Phys. Rev. Lett.*, 73:652–655, Aug 1994.

[55] HM Thomas, GE Morfill, VE Fortov, AV Ivlev, VI Molotkov, AM Lipaev, T Hagl, H Rothermel, SA Khrapak, RK Suetterlin, et al. Complex plasma laboratory pk-3 plus on the international space station. *New journal of physics*, 10(3):033036, 2008.

[56] Jr. Thomas, E., K. Avinash, and R. L. Merlino. Probe induced voids in a dusty plasma. *Physics of Plasmas*, 11(5):1770–1774, 04 2004.

[57] Jr. Thomas, Edward. Measurements of spatially growing dust acoustic waves in a dc glow discharge plasma. *Physics of Plasmas*, 13(4):042107, 04 2006.

[58] Lewi Tonks and Irving Langmuir. Oscillations in ionized gases. *Phys. Rev.*, 33:195–210, Feb 1929.

[59] YA Ussenov, TS Ramazanov, KN Dzhumagulova, and MK Dosbolayev. Application of dust grains and langmuir probe for plasma diagnostics. *Europhysics Letters*, 105(1):15002, 2014.

[60] Bob Walch, Mihály Horányi, and Scott Robertson. Charging of dust grains in plasma with energetic electrons. *Phys. Rev. Lett.*, 75:838–841, Jul 1995.

Appendices

Appendix A

Sheath Width Calculation

A.1 Setup

Import sources and define useful variables:

[1]:
```
#Standard sources:
from matplotlib import pyplot as plt
import numpy as np
import math
from scipy.integrate import odeint
from scipy.integrate import solve_bvp
from scipy.optimize import fsolve

#My sources:
import plasma_resources as pr
locals().update(pr.con) #Bring in constants as individual variables
import bdd

#Need to explicitly set the Jupyter backend to
#  matplotlib so that bdd.plot_setup modifies the
#  correct plot environment:
%matplotlib inline
bdd.plot_setup('presentation',1.75)

#Useful plot variables:
from matplotlib import rcParams as rc
fs     = rc['font.size']       #font size
fs_sm  = fs*0.9
lw     = rc['lines.linewidth'] #line width
lw_sm  = lw/2
fgs    = rc['figure.figsize']  #figure size
fgs_stretch = fgs*np.array([1.1,1])
C0 = 'C0' #Plot color 0
C1 = 'C1' #Plot color 1
C2 = 'C2' #Plot color 2

#Global plot options:
match_axis_colors = True  #If false, all axis labels will be black

#Axis colors:
if match_axis_colors:
    ax_color_pot = C0
    ax_color_den = C1
else:
    ax_color_pot = 'Black'
```

```
    ax_color_den = 'Black'

#For bdd.save():
savedir='sheathWidth_images'
extensions = ['.png','.pdf']
save=True
#usage:
#bdd.save(fig,'test_figure',savedir,save,extensions)
```

Define some sample plasma parameters:

[2]:
```
Te = 3        #eV
Ti = 1/40     #eV
P  = 30       #Pa
ne = 1E16     #m**(-3)
ns = ne*0.61  #Sheath-edge density, for collisionless pre-sheath
rp = 0.0001   #(Cylindrical) probe radius, m
rw = 0.1      #(Spherical) chamber radius, m

Vf = -1*pr.v_float(Te) #Floating potential
Vp = -np.log(ne)*Te    #Assume simple botzmann electrons for␣
 ↪plasma potential
                       #  -> ne = exp[e*phi / kb*Te], with␣
 ↪|kb|=|e| for Te in eV

print(pr.v_float.__doc__)  #Show v_float documentation string
```

```
    plasma_resources.v_float(Te,gas='argon',mi=None)

    Calculates v_float from Langmuir Theory

    Var |dtype | Optnl | Default | Alternatives | Description
  ↪␣
↪-------------------------------------------------------------------------
    Te  | dbl  | no    |         |              | Electron␣
↪temperature (eV)
        |      |       |         |              |
    gas | str  | yes   | 'argon' |   'krypton'  | Will calculate mi␣
↪for gas,
        |      |       |         |  'hydrogen'  |   unless mi is␣
↪not None.
        |      |       |         |              |
    mi  | dbl  | yes   |  None   |              | Ion mass (kg)
        |      |       |         |              |   overrides gas␣
↪input
```

A.2 Solving for Probe Sheath Width

We need to solve Poisson's Equation:

$$\nabla^2\phi(r) = \frac{e}{\epsilon_0}(n_e - n_i)$$

We assume Boltazmann electrons,

$$n_e(r) = n_s e^{e\phi(r)/k_B T_e}$$

where n_s is the plasma density at the sheath edge. Noting that for T_e in units of eV, $k_B = 1.602 \times 10^{-19}\ J/eV$, we will simply write,

$$n_e(r) = n_s e^{\phi(r)/T_e}$$

We assume that ions enter the sheath with the Bohm velocity and flow continuously to the probe surface. We may then write Poisson's Equation as:

$$\nabla^2\phi(r) = A\left(e^{\phi(r)/T_e} - (1 - B\phi(r))^{-1/2}\right)$$

with

$$A = \frac{n_s e}{\epsilon_0}$$

$$B = \frac{2e}{m_i u_B^2} = \frac{2}{T_e}$$

Writing ∇^2 explicitly for cylindrical geometry:

$$\frac{1}{r}\frac{\partial}{\partial r}\left(r\frac{\partial\phi}{\partial r}\right) = A\left(e^{\phi(r)/T_e} - \frac{s}{r}(1 - B\phi(r))^{-1/2}\right)$$

$$\phi'' = A\left(e^{\phi(r)/T_e} - \frac{s}{r}(1 - B\phi(r))^{-1/2}\right) - \frac{\phi'}{r}$$

SciPy's odeint() can't directly handle 2^{nd}-order differential equations, so we re-write this as a system of two 1^{st}-order ODEs with the following change of variable:

$$z = \begin{bmatrix} z_0 \\ z_1 \end{bmatrix} = \begin{bmatrix} \phi' \\ \phi \end{bmatrix}$$

$$z' = \begin{bmatrix} z_0' \\ z_1' \end{bmatrix} = \begin{bmatrix} A\left(e^{z_1/T_e} - \frac{s}{r}(1 - Bz_1)^{-1/2}\right) - \frac{z_0}{r} \\ z_0 \end{bmatrix}$$

We know three boundary conditions for $\phi(r)$ in the sheath:

(1) $\phi(r_{sheath}) = 0$

(2) $\phi'(r_{sheath}) = 0$

(3) $\phi(r_{probe}) = -V_{float}$

We shall write a function that uses BCs (1) and (2) to solve Poisson's Equation, then we shall use scipy.optimize.fsolve() to find the sheath thickness for which ϕ conforms to BC (3)

Solver functions:

[3]:
```
#Redefine 2nd order ODE as system of
#1st order ODEs: z=[Phi',Phi] so z'=[Phi",Phi']
A  = ns*e/e0
B = 2/Te

#dz/dr, where z=[phi',phi] and dz/dr=[phi",phi']
#odeint() repeatedly passes z and r as values
#at individual points, r
def dz(z,r,s,geometry='cylindrical'):
    if 'cyl' in geometry.lower(): #Cylindrical geometry (default)
        der = np.array((
            #z'[0] (which is phi"):
            A*(np.exp(z[1]/Te) - s/r*(1-B*z[1])**(-1/2)) - z[0]/r,
            #z'[1] (which is phi'):
            z[0]
            ))
        return der
    if 'sph' in geometry.lower(): #Spherical geometry
        der = np.array((
            #z'[0] (which is phi"):
            A*(np.exp(z[1]/Te) - (s/r)**2*(1-B*z[1])**(-1/2))\
                - 2*z[0]/r,
            #z'[1] (which is phi'):
            z[0]
            ))
        return der
    if 'pla' in geometry.lower(): #Planar geometry
        der = np.array((
            #z'[0] (which is phi"):
            A*(np.exp(z[1]/Te) - (1-B*z[1])**(-1/2)),
            #z'[1] (which is phi'):
            z[0]
            ))
        return der
    print('dz(z,r,s,geometry): Unknown ODE geometry!')
    return

#Function to be minimized
#diff() returns (target potential)-(sheath potential)
#for a given sheath thickness. The shathe thickness
#variable, sheath, MUST be a list but it MAY
#be a list with only one element.
def diff(sheath,z0=[0,0],surface='probe',geometry='cylindrical'):
    if surface.lower() in ['probe','p']:
        s = rp + sheath[0]
        r = np.linspace(s,rp,200)
        t = Vf #The target potential is the floating potential.
    elif surface.lower() in ['wall','w','chamber','c']:
        s = rw - sheath[0]
        r = np.linspace(s,rw,200)
```

```
        t = Vp #Vp instead of Vf; chamber wall is grounded
    else:
        print('diff(sheath,Z0,surface): Unknown surface type!')
        return
    d_phi,phi = odeint(dz,z0,r,args=(s,geometry)).T
    diff = t - (phi[-1]-z0[1])
    return diff
```

Literature Comparison:

Basu and Sen (1973) provide an approximate expression for the sheath width for a cylindrical probe tip:

$$s'^2 + 4.0 = m_1(\eta_p + 3.5)$$

where

$$m_1 = 0.59 + 1.86 a'^{0.47}$$

s' is the sheath thickness normalized by the Debye length:

$$s' = \frac{r_{sheath} - r_{probe}}{\lambda_D}$$

and η_p is the probe's floating potential normalized by the electron temperature:

$$\eta_p = \frac{v_{float}}{T_e}$$

The sheath width expression above is valid only for $\eta_p \gtrsim 3$

[4]:
```
#Basu and Sen 1973:
def d_sheath_bs(Te,ns,r_probe=0.0001):
    lambda_D = pr.lambda_D(Te,ns)
    m1 = 0.59 + 1.86 * (r_probe/lambda_D)**0.47
    eta = pr.v_float(Te)/Te
    d = (m1*(eta+3.5)-4.0)**(1/2) * lambda_D
    return d
```

Run the solver:

[5]:
```
guess = 0.001 #Initial guess for sheath thickness
z0    = [0,0] #Phi and Phi' at sheath boundary
args = (z0,'probe','cylindrical')
ans = fsolve(diff,guess,args=args)[0]
print('Sheath thickness for {} {} sheath: {:.2f} mm'\
      .format(args[2],args[1],ans*1000))
s_probe_IVP = ans*1000
```

```
Sheath thickness for cylindrical probe sheath: 0.58 mm
```

[6]:
```
#Draw a demonstration of how we found the width:

#Find DeltaV across sheath for range of sheath thicknesses:
sheaths = np.linspace(0.1,1,100)
DVs = np.empty(100)
for i in range(len(sheaths)):
    DVs[i]=diff([sheaths[i]/1000]) + (-Vf)

#Prepare plot
fig,ax=plt.subplots()
ax.set_xlim([sheaths[0],sheaths[-1]])
ax.set_title('Probe Sheath: Potential vs Width')
ax.set_ylabel(r'$\Delta \phi$ Across Sheath (V)',\
              labelpad=18)
ax.set_xlabel('Sheath Width (mm)')

#Draw and label floating potential:
ax.plot(sheaths,[-Vf]*len(sheaths),color='black',\
        ls='dotted')
ax.text(0.3,-Vf+2,'Floating Potential',va='center',\
        ha='center',fontsize=fs_sm)

#Draw and label DeltaV across sheath:
ax.plot(sheaths,DVs,color='C0')
ax.text(sheaths[80]+.04,DVs[80]-.04,'Sheath Potential',\
        rotation=49,ha='center',va='center',\
        fontsize=fs_sm,color='C0')

#Show where they intersect:
ax.axvline(x=ans*1000,color='blue',ls='dotted')
ax.text(ans*1000-0.03,35,'Numerical Solution',\
        rotation=90,color='blue',\
        va='center',ha='center',\
        fontsize=fs_sm)

#Show Basu & Sen's approximation:
ax.axvline(x=d_sheath_bs(Te,ns)*1000,color='red',\
           ls='dotted')
ax.text(d_sheath_bs(Te,ns)*1000+0.04,35,'Basu & Sen (1973)',\
        rotation=90,color='red',va='center',\
        ha='center',fontsize=fs_sm)

#Save:
bdd.save(fig,'probe_solution_IVP',savedir,save,extensions)
```

```
PNG Saved Successfully
PDF Saved Successfully
```

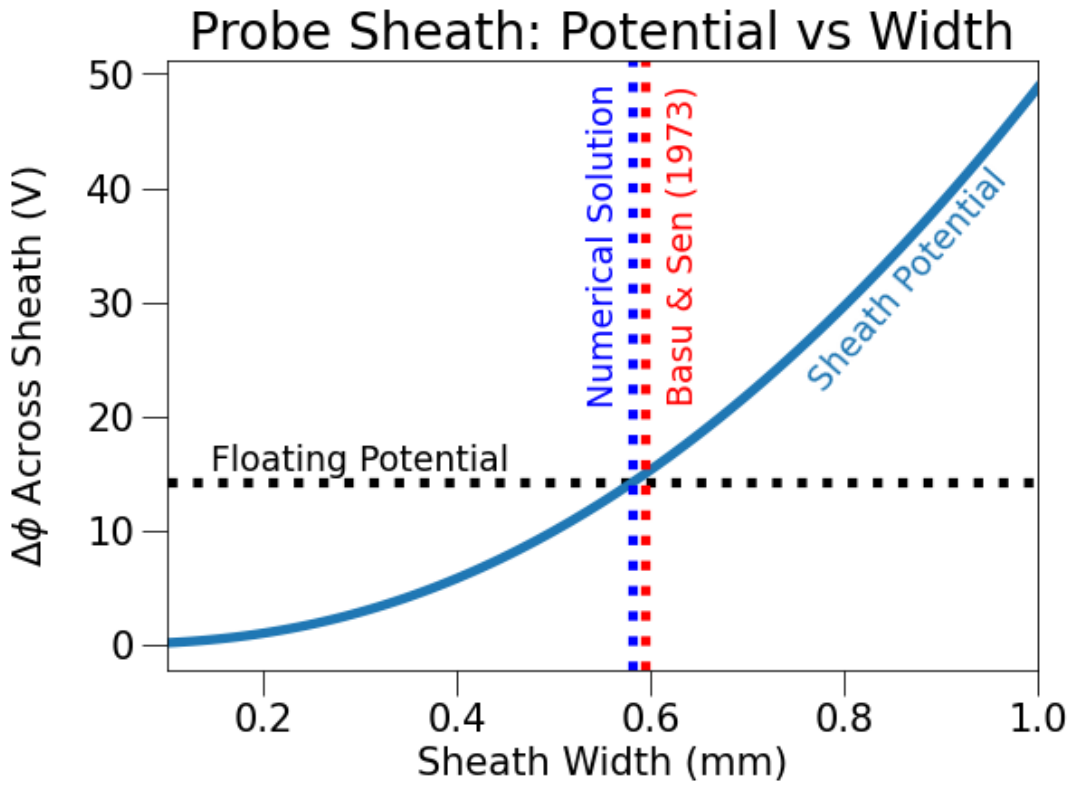

[7]:
```
#Now that we've solved it, let's draw the sheath:

#Solve for sheath:
s = rp + ans
r = np.linspace(s,rp,200)
z0=[0,0]
geometry='cylindrical'
d_phi,phi = odeint(dz,z0,r,args=(s,geometry)).T

#Useful dimensions and locations for plot:
xlim=[0,s*1250]
ylim = [-20,5] #y limits
lab_loc=ylim[0]+(ylim[1]-ylim[0])*.1
vert_space = (ylim[1]-ylim[0])*.05
horiz_space = (xlim[1]-xlim[0])*0.025
ymid = ylim[0]+(ylim[1]-ylim[0])/2
xmid = xlim[0]+(xlim[1]-xlim[0])/2
ro1,phio1 = r*1000,phi

#Set up plot:
fig,ax=plt.subplots(figsize=fgs_stretch)
ax.set_xlim(xlim)
ax.set_ylim(ylim)
ax.grid(False)
ax.tick_params(axis='y', labelcolor=ax_color_pot)
ax.set_title('Probe Sheath')
ax.set_xlabel('Radius (mm)',fontsize=fs)
ax.set_ylabel('Potential (V)',fontsize=fs,\
              color=ax_color_pot,ha='center')
```

```
#Draw and label sheath potential:
ax.plot(r*1000,phi,lw=lw,label=r'$\phi (r)$')
ax.text(r[30]*1000,phi[30]+1,r'$\phi(r)$',\
        color=C0,ha='center')

#Draw probe and bulk:
ax.fill_between([xlim[0],rp*1000],[ylim[0]]*2,\
                [ylim[1]]*2,color='#D3D3D3')
ax.fill_between([xlim[1], s*1000],[ylim[0]]*2,\
                [ylim[1]]*2,color='#D8BFD8')
ax.axvline(x=rp*1000,color='black',ls='solid',lw=1)
ax.axvline(x=s*1000,color='black',ls='solid',lw=1)

#r=s label:
ax.text(s*1000-horiz_space,lab_loc,'r=s',\
        color='gray',rotation=90,va='center',\
        ha='center',fontsize=fs_sm)

#Draw and label floating potential:
ax.plot([xlim[0],rp*1000],[Vf]*2,lw=lw,\
        ls='dotted',color=C0)
ax.text(rp*500+xlim[0]*0.5,Vf+1.5,r'$V_{float}$',\
        va='center',ha='center',\
        color=C0,fontsize=fs_sm)

#Daw and label plasma (bulk) potential:
ax.plot([s*1000,xlim[1]],[0,0],lw=lw,\
        ls='dotted',color=C0)
ax.text((s*1000+(xlim[1]-s*1000)/2),1.5,\
        r'$\phi = 0$',va='center',\
        ha='center',color=C0,\
        fontsize=fs_sm)

#Prepare density axis:
ax2 = ax.twinx()
ax2.grid(False)
ax2.tick_params(axis='y', labelcolor=ax_color_den)
ylim_ne=[1e10,1e20]
ax2.set_ylim(ylim_ne)
ax2.set_ylabel(r'Density ($m^{-3}$)',ha='center',\
               fontsize=fs,color=ax_color_den)

#Draw densities:
nes = ns*np.exp(phi/Te)
nis = ns*s/r*(1-B*phi)**(-1/2)
ax2.semilogy(r*1000,nis,color=C1,ls='dashed',\
             label=r'$n_i(r)$')
ax2.semilogy(r*1000,nes,color=C1,ls='solid',\
             label=r'$n_e(r)$')
ax2.plot([s*1000,xlim[1]],[ns]*2,lw=lw,\
         ls='dotted',color=C1)

#Label densities:
ax2.text(r[30]*1000,nes[30]*.1,r'$n_e(r)$',\
         color=C1,ha='center')
ax2.text(r[30]*1000,nis[30]*3,r'$n_i(r)$',\
         color=C1,ha='center')
ax2.text((s*1000+(xlim[1]-s*1000)/2),ns*0.2,\
         r'$n_{e,i} = n_s$',va='center',ha='center',\
         color=C1,fontsize=fs_sm)

#Stuff that goes on top needs a separate axis:
```

```
top_ax = ax.twinx()
top_ax.set_ylim(ylim)
top_ax.grid(False)
top_ax.set_yticks([])       #Don't draw y-axis ticks
top_ax.set_yticklabels([]) #Don't draw y-axis numbers

#Label probe, sheath, and bulk:
top_ax.text(xlim[0]+(rp*1000-xlim[0])/2,lab_loc,\
            'Probe',color='black',\
            va='center',ha='center',\
            fontsize=fs_sm)
top_ax.text(rp*1000+(s-rp)/2*1000,lab_loc,\
            'Sheath',color='black',\
            va='center',ha='center',\
            fontsize=fs_sm)
top_ax.text(s*1000+(xlim[1]-s*1000)/2,lab_loc,\
            'Bulk\nPlasma',color='black',\
            va='center',ha='center',\
            fontsize=fs_sm)

#Draw and label Debye length:
lam=np.array([0,pr.lambda_D(Te,ne)]) + rp
top_ax.plot(lam*1000,[2]*2,color='black',marker='|',\
            ms=20,markeredgewidth=lw,lw=lw)
top_ax.text(np.average(lam)*1000,3.2,r'$\lambda_{D}$',\
            va='center',ha='center',fontsize=fs_sm)

#Save:
bdd.save(fig,'probe_sheath_IVP',savedir,save,extensions)
```

```
PNG Saved Successfully
PDF Saved Successfully
```

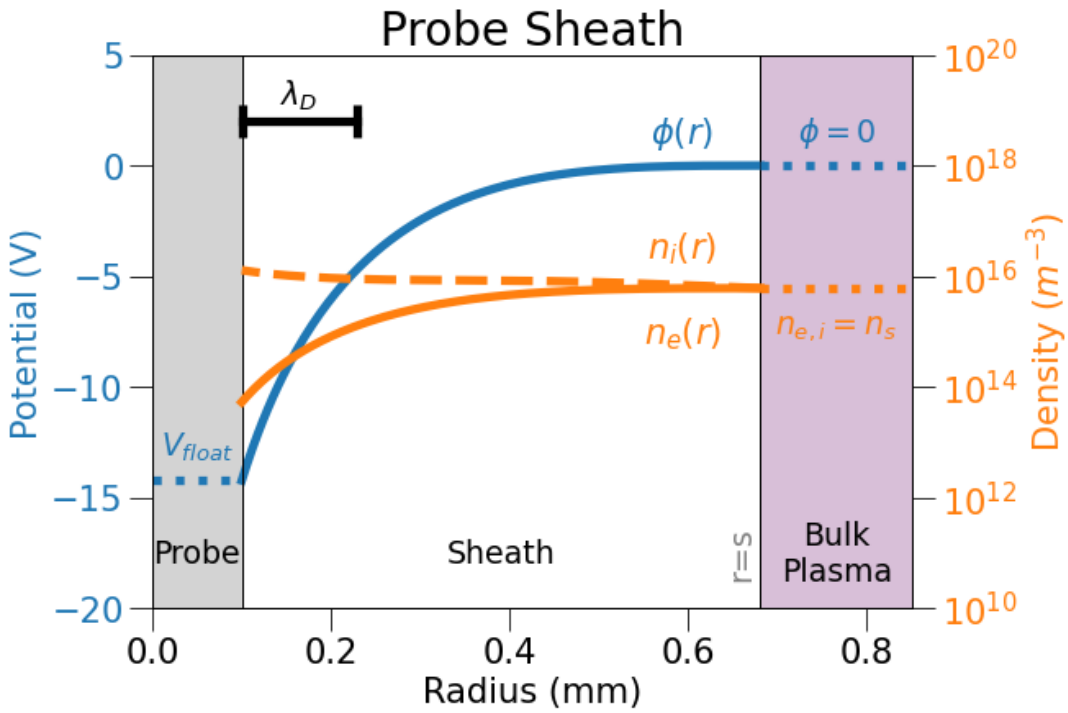

A.3 Chamber wall:

We may solve for the wall sheath thickness in the same way.

However, in the case of a chamber wall, when the surface area of the object is larger than the surface area of the plasma sheath boundary, there is one snag that must be avoided: one possible solution to the differential equation is for bulk plasma to continue all the way to the chamber wall. One can think of this as the trivial solution to the differential equation. However, this trivial solution is highly unstable; a small perturbation in the electron or ion density would cause the arrangement to collapse to a more stable density and potential structure. And therefore, this is not a physically realistic solution, and we would like to avoid obtaining it.

One way to avoid this by cheating on the conditions for ϕ the sheath boundary condition. The true boundary condition is:

$$z_0 = \begin{bmatrix} \phi \\ \phi' \end{bmatrix} = \begin{bmatrix} 0 \\ 0 \end{bmatrix}$$

We artifically nudge the potential donwards at the sheath edge to avoid our ODE solver finding the trivial solution:

$$z_0 = \begin{bmatrix} \phi \\ \phi' \end{bmatrix} = \begin{bmatrix} 0 \\ -0.5\ V/m \end{bmatrix}$$

[8]:
```
guess = 0.004 #Initial guess for sheath thickness
z0    = [0,-0.5] # artifically nudge the potential downwards
args = (z0,'chamber','spherical')
ans = fsolve(diff,guess,args=args)[0]
print('Sheath thickness for {} {} sheath: {:.2f} mm'\
      .format(args[2],args[1],ans*1000))
s_wall_IVP = ans*1000
```

```
Sheath thickness for spherical chamber sheath: 3.79 mm
```

[10]:
```
#Draw a demonstration of how we found the width:

#Find DeltaV across sheath for range of sheath thicknesses:
sheaths = np.linspace(1,6,100)
DVs = np.empty(100)
for i in range(len(sheaths)):
    DVs[i]=diff([sheaths[i]/1000],*args) + (-Vp)

#Prepare plot:
fig,ax=plt.subplots()
ax.set_xlim([sheaths[0],sheaths[-1]])
ax.set_title('Wall Sheath: Potential vs Width')
ax.set_ylabel(r'$\Delta \phi$ Across Sheath (V)',\
              labelpad=18)
ax.set_xlabel('Sheath Width (mm)')

#Draw and label plasma potential:
ax.plot(sheaths,[-Vp]*len(sheaths),color='black',\
        ls='dotted')
ax.text(2,-Vp+10,'Plasma Potential',va='center',\
        ha='center',fontsize=fs_sm)

#Draw and label sheath potential:
ax.plot(sheaths,DVs,color='C0')
ax.text(sheaths[80],DVs[80]+15,'Sheath Potential',\
        rotation=42,ha='center',va='center',\
        fontsize=fs_sm,color='C0')

#Show where they intersect:
ax.axvline(x=ans*1000,color='blue',ls='dotted')
ax.text(ans*1000-0.12,200,'Numerical Solution',\
        rotation=90,color='blue',va='center',\
        ha='center',fontsize=fs_sm)

#Save:
bdd.save(fig,'wall_solution_IVP',savedir,save,extensions)
```

```
PNG Saved Successfully
PDF Saved Successfully
```

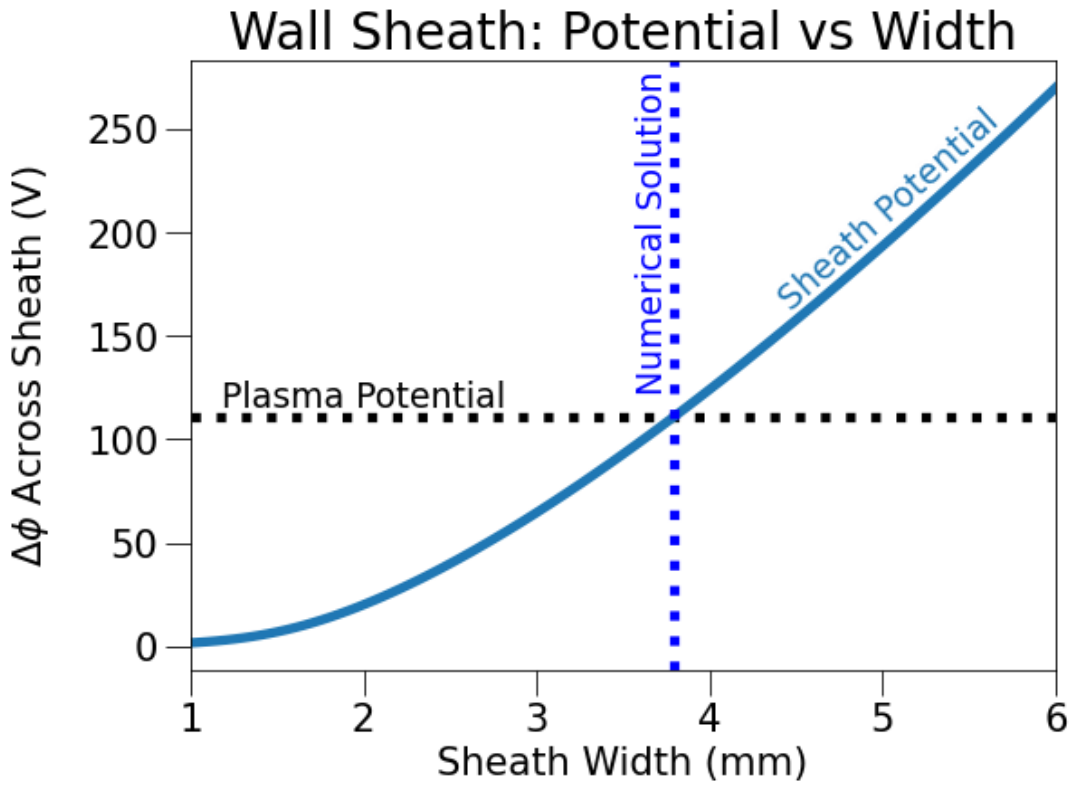

[12]:
```
#Now that we've solved it, let's draw the sheath:

#Solve for sheath:
s = rw - ans
r = np.linspace(s,rw,200)
surface='wall'
geometry='spherical'
d_phi,phi = odeint(dz,z0,r,args=(s,geometry)).T

#Useful dimensions and locations for plot:
xlim = [95,100.9]
ylim = [-150,50]
lab_loc=ylim[0]+(ylim[1]-ylim[0])*.075
vert_space = (ylim[1]-ylim[0])*0.05
horiz_space = (xlim[1]-xlim[0])*0.025
ymid = ylim[0]+(ylim[1]-ylim[0])/2
xmid = xlim[0]+(xlim[1]-xlim[0])/2
ro,phio = r*1000,phi

#Set up plot:
fig,ax=plt.subplots(figsize=fgs_stretch)
ax.set_xlim(xlim)
ax.set_ylim(ylim)
ax.grid(False)
ax.tick_params(axis='y', labelcolor=ax_color_pot)
ax.set_xlabel('Radius (mm)',fontsize=fs)
ax.set_ylabel('Potential (V)',fontsize=fs,\
              color=ax_color_pot)
ax.set_title('Wall Sheath')
```

```
#Plot sheath potential:
ax.plot(r*1000,phi,lw=lw,label=r'$\phi (r)$')

#Draw bulk and chamber wall:
ax.fill_between([xlim[0], s*1000],[ylim[0]]*2,\
                [ylim[1]]*2,color='#D8BFD8')
ax.fill_between([xlim[1],rw*1000],[ylim[0]]*2,\
                [ylim[1]]*2,color='#D3D3D3')
ax.axvline(x=s*1000,color='black',ls='solid',lw=1)
ax.axvline(x=rw*1000,color='black',ls='solid',lw=1)

#r=s label:
ax.text(s*1000+horiz_space,lab_loc,'r=s',\
        color='gray',rotation=90,\
        va='center',ha='center',\
        fontsize=fs_sm)

#Draw and label V_plasma at the wall:
ax.plot([rw*1000,xlim[1]],[Vp]*2,lw=lw,\
        ls='dotted',color=C0)
ax.text((rw+(xlim[1]/1000-rw)/2)*1000,\
        Vp+vert_space,r'$-V_p$',va='center',\
        ha='center',color=C0,fontsize=fs)

#Draw and label V_bulk:
ax.plot([xlim[0],s*1000],[0,0],lw=lw,\
        ls='dotted',color='C0')
ax.text(xlim[0]+(s*1000-xlim[0])/2,\
        vert_space,r'$\phi = 0$',\
        va='center',ha='center',\
        color=C0,fontsize=fs)

#Prepare density axis:
ax2 = ax.twinx()
ax2.tick_params(axis='y', labelcolor=ax_color_den)
ylim_ne=[1e10,1e20]
ax2.set_ylim(ylim_ne)
ax2.grid(False)
ax2.set_ylabel(r'Density ($m^{-3}$)',ha='center',\
               fontsize=fs,color=ax_color_den)

#Draw densities:
nes = ns*np.exp(phi/Te)
nis = ns*s/r*(1-B*phi)**(-1/2)
ax2.semilogy(r*1000,nis,color=C1,ls='dashed',\
             label=r'$n_i(r)$')
ax2.semilogy(r*1000,nes,color=C1,\
             label=r'$n_e(r)$')
ax2.plot([xlim[0],s*1000],[ns]*2,lw=lw,\
         ls='dotted',color=C1)

#Label densities:
ax.text(r[30]*1000,phi[30]+vert_space*.75,\
        r'$\phi(r)$',color=C0,\
        ha='center')
ax2.text(r[30]*1000,nes[30]*.1,r'$n_e(r)$',\
         color=C1,ha='center')
ax2.text(r[30]*1000,nis[30]*3,r'$n_i(r)$',\
         color=C1,ha='center')
ax2.text((xlim[0]+s*1000)*0.5,ns*.2,\
         r'$n_{e,i} = n_s$'\
         ,va='center',ha='center',\
```

```
          color=C1,fontsize=fs_sm)

#Stuff that goes on top needs a separate axis:
top_ax = ax.twinx()
top_ax.set_ylim(ylim)
top_ax.grid(False)
top_ax.set_yticks([])       #Don't draw y-axis ticks
top_ax.set_yticklabels([]) #Don't draw y-axis numbers

#Label bulk, sheath, and chamber wall:
top_ax.text(xlim[0]+(s*1000-xlim[0])/2,lab_loc,\
            'Bulk\nPlasma',color='black',\
            va='center',ha='center',\
            fontsize=fs_sm)
top_ax.text(s*1000+(rw-s)/2*1000,lab_loc,\
            'Sheath',color='black',\
            va='center',ha='center',\
            fontsize=fs_sm)
top_ax.text(rw*1000+(xlim[1]-rw*1000)/2,lab_loc,\
            'Wall',color='black',\
            va='center',ha='center',\
            fontsize=fs_sm)

#Draw and label Debye Length:
lam=rw-np.array([pr.lambda_D(Te,ne),0])
top_ax.plot(lam*1000,[2]*2,color='black',\
            marker='|',ms=10,\
            markeredgewidth=3,lw=3)
top_ax.text(np.average(lam)*1000,1.5*vert_space,\
            r'$\lambda_{D}$',va='center',\
            ha='center',fontsize=fs)

#Save:
bdd.save(fig,'wall_sheath_IVP',savedir,save,extensions)
```

```
PNG Saved Successfully
PDF Saved Successfully
```

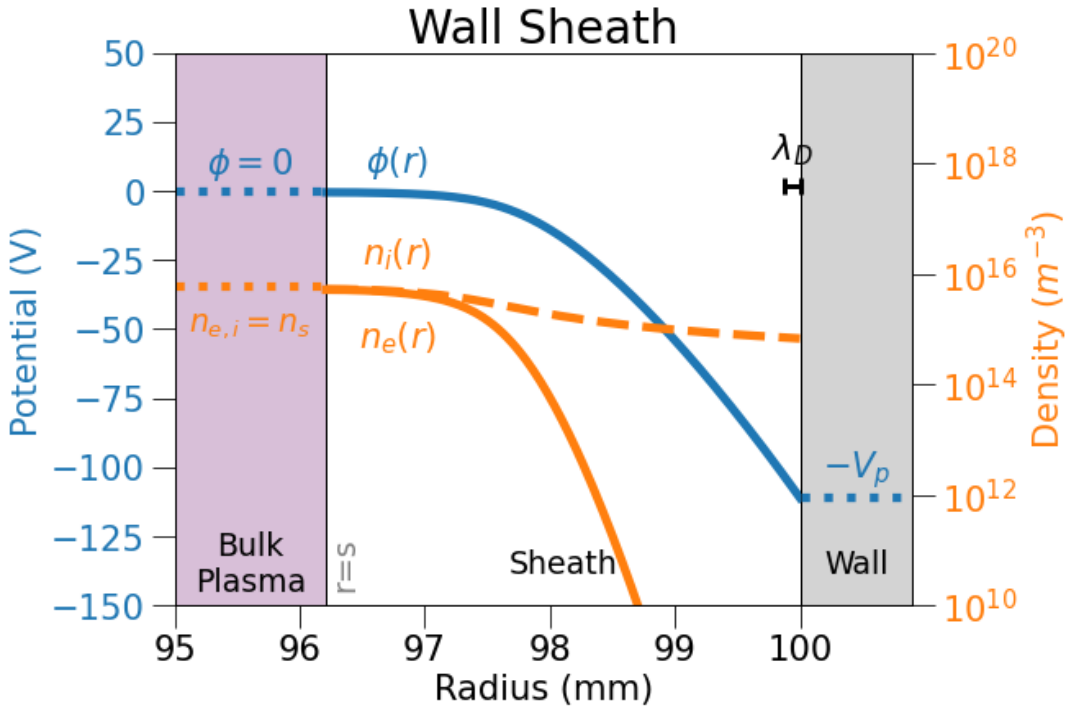

A.3.1 Another way to solve the wall sheath:

But is cheating on the $\phi' = 0$ condition okay? Let's solve the ODE a different way and compare the two.

Recall the three boundary conditions we know about $\phi(r)$ in the sheath:

(1) $\phi(r_{sheath}) = 0$

(2) $\phi'(r_{sheath}) = 0$

(3) $\phi(r_{wall}) = -V_{plasma}$

We can apply these BCs in a different order. We will now write a function that uses BCs (1) and (3) to solve Poisson's Equation and use scipy.optimize.fsolve() to find the sheath thickness for which ϕ conforms to BC (2)

So instead of solving Poisson's Equation as an initial value problem (IVP), we are solving it as a boundary value problem (BVP):

[13]:
```
#Our boundary conditions now depend on geometry, unlike the IVP␣
 ↪case where it didn't matter
#Here's a function to handle that:
def BCs_BVP(phi_l,phi_r):
    if surface.lower() in ['probe','p']:
        return(np.array([phi_l[1]-Vf,phi_r[1]]))
    if surface.lower() in ['wall','w','chamber','c']:
        return(np.array([phi_l[1],phi_r[1]-Vp]))


#solve_bvp() passes z r all at once
#as arrays (unlike odeint())
def dz_BVP(r,z):
    s = r[-1]
    if 'cyl' in geometry.lower():
        der = np.array((
            #z'[0] (which is phi"):
            A*(np.exp(z[1,:]/Te) - s/r*(1-B*z[1,:])**(-1/2))\
            - z[0,:]/r,
            #z'[1] (which is phi'):
            z[0,:]
            ))
        return der
    if 'sph' in geometry.lower():
```

```
        der = np.vstack((
            #z'[0] (which is phi"):
            A*(np.exp(z[1,:]/Te) - (s/r)**2*(1-B*z[1,:])**(-1/2))\
            - 2*z[0,:]/r,
            #z'[1] (which is phi'):
            z[0,:]
            ))
        return der
    print('d(z,r,s,geometry): Unknown geometry!')
    return

#Function to return (target potential')-(sheath potential')
#for a given sheath thickness. Have to supply sheath
#as a possibly-1D list.
def␣
 ↪diff_BVP(sheath,target=0,surface='probe',geometry='cylindrical'):
    if surface.lower() in ['probe','p']:
        s = rp + sheath[0]/1000
        r = np.linspace(rp,s,11)
        phi_guess = np.zeros((2,r.size))
        phi_guess[0,:] = np.array([-Vf/(r.size-1)]*r.size)
        phi_guess[1,:] = np.linspace(Vf,0,r.size)
        edge = -1 #array index for sheath edge
    elif surface.lower() in ['wall','w','chamber','c']:
        s = rw - sheath[0]/1000
        r = np.linspace(s,rw,11)
        phi_guess = np.zeros((2,r.size))
        phi_guess[0,:] = np.array([Vp/(r.size-1)]*r.size)
        phi_guess[1,:] = np.linspace(0,Vp,r.size)
        edge = 0 #array index for sheath edge
    else:
        print('diff_BVP(sheath,Z0,surface): Unknown surface type!')
        return
    res = solve_bvp(dz_BVP,BCs_BVP,r,phi_guess)
    phi_p = res.sol(r)[0]
    diff = phi_p[edge] - target
    return diff
```

[14]:
```
guess = 0.01 #Initial guess for sheath thickness
args = (0,'wall','spherical')
surface='wall'
geometry='spherical'
s_wall_BVP = fsolve(diff_BVP,guess,args=args)[0]
print('Sheath thickness for {} {} sheath: {:.2f} mm'.\
      format(args[2],args[1],s_wall_BVP))
```

```
<ipython-input-13-10ebab1990df>:26: RuntimeWarning: invalid value␣
 ↪encountered in
power
  A*(np.exp(z[1,:]/Te) - (s/r)**2*(1-B*z[1,:])**(-1/2))\

Sheath thickness for spherical wall sheath: 3.30 mm
```

[16]:
```
#Draw a demonstration of how we found the width:

#Find DeltaV across sheath for range of sheath thicknesses:
sheaths = np.linspace(1,6,200)
EField = np.empty(sheaths.size)
for i in range(len(sheaths)):
    EField[i]=diff_BVP([sheaths[i]],*args)/1000
```

```
#Prepare plot:
fig,ax=plt.subplots()
ax.set_title('Wall Sheath: Edge E-field vs Width')
ax.set_ylabel('Sheath Edge E-field (kV/m)')
ax.set_xlabel('Sheath Width (mm)')
ax.set_ylim([-75,25])
ax.set_xlim([sheaths[0],sheaths[-1]])

#Draw target EField, which is 0 kV/m:
ax.plot(sheaths,[0]*len(sheaths),color='black',\
        ls='dotted')

#Draw and label sheath edge EField:
ax.plot(sheaths,EField,color='C0')
ax.text(sheaths[40],EField[40]+10,'E(r=s)',rotation=57,\
        ha='center',va='center',fontsize=fs_sm,\
        color='C0')

#Draw and label BVP solution:
ax.axvline(x=s_wall_BVP,color='blue',ls='dotted')
ax.text(s_wall_BVP-0.1,-40,'BVP Solution',rotation=90,\
        color='blue',va='center',\
        ha='center',fontsize=fs_sm)
ax.axvline(x=s_wall_IVP,color='C1',ls='dotted')
ax.text(s_wall_IVP-0.1,-40,'IVP Solution',rotation=90,\
        color='C1',va='center',\
        ha='center',fontsize=fs_sm)

#Save:
bdd.save(fig,'wall_solution_BVP',savedir,save,extensions)
```

```
<ipython-input-13-10ebab1990df>:26: RuntimeWarning: invalid value␣
 ↪encountered in
power
  A*(np.exp(z[1,:]/Te) - (s/r)**2*(1-B*z[1,:])**(-1/2))\

PNG Saved Successfully
PDF Saved Successfully
```

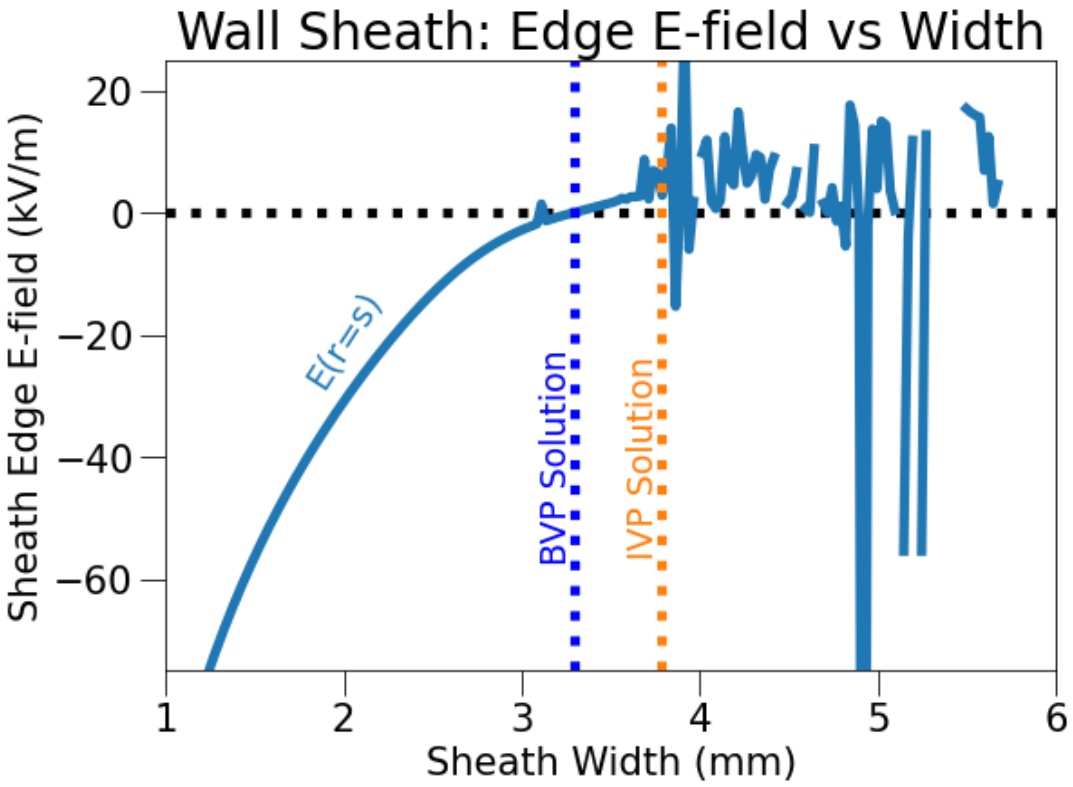

[22]:
```
#Now that we've solved it, let's draw the sheath:

#Solve for sheath:
s=rw-s_wall_BVP/1000
r_mesh = np.linspace(s,rw,11)
phi_guess = np.zeros((2,r_mesh.size))
phi_guess[0,:] = np.array([Vp/(r_mesh.size-1)]*r_mesh.size)
phi_guess[1,:] = np.linspace(0,Vp,r_mesh.size)
res = solve_bvp(dz_BVP,BCs_BVP,r_mesh,phi_guess)
phi = res.sol(r)[1]

#Prepare plot:
colors=[C0,'gray','black',ax_color_pot]
xlim = [95,100.9]
ylim = [-150,20]
fig,ax=plt.subplots()
ax.set_xlim(xlim)
ax.set_ylim(ylim)
ax.grid(False)
plt.xlabel('Radius (mm)',fontsize=fs)
plt.ylabel('Potential (V)',fontsize=fs,\
           color=colors[3])
plt.title('Wall Sheath')
ax.tick_params(axis='y', labelcolor=colors[3])

#Useful dimensions and locations for plot:
vert_space = (ylim[1]-ylim[0])*.05
horiz_space = (xlim[1]-xlim[0])*0.025
ymid = ylim[0]+(ylim[1]-ylim[0])/2
```

```
xmid = xlim[0]+(xlim[1]-xlim[0])/2
lab_loc = ylim[0]+(ylim[1]-ylim[0])*.075
rs_loc  = lab_loc

#Plot and label sheath potential:
r = np.linspace(s,rw,200)
ax.plot(r*1000,phi,lw=lw,color=colors[0])
ax.text(r[30]*1000,phi[30]+10,r'$\phi(r)$',\
        color=C0,ha='center')

#Draw bulk and chamber wall:
ax.fill_between([xlim[0], s*1000],[ylim[0]]*2,\
                [ylim[1]]*2,color='#D8BFD8')
ax.fill_between([xlim[1],rw*1000],[ylim[0]]*2,\
                [ylim[1]]*2,color='#D3D3D3')
ax.axvline(x=s*1000,color='black',ls='solid',lw=1)
ax.axvline(x=rw*1000,color='black',ls='solid',lw=1)

#r=s label:
ax.text(s*1000+horiz_space,rs_loc,'r=s',color=colors[1],\
        rotation=90,va='center',\
        ha='center',fontsize=fs_sm)

#Draw V_plasma at the wall:
ax.plot([rw*1000,xlim[1]],[Vp]*2,lw=lw,\
        ls='dotted',color=colors[0])
ax.text((rw+(xlim[1]/1000-rw)/2)*1000,Vp+vert_space,\
        r'$-V_p$',va='center',ha='center',\
        color=colors[0],fontsize=fs)

#V_bulk:
ax.plot([xlim[0],s*1000],[0,0],lw=lw,\
        ls='dotted',color=colors[0])
ax.text(xlim[0]+(s*1000-xlim[0])/2,vert_space,\
        r'$\phi = 0$',va='center',\
        ha='center',color=colors[0],\
        fontsize=fs)

#Set up density axis:
fig.set_size_inches(fgs_stretch)
ax2 = ax.twinx()
ax2.tick_params(axis='y', labelcolor=ax_color_den)
ylim_ne=[1e10,1e20]
ax2.set_ylim(ylim_ne)
ax2.grid(False)

#Plot plasma densities:
nes = ns*np.exp(phi/Te)
nis = ns*s/r*(1-B*phi)**(-1/2)
ax2.semilogy(r*1000,nis,color=C1,ls='dashed',\
             label=r'$n_i(r)$')
ax2.semilogy(r*1000,nes,color=C1,label=r'$n_e(r)$')
ax2.plot([xlim[0],s*1000],[ns]*2,lw=lw,\
         ls='dotted',color=C1)

#Label plasma densities:
ax2.text(r[30]*1000,nes[30]*.1,r'$n_e(r)$',\
         color=C1,ha='center')
ax2.text(r[30]*1000,nis[30]*3,r'$n_i(r)$',\
         color=C1,ha='center')
ax2.text((xlim[0]+s*1000)*0.5,ns*.2,r'$n_{e,i} = n_s$',\
         va='center',ha='center',\
         color=C1,fontsize=fs_sm)
```

```
ax2.set_ylabel(r'Density ($m^{-3}$)',ha='center',\
               fontsize=fs,\
               color=ax_color_den)

#Stuff that goes on top needs its own axis:
top_ax = ax.twinx()
top_ax.set_ylim(ylim)
top_ax.grid(False)
top_ax.set_yticks([])       #Don't draw y-axis ticks
top_ax.set_yticklabels([]) #Don't draw y-axis numbers

#Label bulk, sheath, and chamber wall:
top_ax.text(xlim[0]+(s*1000-xlim[0])/2,lab_loc,\
            'Bulk\nPlasma',color='black',\
            va='center',ha='center',\
            fontsize=fs_sm)
top_ax.text(s*1000+(rw-s)/2*1000,lab_loc,'Sheath',\
            color='black',va='center',\
            ha='center',fontsize=fs_sm)
top_ax.text(rw*1000+(xlim[1]-rw*1000)/2,lab_loc,\
            'Wall',color='black',\
            va='center',ha='center',\
            fontsize=fs_sm)

#Draw and label Debye Length:
lam=rw-np.array([pr.lambda_D(Te,ne),0])
ax.plot(lam*1000,[2]*2,color='black',marker='|',\
        ms=10,markeredgewidth=3,lw=lw_sm)
ax.text(np.average(lam)*1000,1.5*vert_space,\
        r'$\lambda_{D}$',va='center',\
        ha='center',fontsize=fs)

#Save:
bdd.save(fig,'wall_sheath_BVP',savedir,save,extensions)
```

```
<ipython-input-13-10ebab1990df>:26: RuntimeWarning: invalid value␣
 ↪encountered in
power
  A*(np.exp(z[1,:]/Te) - (s/r)**2*(1-B*z[1,:])**(-1/2))\

PNG Saved Successfully
PDF Saved Successfully
```

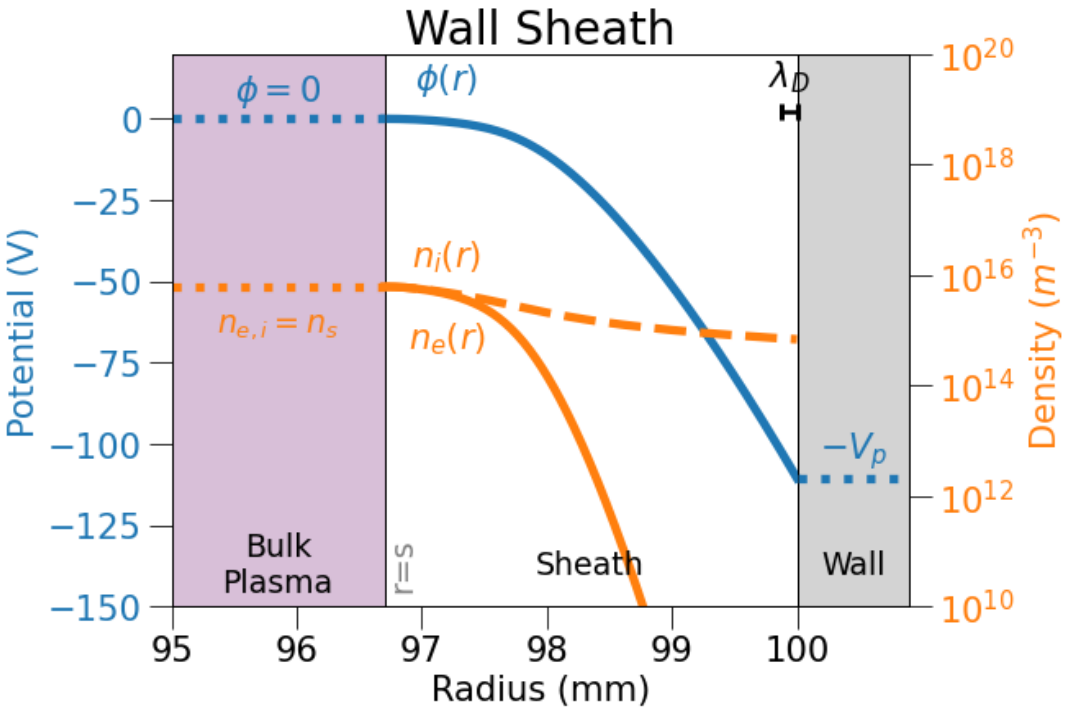

A.4 Conclusion

We know three boundary conditions for the electric potential in the sheath:

(1) $\phi(r_{sheath}) = 0$

(2) $\phi'(r_{sheath}) = 0$

(3) $\phi(r_{wall}) = -V_{plasma}$

To find the sheath thickness, one must write a function to solve Poisson's Equation with two of these three BCs, and then solve for the sheath thickness where the potential obeys the third BC. It might matter which order you use the BCs in. In our case, the wall sheath needs to be solved using BCs (1) and (3) to solve Poisson's Equation, not BCs (1) and (2), because otherwise our method could find mathematically valid, but non-physical solutions for the potential and densities.

[ ]: